RADIATIVE DECAYS OF η, ρ, ω, η' MESONS

PRODUCED IN THE REACTION

$\pi^- + p \rightarrow$ Meson $+ n$ AT 8.45 Gev/c

BY

© ELISA SHAHBAZIAN

A thesis submitted to the Faculty of Graduate Studies and Research
in partial fulfillment of the requirements for the degree of
Doctor of Philosophy (Physics)

Department of Physics
McGill University
Montreal, Quebec
Canada

November 1982

Radiative Decays of η, ρ, ω, η', Produced in Pion-Proton Collisions

(SHORT TITLE)

ABSTRACT

We have studied the radiative decays of non strange mesons into π^+, π^- and one or three gamma rays observed in the reaction

$$\pi^- + p \rightarrow \text{Meson} + n$$

at beam momentum 8.45 Gev/c in a Counter-Spark chamber experiment conducted at Argonne National Laboratory Zero Gradient Synchrotron.

We set a new upper limit on the branching ratio $\omega \rightarrow \pi^+\pi^-\gamma$ which is almost an order of magnitude smaller than the previously set upper limit.

We present a high statistics independent measurement of the branching ratio $\eta' \rightarrow \rho\gamma$.

We observed the decays $\rho(\omega) \rightarrow \eta\gamma$ for the first time in the reaction

$$\pi^- p \rightarrow \rho(\omega)n$$

and measured the decay rates $\Gamma_{\rho(\omega) \rightarrow \eta\gamma}$.

SOMMAIRE

Nous avons étudié les désintégrations radiatives des mésons d'étrangeté nulle en $\pi^+\pi^-$ accompagnés d'un ou de trois rayons gamma. Ces désintégrations furent observées lors de la réaction

$$\pi^- p \to \text{Méson} \quad n$$

á une impulsion incidente de faisceau de 8,45 GeV/c dans une expérience de type compteur-chambre à éticucelles au synchrotron à gradiant nul du Argonne National Laboratory.

Nous établissons une nouvelle borne supérieure du taux relatif de désintégration de $\omega \to \pi^+\pi^-\gamma$. Cette borne est plus petite de presqu'ún ordre de grandeur qu'une autre établie précédemment.

Nous présentons une mesure indépendente faite à grandes statistiques du taux de désintégration de

$$\eta' \to \rho\gamma \quad .$$

Pour la première fois lors de la réaction

$$\pi^- \; p \to \rho(\omega)n$$

nous avons observé les désintégrations

$$\rho(\omega) \to \eta\gamma$$

ainsi que mesuré les taux de désintégration

$$\Gamma\rho(\omega) \to \eta\gamma \quad .$$

ACKNOWLEDGEMENTS

I wish to express my thanks to my advisor, Dr. P. M. Patel for the advice and help he provided on this experiment.

Special thanks to Dr. P. J. Brockman and Dr. J. A. Dankowych for their help and advice in both the analysis and data-taking stages of the experiment.

I would particularly like to thank Dr. N. R. Stanton, Dr. T. S. Yoon, Dr. H. Areti and Dr. J. D. Prentice for the fruitful discussions during the analysis of the data and J. W. Heimaster for his assistance in the development of the analysis programs and for his help in the use of many of his software packages.

I would also like to thank other members of our collaboration who all contributed to the success of this experiment: Dr. K. W. Edwards, D. Legacy, Dr. J. Gandsman, Dr. A. J. Pawliki and Dr. J. F. Martin. In addition, I am grateful to the members of our earlier experiment who helped in constructing the Charged and Neutral Spectrometer: Dr. M. Shaevitz, C. Zanfino, Dr. R. Sidwell, Dr. N. W. Reay, Dr. K. Reibel, Dr. G. Luste, Dr M. Abolins and Dr. G. Luxton. My thanks also to Dr. G. Hartner for sharing his expertise, and A. Pezacki for her advice and help with computer facilities at University of Toronto.

I want to express my appreciation to the Argonne National Laboratory ZGS operations crew and H. Coombes, J. Fitch, A. Kiang and C. Rush for their technical support.

I want to thank Marc Turcotte for the translation of the abstract into french.

This research was supported in part by the United States Department of Energy and by the Natural Sciences and Engineering Research Council of Canada, through the Institute of Particle Physics.

CHAPTER 1. INTRODUCTION

We want to study the radiative decays of nonstrange mesons (η,ρ,ω,η') produced in the ~~reaction~~

$$\pi^- + p \longrightarrow \text{Meson} + n$$

The hadrons comprising baryons (p, n, etc.), antibaryons ($\bar{p}$, $\bar{n}$, etc.), and mesons (π, η, ρ, ω, η' etc.) are complex in their structure, unlike the leptons (electrons, muons, neutrinos, etc.). They have measurable size, about 10^{-13} cm, there are hundreds of them, and all of them, except for the protons and antiprotons, are unstable. To be able to understand the hadrons various ordering principles were invented to classify them.

First the hadrons were organized into small families called charged multiplets consisting of particles with approximately the same mass (e.g. protons and neutrons formed a doublet, pions formed a triplet etc.). In 1962 the charged multiplets were organized into "supermultiplets" that explained relations between particles differing in charge, hypercharge and mass.

The grouping of the hadrons into supermultiplets involves eight quantum numbers and was named the "Eightfold Way". Its mathematical basis is a branch of group theory invented in the 19th century by the Norwegian mathematician Sophus Lie. The group that generates the eightfold way is called SU(3), which stands for special unitary group of matrices of size 3 X 3. The theory requires that all hadrons belong to families corresponding to representations of the group SU(3). The families can have one, three, six, eight, ten or more members. It was possible to classify all known hadrons into families of one, eight and ten, but no families of three or six particles could be found.

In 1963 an explanation was proposed independently by Gell-Mann and George Zweig who suggested that all hadrons were constructed from more fundamental constituents called quarks that belonged to the family of three. The three simple rules of quark model were:

1) mesons are made of one quark and one antiquark.

2) baryons are made of three quarks and antibaryons are made of three antiquarks.

3) no other combination of quarks will make a hadron.

The quarks have fractional charges unlike the hadrons which all have integer multiples of electrons charge. The spin of the quarks is 1/2. Two of the quarks (called "up" and "down") have strangeness zero, isospin 1/2, and charges 2/3, -1/3 and the third (called "sideways") has strangeness -1, isospin zero and charge -1/3.

The family of eight pseudoscalar mesons (e.g. π, η, η', K) consists of a quark and an antiquark with spins in opposite directions and the family of eight vector mesons (e.g. ρ, ω, ϕ, K^*) consists of a quark and an antiquark with spins in the same direction.

The radiative decays of mesons are due to quark spin flip via emission of a photon. Thus a vector meson decays predominantly into a pseudoscalar meson and a photon and a pseudoscalar meson decays predominantly into a vector meson and a photon in so far as we consider radiative decays.

To study the radiative decays of mesons experimentally we will select the topologies in which a π^+, a π^- and a photon or a π^+, a π^- and three photons were detected in the forward direction. These topologies will contain the following radiative decays:

$\omega \rightarrow \pi^+\pi^-\gamma$	(one γ sample)
$\eta' \rightarrow \rho\gamma$	(one γ sample)
$\rho \rightarrow \eta\gamma$	(three γ sample)
$\omega \rightarrow \eta\gamma$	(three γ sample)

In 1974 the decay rate $\rho \dashrightarrow \pi\gamma$ was measured by B. Gobbi et al and the decay rate $\eta \dashrightarrow \gamma\gamma$ was measured by A.Brownman et al [5]. These values were about two standard deviations different from the values calculated from the non-relativistic Quark Model and the Vector Meson Dominance model, where the photon can become a virtual vector meson since it has almost identical quantum numbers as vector mesons.

This motivated a large number of theoreticians to develop different models to bring closer together the experimental and theoretical results. The Table in Appendix F shows the values of different radiative decays predicted by some of these models. These models can be divided into three categories:

1) Different modifications of quark model, where different methods are used to calculate the overlap integral

$$I_{P_j V_i} = \int d^3r \, \psi^*_{P_j} \psi_{V_i}$$

(where ψ_{V_i} is the wave function of the vector meson and ψ_{P_j} is the wave function of the pseudoscalar meson) or its value is left as a free parameter to fit the data [7,9,13,18].

2) Extended Vector Model Dominance models which include higher mass vector mesons [14,19,22,29].

3) Different SU(3) symmetry breaking models.

Between 1974 and 1979 the theoretical models greatly outnumbered the experiments which observed these decays. Appendix F also shows the existing few experimental measurements of these decay rates. We hope to reduce the disproportion between the number of experiments observing radiative decays and theoretical models studying them and to provide help to discriminate between the various models. This will be studied explicitly in Chapter 10.

To be able to predict the spectra of different observable kinematic variables in our experiment (particle energies, momenta, invariant masses etc.) and to calculate the acceptances of different radiative decay events by our limited solid angle apparatus we use Monte-Carlo simulation programs.

The Monte-Carlo method is a numerical way of solving different problems by the combined use of random numbers and theoretical models describing the problem.

In High Energy Physics one cannot observe directly the phenomena of interest. The nature of matter on the microscopic level is statistical, hence only probabilities of observing different outcomes of an experiment can be predicted in these models.

The number of independent variables necessary to describe completely one high energy event with n outgoing particles is 3n-4, when one insists on energy momentum consrvation. It is a major computational problem to predict observable distributions, using these independent variables in a theoretical model.

If the result of a Monte-Carlo calculation is a number or a set of numbers F $\{F = F(r_1, r_2 \ldots r_n)\}$, where $(r_1, r_2 \ldots r_n)$ is a sequence of random numbers between 0 and 1, then from statistics it is known that this is the estimate of the integral

$$I = \int_0^1\int_0^1 \ldots \int_0^1 F(x_1, x_2 \ldots x_n) dx_1 dx_2 \ldots dx_n$$

A Monte-Carlo simulation is a calculation involving series of n trials (or events), the outcome of each trial being a function of k random numbers. This calculation involves n x k random numbers and is equivalent to an integration over a k-dimentional space, where the estimate of the integral is the average over the n points.

We define as expectation of the function $F = F(r_1, r_2 \ldots r_k)$ as

$$E(F) = \int_0^1\int_0^1 \ldots \int_0^1 F(x_1, x_2 \ldots x_k) dx_1 dx_2 \ldots dx_k$$

and variance of this function as

$$var(F) = E\{F - E(F)\}^2$$

o

If X is the vector $x_1, x_2 \ldots x_k$, and X_i is a random vector corresponding to independent random $x_1, x_2 \ldots x_k$, then the law of large numbers says that if var(F) is finite, then

$$\lim_{n \to \infty} \left\{ \frac{1}{n} \sum_{i=1}^{n} F(X_i) \right\} = E(F)$$

This means that the Monte-Carlo estimate of the integral of a function F is a consistent estimation if var(F) is finite.

It can also be shown that the statistical error of the Monte-Carlo estimation decreases as $N^{-1/2}$.

We want to simulate the reaction:

$$\pi^- p \dashrightarrow \text{Meson} + n$$

$$\hookrightarrow M_{\pi^+\pi^-(\pi^0)} + \gamma$$

$$\hookrightarrow \pi^+\pi^-(\pi^0)$$

$$\hookrightarrow \gamma\gamma$$

A Monte-Carlo simulation of this process can be constructed if we know the probability distribution functions that govern each step. Using these functions we can imitate each step with numerical random variables, construct the correct sequence of these steps, and measure the statistics of observable variables.

The different distributions in this process are: the meson production differential cross-section, the resonance Breit-Wigner mass distributions, particle decay angular distributions, particle decay matrix elements and the phase space weight.

Random numbers X_R with desired distributions in the range [a,b] can be generated in the following way:

$$\frac{1}{F}\int_a^{x_R} f(x)\,dx = R$$

where R is a random number (0. < R < 1.), f(x) is the desired distribution and F is a normalization factor:

$$F = \int_a^b f(x)\,dx$$

For each decay step of the reaction the necessary distributions are generated and the energy and momentum of the produced particles are simulated which are constrained by energy-momentum conservation laws.

When the 4-vectors of the reaction are simulated the geometric, kinematic and trigger constraints of the experiment are being applied on them. Then the charged pion decay in flight and charged pion and photon interactions in the target are simulated.

We can use the Monte-Carlo simulated spectra of different kinematic variables to compare with corresponding spectra obtained from our data to understand and find cuts to reduce the number of background events.

In the one gamma topology we study the decays $\omega \dashrightarrow \pi\pi\gamma$ and $\eta' \dashrightarrow \rho\gamma$.

In the three gamma topology we study the decays $\rho(\omega) \rightarrow \eta\gamma$ with the subsequent $\eta \rightarrow \pi^+\pi^-\pi^0$ decay. This is of particular interest to observe since there are no previous experiments that have seen these decays when the $\rho(\omega)$ mesons were produced in the $\pi^- p$ interactions. In these reactions the rho and omega production differential cross-sections are different in contrast with the $\rho(\omega)$ photoproduction experiments where these ($\rho(\omega) \rightarrow \eta\gamma$) decays were previously observed. This will allow us to separate the events due to rho decays from the events due to omega decays and measure their decay rates separately, which could not be done in photoproduction experiments.

For the reaction:

$$\pi^- + p \rightarrow \text{Meson} + n$$

we used the data collected at Argonne National Laboratory Zero Gradient Synchrotron in high statistics counter experiments E397, E420 and E428, using an 8.45 Gev/c momentum pion beam. We now proceed to give a detailed overview of the data sample we used.

1.0 THE "ONE GAMMA" DATA SAMPLE - AN OVERVIEW.

In the data sample where two charged pions and only one gamma ray were detected, the final data summary tape (DST), from experiment E(397) only, contains 45577 events. After all additional cuts to reduce background the $\pi^+\pi^-\gamma$ invariant mass plot (Fig 5-10) shows no indication of $\omega \to \pi^+\pi^-\gamma$ events, and has a clear enhancement at η' mass. Using this data we can:

a) Set a new upper limit for the branching ratio Br($\omega \to \pi\pi\gamma$), and

b) Get a new high statistics measurement of the branching ratio $\eta' \to \rho\gamma$.

c) Check for the existence of the resonance M(953) [43,44,45].

a) $\omega \to \pi^+\pi^-\gamma$ decay mode:

In the mass range $0.6 < M_{\pi\pi\gamma} < 0.8$ Gev/c there is a peak coming from events $\omega \to \pi^+\pi^-\pi^0$ with one gamma missing. There may be some $\omega \to \pi^+\pi^-\gamma$ events too in this peak, but the branching ratio Br($\omega \to \pi^+\pi^-\gamma$) is found to be much smaller than the particle data book upper limit [Br($\omega \to \pi^+\pi^-\gamma$ $<$ 5%]. We come to this conclusion by comparing the ω mass region with the η mass region ($0.4 < M_{\pi\pi\gamma} < 0.6$ Gev) in Fig.5-10;

(i) The branching ratios for η meson are:

$$Br(\eta \longrightarrow \pi^+\pi^-\gamma) = 4.98\%$$

$$Br(\eta \longrightarrow \pi^+\pi^-\pi^0) = 23.6\%$$

(ii) The acceptance ratio for eta events - the acceptance of $\eta \longrightarrow \pi^+\pi^-\pi^0$ with one gamma missing events (peak 1) divided by the acceptance of $\eta \longrightarrow \pi^+\pi^-\gamma$ events(peak 2) is (table 5-3)

$$R_\eta^{Acc} = 0.017 / 0.045 = 0.378$$

and the similar ratio for omega events is

$$R_\omega^{Acc} = 0.027 / 0.071 = 0.380$$

(iii) The branching ratio for $\omega \longrightarrow \pi^+\pi^-\pi^0$ is 89.8%

(iv) The $\pi^+\pi^-\gamma$ mass resolution at omega mass is about 25% larger than at eta mass. The observed width of eta meson is $\Gamma_{o\eta}$ = 15.2 Mev, which is equal to the resolution at eta mass, since the true eta width can be ignored ($\Gamma_{T\eta}$ = 0.85 Kev). The observed omega width would be

$$\Gamma_{o\omega} = (\Gamma_{R\omega}^2 + \Gamma_{T\omega}^2)^{1/2} = 20.6 \text{ Mev}$$

where $\Gamma_{R\omega}$ = 1.25 $\Gamma_{o\eta}$ is the resolution at omega mass and $\Gamma_{T\omega}$ = 10.1 Mev is the omega true width.

(v) The mass resolution for $\pi^+\pi^-\pi^0$ with one gamma missing events is about the same for η and ω region.

There are about half as many $\eta \rightarrow \pi^+\pi^-\gamma$ events as $\eta \rightarrow \pi^+\pi^-\pi^0$ events with one gamma missing in our sample. Considering (i),(ii) and (iii) if the branching ratio $Br(\omega \rightarrow \pi^+\pi^-\gamma)$ is close to 5% there would be about six times fewer $\omega \rightarrow \pi^+\pi^-\gamma$ events than $\omega \rightarrow \pi^+\pi^-\pi^0$ with one gamma missing events. Considering (iv) most of these events would be concentrated in two bins. In this case one would expect to see a separate peak or at least a bump at ω mass. Details are given in Chapter 5.

b) $\eta' \rightarrow \rho\gamma$ decay mode

The η' meson has been observed by a number of experiments [31]-[42], but these experiments had fewer statistics (only Danbury et al [38] had data statistics comparable to ours) than our experiment and most of them observed the η' in a different reaction:

$$K^- p \longrightarrow \Lambda\eta'$$

$$K^- p \longrightarrow \Sigma^0\eta'$$

Also some earlier experimental measurements [35,36,37] disagreed with later measurements [38-42] of the branching ratio of $\eta' \rightarrow \pi^+\pi^-\gamma$. We were able to make an independent high statistics measurement of this branching ratio.

c) M(953) meson

Some experiments [36,37 and 43] observed a meson at 0.953 Gev decaying directly into $\pi^+\pi^-\gamma$. In our data sample in the mass range of $0.8 < M_{\pi\pi\gamma} < 1.04$ Gev, all the events in the peak around 0.95 Gev were found to be coming from the $\rho\gamma$ decay of the η' meson.

2.0 THE "THREE GAMMA" DATA SAMPLE - AN OVERVIEW.

In the data sample where two charged pions and three gamma rays were detected we will concentrate on the study of the decays $\rho\ (\omega) \rightarrow \eta\gamma$, since the decay $\eta' \rightarrow \omega\gamma$ was studied elsewhere [4]. Experimentally these decays were previously observed in a $\rho\ (\omega)$ photoproduction experiment [30] and two model dependent solutions were given. In photoproduction experiments the production mechanisms of ρ and ω mesons are the same (Vector Model Dominance), but the ω production cross section is an order of magnitude smaller than the ρ production cross section (the coupling of ω and gamma $f_{\gamma\omega} = 1/3 * f_{\gamma\rho}$). This makes it very difficult to separate the ρ and ω decays from each other. In our experiment the ρ and ω production mechanisms are different (π+A2 exchange for ρ, and B+ ρ exchange for ω) leading to a different momentum transfer dependence. At large transverse momenta [$|t'| > 0.4 (Gev/c)^2$] ω production dominates making it possible to separate the ρ and $\omega \rightarrow \eta\gamma$ decays. We simultaneously fitted the $\eta\gamma$ mass spectrum for two $|t'|$ ranges ($|t'| < .4\ (Gev/c)^2$ and $|t'| > .4\ (Gev/c)^2$) and the whole mass spectrum for the final data sample (Fig 7-20) to the theoretical model [6] discussed in Appendix E. We obtained two solutions one of which agrees with most of the predictions [7]-[29] and one of the solutions from the previous experiment [30]. We cannot, however, rule out the second solution because of poor statistics at present.

3.0 SUMMARY

We used only the data from experiment E(397) when studying the decays into $\pi^+\pi^-\gamma$. We did not need the data from experiments E(420) and E(428) since there was already a large number of events of this type in E(397), and the experiments E(420), E(428) were designed to handle larger number of gamma rays which improved the detection rate of multi-gamma events but worsened the experimental resolution for the gamma momentum vector.

In Chatper 2 we describe experiment E(397). Chapter 3 contains the details of data collection and analysis. Chapter 4 presents the experimental resolution of the apparatus for E(397). Chapter 5 gives the experimental acceptance of the apparatus and the selection of the final sample of the $\pi^+\pi^-\gamma$ events. In chapter 6 our experimental results for the radiative decays into $\pi^+\pi^-\gamma$ are presented.

In Chapter 7 we discuss the differences in the apparatus of experiments E(397), E(420) and E(428), the effects of these differences on the resolution and reconstruction programs. In this chapter we also study the data sample with two charged pions and three gamma rays detected, and the experimental acceptance of the apparatus of such events for the experiments E(420) and E(428). The inefficiency corrections are calculated in Chapter 8 and Chapter 9 presents our experimental results for the decays $\rho\ (\omega) \longrightarrow \eta\gamma$.

In Chapter 10 we discuss our conclusions.

CHAPTER 2. APPARATUS

1.0 INTRODUCTION

The experimental layout of our charged particle and gamma ray spectrometer is shown in Fig.2-1. It was set up to study, among other processes, the radiative decays of different mesons in the data subsets where two charged pions and an odd number of gamma rays (1 or 3) were detected in the process;

$$\pi^- p \rightarrow \pi^+ \pi^- \gamma n$$

and

$$\pi^- p \rightarrow \pi^+ \pi^- \pi^0 \gamma n$$
$$\quad\quad\quad\quad\quad\quad \hookrightarrow \gamma\gamma$$

The beam consisted of 8.45 Gev/c negative pions produced at the Zero Gradient Synchrotron (ZGS) at Argonne National Laboratory. The experimental target was a 16 inch long, one inch radius cylinder of liquid hydrogen. The recoil neutron was not detected and the direction and the momenta of charged particles and gamma rays were measured in the spectrometer as described in the following sections.

2.0 BEAM

The beam in this experiment was a secondary pion beam produced in the Extracted Proton beam II area of the ZGS by directing 12 Gev/c protons at a beryllium target. Negative particles produced at 1.5 degrees were focussed and brought to the experimental area by a two stage system of quadrupole and bending magnets shown on the Fig.2-2.

The first stage consisting of the bending magnets SB1, SB2, quadrupole magnets Q1, Q2, bending magnet B1 and a brass collimator, produced a momentum dispersed focus at the position of the beam hodoscope BH. BH consisted of seven scintilation counters that selected an overall 2.5% momentum bite from the particles focussed at this point.

The second stage consisting of the strong bending magnet B2 and four quadrupole magnets Q3, Q4, Q5 and Q6 recombined the momenta and focussed the beam on anti counters BV1 and BV2, located 120 inches downstream of the hydrogen target, where all non-interacting beam events were rejected.

The beam particle direction and position were determined by four magnetostrictive readout spark chambers upstream of the hydrogen target. A pair of anti counters BHR+BHL vetoed all beam particles outside of the one inch radius diameter hole at the target. On the average 85% of beam passed within the hole.

The contamination of other negative particles (i.e. μ^-, K^-, e^-) was found to be; 5.0 + 0.4% for μ^-, 3.2 + 0.1% for K^- and an insignificant amount of e^-. Table 2-1 gives the summary of the beam characteristics.

3.0 CHARGED PARTICLE SPECTROMETER

The momenta and positions of the charged particles were measured by the charged particle spectrometer which consisted of a set of five spark chambers on either side of a wide aperture magnet (SCM 104) and was located immediately downstream of the hydrogen target. The summary of the charged particle spectrometer characteristics is given in Table 2-2. The narrow width of the magnet (40 inches) and closeness of the spark chambers to each other and the magnet ensured a good acceptance for the large-angle tracks. Two chambers upstream of the magnet were rotated by 45 degrees and two chambers downstream of the magnet were rotated by 15 degrees to eliminate ambiguities which arise from multiple tracks.

Spark positions in the chambers were read out by magnetostrictive techniques and a SAC scaler system interfaced to CAMAC. Each plane could handle up to six sparks.

In all spark chambers including the beam chambers and the chambers used in the gamma ray detecting system, a mixture of 90% neon and 10% helium was used with ethyl alcohol added to quench the sparks. The gas was purified and recirculated by a carbon and liquid nitrogen trap (The Berkely Gas Cart).

At the beginning of every ZGS pulse the spectrometer chambers were triggered on a non-interacting beam track. These events were used to update the spectrometer chamber spatial positions and the distance per scaler count for each magnetostrictive ribbon. These could change because of the aging of the spectrometer or short term temperature effects.

4.0 PHOTON DETECTOR

The energy of the photons was measured using a system of 56 lead glass Cherenkov counters and their position was measured with a system of a 1.6 radiation length lead converter and three magnetostrictive readout spark chambers closely packed together. Two of the three chambers were rotated 2.5 degrees to resolve multi-track ambiguities. 67% of the photons coming into the detector showered in the lead producing tightly collimated showers with rms angle approximately 0.2 degrees for 1 Gev photon, [1], [3]. Closeness of the first spark chamber (1/4 inches away from the lead) resulted in these showers being recorded as a single spark in this first chamber and thus the shower center was accurately determined. The second and third spark chambers supplied information for showers which were missed by the first chamber and were also used to confirm and resolve shower positions. The momentum vector of the photon was obtained by joining the shower origin to the interaction point in the target.

The spark digitization for these chambers was performed by a Borer scaler-CAMAC system. The first chamber was instrumented to handle up to eight sparks and the second and third spark chambers could handle up to twelve sparks.

As in the charged particle spectrometer chambers the non-interacting beam events were used to update the positions of the gamma chambers and the speed of their magnetostrictive pulses.

The symmetrically stacked lead glass array (Fig.2-3) was positioned immediately downstream, 5 inches away from the shower chambers. Each block was 10 radiation lengths deep (approximately 12 inches) and 7.5 inches by 7.5 inches in cross-section. It was viewed by a 5 inch photomultiplier tube attached to its downstream face. A small hole in the array allowed the beam to pass through unaffected. The signal from each photomultiplier was fed into an analog to digital converter (ADC) and the digitized information was made available to the online computer via CAMAC. The ADC reading, after small corrections for geometrical losses, was proportional to the energy deposited in the block. The proportionality constant was a function of the photomultiplier tube gains, which were sensitive to fluctuating temperature. Two procedures to monitor the relative gain drifts between the tubes were used. The light output from a nitrogen laser was piped to each block via fiber optics. To correct the short term drifts, laser pulse height data were recorded at the start of each ZGS pulse. The offline analysis program used this data to update the tube gains on the run-to-run basis. As a check against long term drifts, energy spectra were recorded for each of the blocks twice daily, using several thousand laser pulses. This data was used by the online analysis program.

Gamma rays from π^0 decays were used as a standard for absolute calibration. The method which was used to calibrate a lead glass block is outlined in Fig.2-4. The errors in the π^0 mass measurement mainly came from the gamma energy determination uncertainty. Therefore, for all two gamma events, for the blocks which contained a shower center, a digamma mass distribution, summed over all the other blocks, was plotted. The ratio of the centroid of the histogram for a block to the actual π^0 mass was used to correct the tube gains for that block.

5.0 THE TRIGGER

A system of scintillation counters combined with fast electronic logic modules was designed to indicate the presence of at least two charged tracks and at least two gammas in the detector with no charged particles or gamma rays recoiling at wide angles. Later in this paragraph we discuss how we obtained our one gamma data sample from these events.

This system produced a trigger that was used to initiate the firing of the spark chambers, the gating of the gamma shower ADC's and the storing of the resulting CAMAC information. A simplified trigger diagram is shown in Fig.2-5. The triggering system consisted of the following parts designated as beam, charged, gamma and anti. When requirements of all these parts were satisfied the fast logic initiated an event trigger.

The beam part required an interaction in the target;

$$S1 * B1 * B2 * \overline{(BHR * BHL)} * \overline{(BV1 * BV2)}$$

A count in S1, B1 and B2 means there was a beam particle. No count in BHR and BHL means it went into the target and no count in beam veto counters BV1 and BV2 means that the beam particle interacted.

The charged part required at least two charged particles to be present after the magnet with at least one particle leaving the target at an angle greater than 4°;

$$HO(\geqslant 1) * H2(\geqslant 2)$$

A count in HO means the charged particle went outside the 1.5 inches diameter hole centered on the beam, which means that it had an angle greater than 4°, and a count in at least 2 of the 30 element scintilation hodoscope H2 indicated the presence of two charged particles.

The gamma part required at least two possible gamma showers to be present.

$$\overline{GHF} * GHR\ (\geq 2)$$

GHF and GHR are two identical 16-element scintillation hodoscopes before and after the lead converter respectively. No count in a GHF element and a count in the GHR element directly after it means that a photon had passed through the GHF element and produced a shower in the converter which was detected by the GHR element. The gamma part of the trigger required at least two such no-yes combinations in the GHF and GHR.

Often, after the off-line analysis of the data, one of these two no-yes combinations was proved to be coming from different background reasons such as a δ-ray from a charged pion going in the neighbouring H2 paddle or a cosmic ray or electronic noise in the GHR counters. The one gamma data sample consisted of these events.

The anti part of the trigger rejected gamma rays and charged particles recoiling at wide angles or missing the acceptance;

$$\overline{AA1 + AA2 + TA(\geq 1)}$$

The aperture-anti counters AA1 and AA2 were located upstream of the magnet and were used to veto the events with decay particles that would go outside the geometrical acceptance of charge particle and gamma detectors.

The upstream sides of these counters were covered with 0.25 inches of lead sheets to make them sensitive to gamma rays as well. The target anti counters (TA) were used to reject gamma rays or charged particles recoiling at wide angles.

The TA system consisted of four alternate layers of 0.125 inches of scintilator and 0.25 inches of lead sheets on each of the four lateral sides of the hydrogen target. To stop low energy particles such as δ-rays the target was surrounded by a 0.5 inches thick polyethylene (CH_2) (before the TA counters). The anti part of the trigger demanded no counts in either AA1 or AA2 and no more than 1 count in the TA system. All the TA counters were latched to allow studies of the event for which one counter fired.

Table 2-3 lists all the counters of the trigger system.

CHAPTER 3. DATA COLLECTION AND ANALYSIS

1.0 DATA COLLECTION

Data collection was performed on a General Automation SPC 16/85 computer interfaced to the experiment through CAMAC. Each event consisted of 260 16-bit words and the collection system was capable of recording up to forty events in each 600 msec pulse. All the data was recorded on magnetic tapes for later off line analysis.

About 30% to 40% of the events were analysed online during the time between the machine pulses. The online analysis program calculated all the spark chamber efficiencies and plotted the scintillation counter participation and lead glass block participation rate, thus providing us with a valuable means of monitoring the equipment performance continuously. Also the three pion effective mass and the missing mass were plotted to provide us with information about the useful data yield.

The non-interacting beam events and the laser pulse lead glass calibration data were not used by the online program, but were recorded on magnetic tapes for off line use.

2.0 DATA ANALYSIS

All the events recorded on tapes were reanalysed on the IBM facilities at McGill University, Ohio State University and University of Toronto.

The offline analysis program used the same trackfinding and fitting software as the online program. This track reconstruction software consists of three basic sections: the beam, the charged particles and the gamma rays and will be described in detail later. The offline program progressively updated the spark chamber fiducial positions and pulse speeds on the magnetostrictive wands using the non-interacting beam events. It also used the laser calibration information to update the lead glass phototube gains. For each month's data, an absolute calibration for these gains was done using the events with a neutral pion. This has significantly improved the resolution of the apparatus.

After all events were analysed a sample of well understood $\omega(783)$ events with two charged tracks and two gamma rays was selected. This was used to refine the chamber orientations and lead glass phototube gains. The adjustments to the chamber positions and the phototube gains were obtained by weighting them to get a good kinematic fit for each event.. These new adjustments were later used to reanalyse all the events to obtain so called "tuned" events. These were stored on the data summary tapes (DST). From these DST tapes different topologies were selected to study different interactions.

In about 40% of all events with two oppositely charged pions, the offline analysis program has found less than two real gamma showers (one or more no-yes combinations in GHF and GHR counters were found to be coming from different background reasons). About 15% of the events the two oppositely charged pions were accompanied by three real gamma showers.

3.0 RECONSTRUCTION SOFTWARE

The reconstruction software consisted of three basic sections: beam, charged particles and gamma rays.

1.Beam:

The beam line magnetic optics were tuned to have pions of 8.45 Gev/c momentum for all the runs. However for each event the more precise momentum of the beam track was determined according to which BH counter detected it. The direction and position of the beam track was obtained from the beam spark chambers - using the same trackfinding routines that reconstructed the charged particle trajectories. Events with more than one beam track were discarded and if the beam track hit two of the BH counters its momentum was averaged.

2.Charged tracks.

The momenta of the charged particles were calculated using their trajectories. The trajectories of the particles were reconstructed by searching for tracks within corridors in space defined by the H2 hodoscope element dimensions, an imaginary grid similar to H2 at the magnet center and the hydrogen target. This method saved a considerable amount of time. In these corridors the tracks were first searched in the downstream y-view, then in the downstream x-view. To further constrain the track candidates these tracks were crosschecked in rotated chambers. In each view a track was accepted if it contained two of three x or y plane coordinates and one of the two u or v plane coordinates. The track candidates with common sparks were pruned and the tracks with lowest chi-squared values were kept. The upstream and downstream sections of tracks were then matched at the magnet center. A common intersection with the beam track for two or more of the charged tracks was demanded to occur within the hydrogen target fiducial volume. The particle trajectories were also corrected for bending outside of the magnet caused by the strong fringe field. Fig 3-1 shows the reconstructed trajectories for a three-prong event. The momenta of the particles were determined by comparing the final trajectories with a fourteen term momentum function that was developed [1] using numerical integration of Monte-Carlo created tracks. A detailed magnetic field map was available for this purpose.

This method of calculating the momentum circumvented the necessity of doing point by point integration in the magnetic field.

3.Gamma rays.

Fig 3-2 shows the gamma shower reconstruction flowchart and fig 3-3 shows an example of a reconstructed event with two gamma showers.

The gamma rays were reconstructed by first looking for a lead glass block where more than 30 Mev energy was deposited. For each such block, roads were constructed within which the gamma shower sparks were expected to lie. For each shower candidate a code word ('score') was constructed which indicated which spark chamber participated. A minimum of one x and one y spark was required in the first or second shower chamber and at least one x or one y spark was required in the next chamber. The shower center was determined by the sparks in the first two chambers.

To eliminate ambiguities resulting from an overlap of a charged particle and a gamma ray, events with a shower candidate within 5 inches of an extrapolated charged track position in the lead glass were rejected. Two showers with different 'scores' had to be more than 7.6 inches apart. If they were less than 7.6 inches apart the shower with the smaller 'score' value was rejected. The showers with same 'scores' had to be more than 4.0 inches apart, otherwise their energy was combined and the position was averaged.

The shower energy was determined by adding the energy deposited in the blocks surrounding the shower candidate. If two showers were next to the same block, the energy in that block was shared inversely proportional to the square of the distances of the shower centers from the block. Then the overall energy deposited for each shower candidate was corrected for energy losses in the lead converter, around the photomultiplier tube and in the 0.04 inch thick magnetic shields surrounding each block [1]. For all events with two or more showers, the two showers forming an invariant mass closest to the π^0 mass were selected and put first and second in the final analysis event buffer, in decreasing order of energy.

CHAPTER 4. EXPERIMENTAL RESOLUTION

The particle momentum and direction measurement errors were studied in detail by a previous experiment using the same apparatus [1]. Their results with minor modifications due to slightly higher beam momentum were used in our experiment.

1.0 BEAM

The beam momentum error is given in Table 2-1

$$\Delta p/p = 0.005 \text{ (FWB)}$$

The beam slope errors were given by the expression

$$\Delta\theta \text{ (FWHM)} = [(1.3*10^{-4}) + (0.015/p)^2 *t]^{\frac{1}{2}} \quad \text{rad}$$

where the first term is the angle error due to position measurement and the second term is the error due to multiple scattering of the beam particles in the target. Here p is the beam track momentum given in Gev/c and t is the number of radiation lengths of hydrogen seen by the beam track. Typicaly for 1 Gev/c pion traversing the target $\Delta\theta \simeq 0.01$ rad.

2.0 CHARGED PARTICLES

The charged particle momentum error consists of the multiple scattering error of 2.8% (FWHM) and a term that comes from the position error in the spark chambers

$$\Delta p/p \text{ (FWHM)} = [(0.028)^2 + (.11 * p/P_{beam})^2]^{\frac{1}{2}}$$

The second term was obtained by extrapolating to the appropriate momenta the position errors calculated for the non-interacting beam tracks. The momentum error, for a beam track of 8.45 Gev/c, was found to be 9% (FWHM) - this corresponds to a spark chamber position error of 0.04 inches (FWHM). For two track events the position error was found to be approximately 0.05 inches, which corresponds to momentum error of 11% (for p=8.45 Gev/c).

The error in the charged particle angle measurements was given by

$$\Delta\theta \text{ (FWHM)} = [(0.0014)^2 + (0.036/p)^2 * t]^{\frac{1}{2}} \text{ rad}$$

The first term is an estimate of an angle error in the position measurement and is very small compared to the second term, that comes from the multiple scattering of the charged tracks in the hydrogen target. Here t is the radiation length of material travelled by the charged particle in the target.

3.0 GAMMA RAYS

The gamma ray energy error was calculated by observing the symmetric decays of the neutral pions in the topologies with two or more gamma rays. The di-gamma mass is given by the expression

$$M_{12}^2 = 2*(1 - \cos\theta)*E_1*E_2 = k*E_1*E_2$$

Thus the fractional error on the di-gamma mass will be

$$2*\delta M_{12}/M_{12} = [(\delta E_1/E_1)^2 + (\delta E_2/E_2)^2]^{\frac{1}{2}}$$

When $E_1 = E_2$

$$\delta M_{12}/M_{12} = 1/\sqrt{2} * \delta E_1/E_1$$

Using this expression the gamma energy resolution was calculated by measuring the π^0 width for different gamma energy bins. The gamma energy resolution (i.e. $\sqrt{2} * \pi^0$ mass resolution) as a function of the gamma energy was fitted to the following curve

$$\delta E_\gamma/E_\gamma \text{ (FWHM)} = 0.055 + 0.175/\sqrt{E_\gamma}$$

The shower position error was calculated by tracking electrons of various energies through the apparatus. The position determined by the spectrometer was compared with the position found at the converter. The position error was found to be

$$\Delta x \text{ (FWHM)} = 0.35 \text{ inches.}$$

D A T A   A N A L Y S I S

SECTION 1.   STUDY OF THE EVENTS $\pi^- p \rightarrow \pi^+ \pi^- \gamma\ n$

CHAPTER 5. FINAL EVENT SELECTION

1.0 KINEMATICS

From the final data summary tapes, events that have one positive and one negative charged track and one gamma shower were selected for the study of radiative decay of resonances to the final state $\pi^+\pi^-\gamma$. The gamma ray and the charged tracks were constrained to lie inside a one inch border in each detector to avoid any problems arising from detector inefficiencies around the edges. The charged pion momenta were required to be at least 400 Mev/c to avoid the reconstruction problems for soft particles.

In our data sample the gamma momentum was cut at 700 Mev/c. Contrast this with a cut of 300 Mev/c applied to the other topologies where two or more gamma rays were present, and where two gammas come from a π^0 decay (or from an η decay). In these topologies it is easier to reconstruct the gamma energy using the neutral pion or eta mass as a constraint. Hence a higher gamma ray energy cut is not necessary. In our data sample where only one gamma ray was detected there is a large fraction of events where a meson was produced with a more common decay into $\pi^+\pi^-\pi^0$ system but one of gammas from the $\pi^0 \rightarrow \gamma\gamma$ decay is not detected.

In order to reduce the number of such events and also to remove the small contamination of $\pi^+\pi^-\gamma N^*$ events (where $N^* \rightarrow n\,\pi^o$) which survived in spite of the target anti-coincidence system, we also instituted a cut $M_{rec} < 1.5$ Gev. Less than 30% of all one gamma events survived after this cut.

Fig.5-1 shows the $\pi^+\pi^-\gamma$ mass spectrum ($M_{\pi\pi\gamma}$) for the events left after all the cuts (geometric and kinematic) discussed above. Table 5-1 gives the summary of these cuts.

All the events were then fitted to the hypothesis $\pi^- p \rightarrow \pi^+\pi^-\gamma\ n$ with the missing mass constrained at the neutron mass value. This procedure should enhance the signals in Fig.5-1 that are due to events which agree with the hypothesis. Fig.5-2 shows the fitted $M_{\pi\pi\gamma}$ spectrum for the data sample shown in Fig.5-1.

There are four peaks in Fig.5-2. The first peak at approximately 0.500 Gev comes from the $\pi^+\pi^-\pi^o$ decay of the η meson with one gamma from the $\pi^o \rightarrow \gamma\gamma$ decay not detected. It is lower in mass than the eta meson mass (0.55 Gev) because of the missing gamma. The second peak in Fig.5-2 has become considerably sharper than the corresponding peak in Fig.5-1. This peak is at eta meson mass and is due to bonafide $\pi^+\pi^-\gamma$ decays. The third peak in Fig.5-2 comes from $\omega \rightarrow \pi^+\pi^-\pi^o$ with one gamma missing events. It is at about 0.750 Gev. The fourth peak in Fig.5-2 has become much sharper because of fitting and is at approximately 0.950 Gev. This peak is due to the $\pi^+\pi^-\gamma$ decay of η' meson.

The background events as well as the η, ω --> $\pi^+\pi^-\pi^0$ events (with one gamma missing) will be discussed in detail later in this chapter.

2.0 EXPERIMENTAL ACCEPTANCE

In order to understand the backgrounds coming from $\pi^+\pi^-\pi^0$ decays of mesons with one undetected gamma ray from the π^0 and also to find the acceptances of the apparatus for such events and for true radiative decay ($\pi^+\pi^-\gamma$) events, the Monte-Carlo simulation programs described in Appendix A were used. These programs used specified $d\sigma/dt$ and decay angular distributions to generate momenta of particles coming from the reaction

$$\pi^- p \text{ --> Meson} + n$$

and the subsequent decay of the meson into $\pi^+\pi^-\gamma$ or $\pi^+\pi^-\pi^0$. Then interactions of the charged particles or gammas with the hydrogen in the target, and the decay of a charged pion were simulated by statistically rejecting events, using the cross-sections of charged particles and gamma rays in hydrogen, and the charged pion decay rates.

In the Monte-Carlo program for the true radiative decays for the events where no interactions in the target have occured and no pions decayed while passing through the detector, the geometric and kinematic cuts of Table 5-1 were applied. The acceptance of events surviving these cuts was calculated and also the 4-vectors of these events were stored on magnetic tape for later processing.

In the Monte-Carlo program, where the meson decayed into $\pi^+\pi^-\pi^0$, for all the events where the charged pions did not decay while passing through the detector, or did not interact in the target we proceeded as follows:

1. If only one gamma interacted in the target, then the geometric and the kinematic cuts were applied for the charged pions and the gamma that did not interact in the target.

2. If neither of the gammas interacted in the target, then the geometric and kinematic cuts were applied on the charged pions and each gamma separately. If these cuts were satisfied for both gammas, 'loss' of a gamma ray was simulated.

The acceptance of the events where both charged pions and one gamma ray survived was calculated, and the 4-vectors of these particles were stored on magnetic tapes for later processing. Such tapes were made for the reactions corresponding to all four peaks in Fig.5-2.

To be able to compare the spectra of different variables calculated from the 4-vectors in these tapes with the spectra of corresponding variables calculated from the

4-vectors in the data summary tapes, we smeared the momenta and directions of the particles from the Monte-Carlo tapes according to the experimental resolution and then fitted to hypothesis $\pi^- p \to \pi^+ \pi^- \gamma n$ with the missing mass constrained at the neutron mass value.

By comparing the different distributions obtained from the Monte-Carlo generated 4-vector tapes in the way described above with the corresponding experimental distributions, we were able to understand the backgrounds better and to find new cuts (on momenta of charged pions, gamma ray energy and missing mass) to decrease the number of background events compared to the radiative decay signal. The detailed study of these cuts will be made in a later paragraph. The experimental acceptance will be the product of the acceptance for the events written on the Monte-Carlo 4-vector tapes with the fraction of events left after the final cuts. The acceptance for true radiative decay Monte-Carlo's have also to be corrected for the gamma ray not being converted in the lead converter. This is necessary to be consistent with a background simulating Monte-Carlo program, where the conversion efficiency of the Lead Converter is being taken into account, when simulating the "loss" of a gamma ray.

3.0 CONVERSION EFFICIENCY OF LEAD CONVERTER

The gamma conversion efficiency is highly dependent on the effective cutoff energy for observed secondary electrons. This cutoff energy is dependent on the position of the conversion in the converter and the energy and emission angle of electrons, and is very difficult to measure. Therefore, the value for the single gamma efficiency was taken as the average between an upper limit based on pair productions, and a lower limit from published Monte-Carlo results.

Using theoretical pair production cross section the conversion efficiency upper limit is given by [55]

$$1 - \exp\{-\mu_0 (RL)\}$$

where RL is the number of radiation lengths of converter and

$$\mu_0 = \frac{7}{9} - \frac{b}{3}$$

where $b = [18 \ln(183 * z^{-1/3})]^{-1} = -0.0069$ for lead and can be ignored as it is negligible.

For 1.6 radiation lengths of lead converter the upper limit for conversion efficiency will be 71.2%. The lower limit was obtained from published Monte-Carlo results for photon showers by Messel and Crawford [56]. The secondary cutoff energy for our detector lies somewhere below 10 Mev [1]. From the shower tables a value of 62.9% is predicted for a 10 Mev cutoff. We believe the parameters of our system lie between the two extremes, therefore the average was taken (67.1 ± 4.5)% with a systematic error covering the two limits.

4.0 STUDY OF THE BACKGROUNDS

As already discussed in previous paragraphs of this chapter, most of the background in our sample of the data (with two charged pions and one gamma ray detected) comes from the $\pi^- p \rightarrow \pi^+ \pi^- \pi^0 n$ events where one of the gamma rays from the $\pi^0 \rightarrow \gamma\gamma$ decay was not detected. A gamma ray would not be detected because of one or more of the following reasons:

a) The gamma failed to be accepted because of the geometrical acceptance of the experiment. These are mostly soft gamma rays at large angle with respect to the π^0 momentum vector.

b) The gamma ray did not get converted in the lead converter.

c) The two gamma rays went too close to each other and were seen as one in the spark chambers and in the lead glass array.

We have also investigated the possibility of a gamma ray from the π^0 having less than a 5 inch distance from the charged pion and being eliminated by out geometric cut - thus leaving us with a background one gamma event. We found that the fraction of the gamma rays "killed" because of this particular cut is very close to the theoretically calculated probability of a charged pion producing a δ-ray in the lead converter. About 75% of charged pions had a shower candidate that was less than 5 inches away from it and got eliminated. There is a 3% probability for a gamma ray from the π^0 being near a charged pion. It is not possible to separate this background from the true radiative decay events with a δ-ray produced by a charged pion less than five inches away from it (both have a shower candidate "killed" because of being near a charged pion). Instead this background is easily taken into account in the Monte-Carlo simulation of the $\pi^+\pi^-\pi^0$ with one gamma from the π^0 missing events.

Besides the background coming from the reaction $\pi^- p \to \pi^+\pi^-\pi^0 n$ there may also be background coming from the reaction $\pi^- p \to \pi^+\pi^- n$ accompanied by a spurious gamma created by noise in the detectors, cosmic rays or δ-rays. These events can be eliminated by a high gamma energy cut. Fig.5-3 shows the $\pi^+\pi^-\gamma$ mass spectrum with $E_\gamma > 1.5$ Gev cut after the one constraint (1C) fit requiring M_{rec} = 0.9396 Gev. In this plot there is less background than in the corresponding Fig.5-2, but there still is a considerable amount of background that comes from $\pi^+\pi^-\pi^0$ events. These events have to be eliminated before the true radiative decays can be studied. This background comes mainly from the following reactions:

$$\pi^- p \;\text{-->}\; (\eta \text{ or } \omega)\, n \qquad \text{(i)}$$
$$\quad \lfloor\!\to \pi^+\pi^-\pi^0$$
$$\qquad\quad \lfloor\!\to \gamma\gamma$$

$$\pi^- p \;\text{-->}\; A_2 \; n \qquad \text{(ii)}$$
$$\lfloor\!\to \rho^\pm \pi^\pm$$
$$\quad \lfloor\!\to \pi^\pm \pi^0$$
$$\qquad \lfloor\!\to \gamma\gamma$$

$$\pi^- p \;\text{-->}\; \rho^\pm \pi^\pm \, n \qquad \text{(iii)}$$
$$\lfloor\!\to \pi^\pm \; \pi^0$$
$$\quad \lfloor\!\to \gamma\gamma$$

$$\pi^- p \;\text{-->}\; \rho^0 \; \pi^0 \; n$$
$$\quad \lfloor\!\to \gamma\gamma$$
$$\lfloor\!\to \pi^+ \; \pi^-$$

$$\pi^- p \;\text{-->}\; \rho^- \; N^{*+} \qquad \text{(iv)}$$
$$\quad \lfloor\!\to \pi^+ \, n$$
$$\lfloor\!\to \pi^- \; \pi^0$$
$$\quad \lfloor\!\to \gamma\gamma$$

$$\pi^- p \;\text{-->}\; \rho^0 \; N^{*0}$$
$$\quad \lfloor\!\to n \; \pi^0$$
$$\lfloor\!\to \pi^+\pi^- \quad \lfloor\!\to \gamma\gamma$$

There may also be background events with an $\eta \text{ --> } \gamma\gamma$ decay rather than a $\pi^0 \text{ --> } \gamma\gamma$ decay as in the reactions

$$\pi^- p \rightarrow \eta' n \qquad (v)$$
$$\quad \mapsto \eta \pi^+ \pi^-$$
$$\qquad \mapsto \gamma\gamma$$

In each case one of the gamma rays will be missed for the reasons enumerated above.

The first and third peaks in the $\pi^+\pi^-\gamma$ invariant mass plot come from the reaction (i) and the "flat" background is due to the rest of the reactions.The reaction (ii), where the background is due to an A2 decay with one undetected gama ray, is mainly responsible for the background at higher masses ($M_{\pi\pi\gamma}$ > 1.Gev.).

In all these reactions the gamma energy spectrum will peak slightly lower than in the true radiative decay events since one of the gamma rays that comes from the π^0 decay was not detected. Thus the gamma ray energy cut $E_\gamma > 1.5$ Gev has reduced the number of such events too.

In the reaction (iv), since rho mesons are being produced dominantly by pion exchange, most of the background of this type should disappear by making a low transverse momentum cut:

$$|t'| = |t - t_{min}| > 0.2\ (\mathrm{Gev/c})^2$$

Also in all the reactions the energy of the gamma ray which failed to convert or failed to be within the geometrical acceptance of the apparatus will be added to the neutron energy. So a high cut on the kinetic energy of the missing mass T_{MM} < 0.22 Gev (T_{MM} is approximately equal to $|t'|/2m$) should also reduce the background coming from the reactions (i-v). The values at which the cuts were made on the $|t'|$ and T_{MM} were found by comparing the true radiative decay Monte-Carlo, $\pi^+\pi^-\pi^0$ background Monte-Carlo and the data spectra for $|t'|$ and T_{MM} for different peaks in Fig.5-3 and also for all the data from Fig.5-3.

Fig.5-4 shows the 1C fitted $M_{\pi\pi\gamma}$ spectrum with the cuts $|t'| > 0.2$ $(Gev/c)^2$ and $T_{MM} < 0.22$ Gev.

Now we compare the Monte-Carlo single particle spectra and data for the charged pions. Fig.5-5 and Fig.5-6 show the experimental and Monte-Carlo kinetic energy distributions for the positive pion correspondingly for the $\eta \to \pi\pi\gamma$ decay. Fig.5-7 and Fig.5-8 show same distributions for the $\eta' \to \pi\pi\gamma$ decay. The Monte-Carlo spectra are normalised to the number of events of the corresponding data spectra. The average charged pion kinetic energy in a background event is lower than in a radiative decay event since a gamma ray was "lost". Also in the reactions (iii) and (iv) where the π^+ is produced at the recoil vertex (with small $|t'|$) it is expected to have considerably lower kinetic energy than the π^+ coming from a radiative decay event. As expected in Fig.5-5, 5-6, 5-7 and 5-8 one can see disagreement between experimental and Monte-Carlo charged pion energy spectra for low energies ($T_{\pi^\pm} < 1.0$ Gev). Fig.5-11 shows the 1C fitted $M_{\pi\pi\gamma}$ spectrum with cuts on the charged pion kinetic energy $T_{\pi^\pm} >$

1.0 Gev. The comparison of the Fig.5-9 with the Fig.5-4 shows that cuts on the charged pion kinetic energy have not only reduced the backgrounds in the $\eta \to \pi\pi\gamma$ and $\eta' \to \rho\gamma$ regions, but also reduced considerably the backgrounds η, $\omega \to \pi^+\pi^-\pi^0$ with one gamma ray missing. As in the high gamma energy cut, the cut on charged pion energy has reduced the number of all backgrounds (i-v) because the charged pions in these reactions (especially in reaction v) have lower average energies than in the true radiative decay events.

The last cut we made to reduce the backgrounds was to demand that the χ^2 probability of the 1C fit $\chi^2_{prob} > 0.1$. The χ^2 probability is the measure of how close the missing mass is to the neutron mass, i.e. how well the events agree with the final data sample (with all the cuts discussed above).

As it can be seen from Fig.5-10 in the mass region $M_{\pi\pi\gamma} < 1.05$ Gev all background except the backgrounds of the type (i) (η and $\omega \to \pi^+\pi^-\pi^0$) are reduced to negligible amounts.

In the mass region $M_{\pi\pi\gamma} > 1.05$ Gev/c the background comes mainly from the reaction (ii) and since the A_2 has a large width ($\Gamma_{A_2} = 0.102$ Gev) these background events cover a wide mass range. This makes it impossible to separate, from the background coming from the reaction (ii), possible $f \to \rho\gamma$ radiative decay events [9,10,46]. Also since our experimental acceptance decreases for high $M_{\pi\pi\gamma}$ values we will study only the mass region $M_{\pi\pi\gamma} < 1.05$ Gev/c .

Table 5-2 shows the number of events on the original DST tape (with the cuts from the table 5-1) and the number of events left after each stage of the cuts.

After all the cuts, only about 10% of all events have survived. The peak to background ratio in the η' region has improved from 2.7 in the original DST events (Fig.5-2) to 11 in the final data sample (Fig.5-10).

Table 5-3 gives the Monte-Carlo calculated acceptances for the different backgrounds (η, ω --> $\pi^+\pi^-\pi^0$ with one gamma missing) and different possible radiative decays (η, ω, η' --> $\pi^+\pi^-\gamma$) after all the cuts from Fig.5-10 were applied. The acceptances for the radiative ($\pi^+\pi^-\gamma$) decays after all the cuts are approximately 3 times better than the acceptances for $\pi^+\pi^-\pi^0$ decay for the same mesons. Different tests with Monte-Carlo simulation programs lead us to believe that the error in the acceptance calculation is 7%. This includes the error for gamma conversion efficiency.

Since we were not able to eliminate the $\pi^+\pi^-\pi^0$ (with one gamma missing) background, we will have to use Monte-Carlo simulated background spectra in the fits to the data $\pi^+\pi^-\gamma$ mass spectrum.

We now proceed to study this Monte-Carlo simulated background to get an estimate of its stability and reliability.

5.0 STUDY OF THE MONTE-CARLO SIMULATED BACKGROUNDS

In the Monte-Carlo simulation programs of the $\pi^+\pi^-\pi^o$ (with one gamma missing) background, in the sections where the generation of the 4-vectors is done, the geometric, kinematic and trigger constrains are applied, the charged pion decay in flight and the charged pion and gamma ray interaction in the target are simulated, the physics of the reaction and experimental setup are explicitly taken into account. In the part where the simulation of loss of a gamma ray is done, when both gamma rays survive the geometrical cuts, one has to go beyond the arguments used there to estimate the correction factor made by the offline analysis program. In these events the detectors have seen only one gamma ray, but both gamma rays have deposited energy in the lead glass. The off-line analysis program made a correction assuming that there was one high energy gamma ray instead of two lower energy gamma rays in the lead glass. We tried to estimate this correction factor used by the off-line analysis program by fitting the data $\pi^+\pi^-\gamma$ mass spectrum and Monte-Carlo simulated mass spectra for $\eta, \omega \to \pi^+\pi^-\pi^o$ (with one gamma missing), where parameters were used to calculate the fraction of energy deposited by a gamma ray in the lead glass as described in the Appendix A.

Fig.5-11(a-f) show the results of the fits where different fractions of energy deposited by a gamma ray were used in the Monte-Carlo program for each plot, when the two gamma rays were close enough to deposit their energy in one lead glass block. In all these plots the $\omega \rightarrow \pi^+\pi^-\pi^0$ (with one gamma missing) Monte-Carlo mass spectrum fits well with the corresponding data spectrum, but the more sensitive $\eta \rightarrow \pi^+\pi^-\pi^0$ (with one gamma missing) Monte-Carlo mass spectrum peaks higher than the corresponding data spectrum. Therefore we try to estimate an overall gamma energy correction factor for all 'detected' gamma rays (even when the two gamma rays were not close enough) to obtain better fits for the $\eta \rightarrow \pi^+\pi^-\pi^0$ (with one gamma missing) peak and see how this affects the ω mass peak. This overall gamma energy correction factor is used in addition to the parameters used to get the best one of the above fits (Fig.5-11c).

This is shown in Fig.5-11(g-j), where in each plot a different overall correction factor was used. Again the fits in the ω mass region did not change significantly, while in the η mass region the Monte-Carlo peak gets shifted to the correct mass and beyond.

All this leads us believe that the $\omega \rightarrow \pi^+\pi^-\pi^0$ (with one gamma missing) Monte-Carlo $\pi\pi\gamma$ mass spectrum is not very sensitive to the gamma energy correction factors. All physically meaningful gamma energy correction factors shift the centre of this peak by less than 5 Mev (half channel width).

We decided to use the parameters which give the best fits to the omega mass spectrum (i.e. parameters from Fig 5-11c), since we were not interested in studying the eta mass region, where other experiments have better statistics and resolution.

In all the above fits gaussians were used for the bonafide $\eta \to \pi^+\pi^-\gamma$ radiative decay events and for possible $\omega \to \pi^+\pi^-\gamma$ decay events, and in all of them the number of $\omega \to \pi^+\pi^-\gamma$ events was found to be zero. We want to be sure that this limit is not due to some calibration uncertainties. We make the following observations:

(i) We already saw that the $\omega \to \pi^+\pi^-\pi^0$ (with one gamma missing) background peak can have less than 5 Mev shift (possibly towards higher masses) when we demand the correct η mass location.

(ii) The fits to the $\eta \to \pi^+\pi^-\gamma$ peak give eta meson mass identical to Particle Data Book value, but the fits to the $\eta' \to \rho\gamma$ peak show that the eta prime meson mass in our experiment is about 3 Mev less than the Particle Data Book value. This means that the omega radiative decay peak could be shifted down by maximum 3 Mev because the η' and ω are so near to each other in mass.

(iii) There could be a worse case scenarios when the background and radiative $\pi^+\pi^-\gamma$ peaks are shifted relative to each other.

Fig.5-12a shows a fit where omega background peak is shifted down by one channel (10 Mev). There are 106 omega radiative decay events in this fit, but the χ^2_{PDF} of this fit is 2.01, corresponding to confidence limit of less than 10^{-4} which is unacceptable. In fig 5-12b we have shifted the omega radiative decay peak centre down by 10 Mev (the background peak is not shifted). In this fit there are 16 radiative decay events and the χ^2 per degree of freedom is 1.1, but from (i) and (ii) we know that 10 Mev mass shift is very unlikely. Therefore we argue a very high level of confidence for the limits we quote for the $\omega \rightarrow \pi^+\pi^-\gamma$ radiative decay.

CHAPTER 6. EXPERIMENTAL RESULTS

Using the number of events due to different reactions in the final sample of events presented in Fig 5-10 a number of quantities can be obtained for the radiative decay of mesons.

We get the number of events due to different reactions by fitting the spectrum of Fig 5-10 ($M_{\pi\pi\gamma}$ < 1.045 Gev) with;

1) The Monte-Carlo generated mass spectra for $\eta \to \pi^+\pi^-\pi^0$ and $\omega \to \pi^+\pi^-\pi^0$ with one gamma missing events,

2) A gaussian for the $\eta \to \pi^+\pi^-\gamma$ events,

3) A gaussian for $\omega \to \pi^+\pi^-\gamma$ events,

4) A gaussian for $\eta' \to \rho\gamma$ events and

5) A parabolic background.

Fig 6-1 shows the results of this fit in the region $M_{\pi\pi\gamma}$ < 1.045 Gev. According to this fit the number of events in each channel are:

$$N_{\eta\to3\pi} = 291$$

$$N_{\eta\to\pi\pi\gamma} = 135$$

$$N_{\omega\to3\pi} = 1271 \qquad (6\text{-}1)$$

$$N_{\omega\to\pi\pi\gamma} = 0$$

$$N_{\eta'\to\rho\gamma} = 434$$

with a confidence limit (C.L.) of 80%. In this fit it is possible to allow for a non-zero number of radiative decays of omega meson as follows:

$$N_{\omega\to\pi\pi\gamma} = 25 \text{ with C.L. } > 90\%$$

$$N_{\omega\to\pi\pi\gamma} = 50 \text{ with C.L. } > 96\%$$

Fig.6-2 and 6-3 are fits of experimental gamma energy (E_γ) and $\pi^+\pi^-$ invariant mass ($M_{\pi^+\pi^-}$) to the Monte-Carlo generated spectra of E_γ and $M_{\pi^+\pi^-}$ for different contributing channels, scaled to the number of events (6-1) calculated from the fit to $M_{\pi^+\pi^-}$ and a parabolic background. The good agreement between the experimental and Monte-Carlo E_γ and $M_{\pi^+\pi^-}$ distributions gives us additional confidence that the backgrounds in our data are understood.

Now we proceed to study the radiative decays of different mesons separately.

Since all the decay modes of the eta mesbn are very well studied we will use the events coming from $\eta \to \pi^+\pi^-\gamma$ decay (the second peak in Fig 5-10) as normalisation for all the $\pi^+\pi^-\gamma$ data sample. We can do this since the cuts discussed in chapter 5 have left us with a data sample that has close enough gamma energies and charged pion momenta for the $\pi^+\pi^-\gamma$ invariant masses of interest. We thus expect to ignore the mass dependence of the experimental corrections in the mass range of interest. For the $\pi^+\pi^-\gamma$ data it is difficult to estimate accurately these corrections since most of this data was collected with a "two gamma" trigger (demanding two no-yes pairs at the gamma hodoscope), one of which was found to be spurious by the off-line analysis program.

We will concentrate on two mass ranges:

1) In the mass range 0.6 < $M_{\pi\pi\gamma}$ <0.8 Gev, we study $\omega \rightarrow \pi\pi\gamma$ decay mode.

2) In the mass range 0.9 < $M_{\pi\pi\gamma}$ < 1.0 Gev we will study the decay $\eta' \rightarrow \rho\gamma$. Also we will check for the existence of the resonance M(953) [43,44,45].

1.0 STUDY OF THE DECAY $\omega \rightarrow \pi\pi\gamma$

The charge conjugation quantum number for the ω meson is C=-1 which implies that the decay $\omega \rightarrow \pi^+\pi^-\gamma$ is electromagnetically allowed [48]. While the decay $\omega \rightarrow \pi^0\gamma$ proceeds as a magnetic dipole (M1) transition, the lowest configuration for the $2\pi\gamma$ decay is realized by an electric quadrupole (E2) transition with the two pions in a relative S state. The magnetic dipole transition with two pions in a P state cannot occur in the decay $\omega \rightarrow (2\pi) + \gamma$ because of the following reasons;

(i) If both pions are π^{0}'s, they cannot be in P-state, because two identical, spin 0 bosons (obeying Bose statistics) have to have even space symmetry (l=0,2,...)

(ii) When $\omega \rightarrow \pi^{+}\pi^{-}\gamma$ the charge conjugation quantum numbers for γ and ($\pi^{+}\pi^{-}$) system are; $C(\gamma)=-1$ and $C(\pi^{+}\pi^{-})=P=(-1)^{\ell}$. Since $C(\omega)=-1$, the charge conjugation invariance of electromagnetic decays will allow only even l values for the $\pi^{+}\pi^{-}$ system to make $C(\pi^{+}\pi^{-})=+1$.

Also since ω^{0} has isospin equal to zero ($t_{\omega}=0$), in this decay the two pions are restricted to the isospin zero state. This determines the following relation [50];

$$\Gamma(\omega \rightarrow \pi^{+}\pi^{-}\gamma) = 2\,\Gamma(\omega \rightarrow \pi^{0}\pi^{0}\gamma)$$

Different models are used in ref. [48,49,50] to calculate the width $\Gamma(\omega \rightarrow \pi\pi\gamma)$. All these models predict an upper limit for branching ratio $Br(\omega \rightarrow \pi\pi\gamma)$ which is considerably smaller than the existing experimental upper limit [$Br(\omega \rightarrow \pi\pi\gamma) < 5\%$]. All the models use the width $\Gamma(\rho \rightarrow \pi\gamma)$ to calculate the width of the $\omega \rightarrow \pi\pi\gamma$ radiative decay. The theoretical predictions for the width $\Gamma(\rho \rightarrow \pi\gamma)$ (ref. [7-29]) do not agree with each other and also with the particle data book value for $\Gamma(\rho \rightarrow \pi\gamma)$. A recent experiment [51] has obtained a value for $\Gamma(\rho \rightarrow \pi\gamma)$ which is close to some of the theoretical predictions. Since the value of the width $\Gamma(\rho \rightarrow \pi\gamma)$ is not certain, an estimate of the width $\Gamma(\omega \rightarrow \pi\pi\gamma)$ using the models from ref [48,49,50] cannot be made.

Using our results (6-1) we will set a new upper limit for the branching ratio Br($\omega \to \pi\pi\gamma$). Our result can be compared with the models from ref. 48,49,50 when the value for the width $\Gamma(\rho \to \pi\gamma)$ is more definite.

The upper limit for the branching ratio of the decay $\omega \to \pi^+\pi^-\gamma$ is found in the following way;

$$Br(\omega \to \pi^+\pi^-\gamma) = Br(\omega \to \pi^+\pi^-\pi^o)\,\frac{N_{\omega\to\pi^+\pi^-\gamma}}{N_{\omega\to\pi^+\pi^-\pi^o}}\,\frac{Acc(\omega\to\pi^+\pi^-\pi^o)}{Acc(\omega\to\pi^+\pi^-\gamma)}$$

Using the number of events $N_{\omega\to\pi^+\pi^-\gamma}$ and $N_{\omega\to\pi^+\pi^-\pi^o}$ obtained from the fit to the mass spectrum and the acceptances $Acc(\omega \to \pi^+\pi^-\pi^o)$ and $Acc(\omega \to \pi^+\pi^-\gamma)$ from the Table 5-3 we get;

$$Br(\omega \to \pi^+\pi^-\gamma) < 0.67\% \quad (\text{C.L.} > 90\%)$$

This value is almost an order of magnitude smaller than the previous upper limit (5%) for the branching ratio $Br(\omega \to \pi^+\pi^-\gamma)$. It is also closer to the theoretical predictions [49,50] if we use the most recent experimental value for the decay width $\rho \to \pi\gamma$.

2.0 STUDY OF THE DECAY $\eta' \to \rho\gamma$

The radiative decay $\eta' \to \rho\gamma$ occurs via M1 photon emission. The quark model theory of such decays is described in Appendix B. Different models predict different values for $\Gamma_{\eta'\to\rho\gamma}$ ranging in wide limits between 10 Kev and 643 Kev [6]-[29]. The models that predict M1 decay rates of other mesons in close agreement with experimental values (ref. [7,8,9,10,16,24,28]) predict a value between 77 Kev and 150 Kev. Experimentally this decay has been observed many times (ref. [31-42]). Ref. [31-40] have only been able to measure branching ratios of different decays of the η' meson. The particle data book value for $\eta' \rightarrow \rho\gamma$ branching ratio is 29.8 ± 1.6% .

This would make the theoretically expected total width $\Gamma_{\eta'}$ to be approximately 500 Kev, which is too small compared with experimental resolution of all the experiments in ref. [31-40].

D.M.Binnie et al [41] measured the total η' width, by observing threshold production of η' mesons in the reaction $\pi^- p \rightarrow \eta' n$. In this experiment the resolution is small enough to allow the extraction of the η' meson total width from the observed width.

G.S.Abrams et al, the JADE Collaboration and the CELLO Collaboration in DESY [42] observed η' mesons in the two photon reaction

$$e^+e^- \rightarrow \gamma\gamma\, e^+e^- \rightarrow \eta'\, e^+e^-$$

Here the production cross section is proportional to the $\eta' \rightarrow \gamma\gamma$ partial width and using the branching ratio value they calculated the total width. Our experimental resolution is also not good enough to measure the width $\Gamma_{\eta'}$, but since it is a high statistics counter experiment with very little background in η' mass region (Fig 6-4), our experiment will provide a significant, independent measurement of the branching ratio $Br(\eta' \to \rho\gamma)$. Note that there is a disagreement between the value of this branching ratio calculated in the earlier experiments [35,36,37] and the later experiments [38,39], and the only calculation of the branching ratio with data statistics compatible to ours is made by J.S.Danbury et al [38] by observing mesons produced in the reaction $K^- p \to \eta' \Lambda$.

The branching ratio $Br(\eta' \to \rho\gamma)$ is going to be calculated by normalising it with the number of $\eta \to \pi^+\pi^-\gamma$ events in the same sample of data. This is better than using $\eta' \to \eta\pi^+\pi^-$ ($\eta \to \gamma\gamma$) events from the two gamma data sample of our experiment, since the experimental corrections for the event topology with one gamma and two gammas are different. For $\eta \to \pi^+\pi^-\gamma$ and $\eta' \to \rho\gamma$ these corrections will cancel if we ignore the expected small mass dependence of these corrections. Thus

$$Br(\eta' \to \rho\gamma) = Br(\eta \to \pi^+\pi^-\gamma)\ \frac{Acc(\eta \to \pi^+\pi^-\gamma)}{Acc(\eta' \to \rho\gamma)}\ \frac{N(\eta')}{N(\eta)}\ \frac{\sigma^{tot}(\eta)}{\sigma^{tot}(\eta')} \qquad (6-2)$$

$\sigma^{tot}(\eta)$ and $\sigma^{tot}(\eta')$, the total η and η' production cross sections, are obtained from our experiment as described in ref [47]. The acceptances ($Acc(\eta \to \pi^+\pi^-\gamma)$ and $Acc(\eta' \to \rho\gamma)$) are calculated by the Monte-Carlo programs (table 5-3), and $Br(\eta \to \pi^+\pi^-\gamma)$ is taken from the particle data book. Substituting all these values into (6-2) we will get:

$$Br(\eta' \to \rho\gamma) = 30.8 \pm 4.9\%$$

The error includes the 7% error for the $\sigma^{tot}(\eta)$ and $\sigma^{tot}(\eta')$ from [47], acceptance error of 5% (ref. [47]) and statistical error for $N_{\eta\to\pi^+\pi^-\gamma}$ and $N_{\eta'\to\rho\gamma}$. Our value for the branching ratio $Br(\eta' \to \rho\gamma)$ is in excellent agreement with the particle data book value as well as with the values obtained by Danbury et al [38] and Jacobs et al [39]. In all calculations so far the $\pi\pi\gamma$ peak at 0.955 Gev was considered to be due $\eta' \to \rho\gamma$ decay. Now we try to study this further.

3.0 THE M(953) MESON

Fig 6-4 is the distribution of $M_{\pi\pi\gamma}$ for all events with $M_{\pi^+\pi^-}$ in the ρ-band, i.e. $0.65 < M_{\pi^+\pi^-} < 0.85$ Gev. Fig 6-5 is the same distribution but with $M_{\pi^+\pi^-} < 0.65$ Gev. Fig 6-6 is the Monte-Carlo $M_{\pi^+\pi^-}$ P-wave Breit-Wigner distribution from $\eta' \to \rho\gamma$ simulation.

The ratio of number of events in the peak at 0.955 Gev in Fig 6-4 and 6-5 is consistent with the ratio in Fig 6-6 of the number of events with $0.65 < M_{\pi^+\pi^-} < 0.85$ Gev and the number of events with $M_{\pi^+\pi^-} < 0.65$ Gev.

This shows that almost all events are accounted for by the decay mode $\eta' \to \rho\gamma$. We do not need to postulate a particle M of mass 0.953 (as in ref. [36, 37 and 43]) decaying directly into $\pi^+\pi^-\gamma$.

SECTION 2. STUDY OF THE EVENTS $\pi^- p \rightarrow \pi^+\pi^- 3\gamma n$

CHAPTER 7. CHANGES IN THE APPARATUS AND FINAL EVENT SELECTION FOR $\pi^+\pi^-3\gamma$ TOPOLOGY

1.0 KINEMATICS

The radiative decays of mesons into $\omega\gamma$ and $\eta\gamma$ can be studied using the sample of events where two charged pions and three gamma rays were found. To select a sample of events for this study we have applied the same geometric cuts of Chapter 5 on all the detected particles. The kinematic cuts on the charged pions and gamma ray not associated with the π^0 were also the same as for the selection of the $\pi^+\pi^-\gamma$ events (Table 5-1) for the reasons discussed in chapter 5. The two gamma rays that come from the π^0 decay do not need to have such a high energy cut (0.700 Gev) as the bachelor gamma ray since their energy calibration can be checked by looking at the π^0 mass spectrum. We applied a 0.400 Gev cut on these gamma rays. In this topology there can be three types of background events;

$$
\begin{array}{l}
1.\ \pi^- p \to \text{Meson} + n \\
\qquad\qquad\qquad \lfloor\!\to \pi^+\pi^-\pi^0 \\
\qquad\qquad\qquad\qquad\quad \lfloor\!\to \gamma\gamma
\end{array}
$$

accompanied by a spurious gamma ray,

2. $\pi^- p \to \text{Meson} + n$

$$\text{Meson} \to \pi^+\pi^-\pi^0\ \pi^0, \quad \pi^0 \to \gamma\gamma, \quad \pi^0 \to \gamma\gamma$$

with one gamma ray undetected,

3. $\pi^- p \to \text{Meson} + N^{*0}$

$$\text{Meson} \to \pi^+\pi^-\pi^0, \quad \pi^0 \to \gamma\gamma; \qquad N^{*0} \to n\pi^0, \quad \pi^0 \to \gamma\gamma$$

with one gamma ray undetected.

To decrease the number of events of the type (1) a missing mass squared cut of $M^2_{rec} > 0\ \mathrm{GeV}^2$ was applied, and to decrease the number of events of the types (2,3) the cut $M^2_{rec} < 1.6\ \mathrm{GeV}^2$ was applied. Table 7-1 shows the summary of the cuts for this data sample.

Most of the events selected in this way were found to be coming from the reaction

$$\pi^- p \to \eta' n, \quad \eta' \to \omega\gamma, \quad \omega \to \pi^+\pi^-\pi^0$$

or a background associated with the ω meson. This is because our experimental acceptance of $\pi^+\pi^-\pi^0$ invariant mass is considerably larger in ω meson mass region than in η meson mass region. A detailed study of the $\eta' \to \omega\gamma$ decay is done elsewhere [4].

We want to separate events where the $\pi^+\pi^-\pi^0$ form an η meson to study the radiative decays of rho and omega mesons into $\eta\gamma$. Using data of experiment E397 in a preliminary study of the events with $\pi^+\pi^-\pi^0$ invariant mass in the η meson mass range only 6-7 events were found that could come from $\rho(\omega) \rightarrow \eta\gamma$ decay.

To collect more multi-gamma events (events with more than two gamma rays) there were some changes made in our experimental apparatus to increase the multi-gamma ray detection efficiency, and two new experiments (E420, E428) were conducted.

We first study the changes in the experimental apparatus, corresponding changes in analysis programs, and the effects of these changes on the data.

2.0 EXPERIMENTS E420, E428

a) Experimental apparatus.

As compared with the experiment E397 discussed above, the following changes were made to the beam, charged track and gamma ray sections of the apparatus:

1. Beam:

To remove the late beam particles, a 10 finger hodoscope (BH10) located immediately in front of beam chamber 1 and rotated 45 degrees to the normal was added.

2, Charged particle:

The charged particle spectrometer was the same except that in the charged particle part of the triggering system the HO scintillation counter was replaced by a Proportional Wire Chamber. In the previous experiments the HO counter could not detect charged tracks leaving the target at an angle less than 4 degrees. This was cutting out a fraction of low transverse momentum events.

The Proportional Wire Chamber (PWC) was hardwired into 16 independent strips, whose respective widths were chosen by Monte-Carlo simulation to maximize the trigger rate for all transverse momenta. It served as a 16-element hodoscope and demanded that only 2 or 3 charged particles be detected. The PWC helped avoid triggers caused by back-scattered particles from the lead converter in the H2 hodoscope. The PWC is described in detail in Fig.7-1.

3. Gamma ray:

In the gamma ray detector more lead was added to increase the conversion probability of the gamma rays, allowing us to detect more multi-gamma events. In front of the first gamma spark chamber the lead converter thickness was increased from 1.6 radiation lengths to 2.07 radiation lengths (0.5 inches). In addition, an aluminum plate (used as support for the lead) contributed 0.1 radiation lengths. Also between the first and second gamma spark chambers there were added additional 1.14 radiation lengths of lead (0.25 inches) and 0.07 radiation lengths of aluminum. The total conversion probability of this assembly for one gamma ray was 89%, instead of the 67% conversion probability of the previous experiments. Also more Borer scalers were added to handle 12-16 sparks (insted of 8-12 as before) in each plane to ensure high efficiency for multi-spark events.

b) Data analysis

A larger event buffer (328 16-bit words) was necessary for each event after the changes in the trigger requirements (2 or 3 charged tracks) and the apparatus for the gamma ray detection system. Both online and offline analysis programs were modified to use the information in the new buffer, but the event reconstruction techniques stayed the same.

At the tuning stage a different method was used to finetune the charged particle momenta and positions. A quintic spline fit, described in detail in reference [3] was used. This method improved the charged track resolution by 20%.

c) Experimental Resolution

After the fine tuning of the data, the experimental resolution of the beam and charged track momentum and position were found to be the same [3], but the gamma energy resolution was changed. Because of the extra lead converter, more energy is lost in the converter and the fluctuations in the lead glass are bigger. This made the reconstruction of the gamma ray energy more difficult.

As in previous experiments the gamma ray energy error was obtained using the di-gamma mass spectra for different gamma energy bins. The energy uncertainty as a function of energy was fitted to the following form [3];

$$\Delta E/E\ (FWHM) = 0.073 + 0.181/\sqrt{E}$$

The gamma ray position error did not change, since at the first shower spark chamber, where the shower position is mainly determined, the showers are not spread wider than in previous experiments.

3.0 ANALYSIS OF THE REACTION $\pi^- p \rightarrow \eta\gamma n$

From the data collected in the experiments E420, E428 a sample of events for the study of the reactions

$$\pi^- p \rightarrow \rho(\omega) n, \quad \rho(\omega) \rightarrow \eta\gamma$$

was selected using the kinematic and geometric cuts from the Table 7-1 and the cut $M_{\pi^+\pi^-\pi^o} < 0.65$ Gev to enrich the sample of events where the $\pi^+\pi^-\pi^o$ came from the eta decay. Fig.7-2 shows the $\pi^+\pi^-\pi^o$ invariant mass spectrum for these events with one constraint fit requiring $\gamma_1\gamma_2$ invariant mass to be equal to neutral pion mass ($M_{\gamma_1\gamma_2}$ = 0.1349 Gev). After the 1C fit in Fig.7-2 a sharp peak can be seen at eta meson mass. Fig.7-3 shows the invariant mass of $\pi^+\pi^-\pi^o\gamma$ (hereafter called M_{mes}). The whole spectrum in Fig.7-3 peaks around 0.8 Gev. However this cannot be taken to be a significant indication of $\rho(\omega)$ signal. We first try to find additional cuts (to be described in the section 5.0) to reduce the background low enough, to be able to study radiative decays $\rho\ (\omega) \rightarrow \eta\gamma$. As before one of the ways of finding cuts will be the comparison of Monte-Carlo simulated spectra to the corresponding data spectra. We also did a three constraint (3C) fit to this data sample, requiring;

1. $\gamma_1\gamma_2$ invariant mass to be equal to π^0 mass ($M_{\gamma_1\gamma_2}$ = 0.1349 Gev)

2. Missing mass to be equal to neutron mass (M_{rec} = 0.9396 Gev)

3. $\pi^+\pi^-\pi^0$ invariant mass to be equal to eta mass ($M_{\pi^+\pi^-\pi^0}$ = 0.5488 Gev)

This procedure sharpens the peaks that agree with the fit hypothesis and does little to the background spectra.

It is important to remember that the reconstruction programs have ordered the gamma rays so that the first two showers come (with higher probability) from the π^0 with energies in decreasing order ($E_{\gamma_1} > E_{\gamma_2}$). We have also found that invariant masses of $\gamma_1\gamma_2$ and $\gamma_2\gamma_3$ contain only about 10% of all π^0's and we will take this into account in the end as an experimental correction.

4.0 EXPERIMENTAL ACCEPTANCE

For the study of the data sample where three gamma rays were detected we modified the Monte-Carlo simulation programs simulating radiative decays of mesons into $\pi^+\pi^-\gamma$ (described in Appendix A) to simulate the interactions

$$\pi^- p \to \rho\ (\omega)\, n$$
$$\quad\quad \hookrightarrow \eta\ \gamma$$
$$\quad\quad\quad \hookrightarrow \pi^+\pi^-\pi^0$$

And to take into account the changes in the apparatus (i.e. the PWC instead of the HO counter).

The 4-vectors were generated using the same routines described in Appendix A. Then the interactions of the charged pions and all three gamma rays with the hydrogen target and the decay of charged pions in flight were simulated. For the events, where all the particles survived, the geometric and kinematic cuts were applied. The 4-vectors of the remaining events were stored on a magnetic tape and the acceptance of such events was calculated.

The 4-vectors from these tapes were smeared using experimental resolution and 3C fitted to obtain the experimental resolution of different kinematic variables. Also the spectra of different variables at different fitting steps were compared with corresponding spectra from the data sample to help us find additional cuts to separate the $\rho(\omega) \to \eta\gamma$ decay radiative decay events from the background. We will discuss the additional cuts in the next paragraph.

The experimental acceptance of the remaining $\rho(\omega) \to \eta\gamma$ radiative decay events will be the product of the acceptance of the events written on the Monte-Carlo 4-vector tapes with the fraction of events left after the final cuts.

5.0 STUDY OF THE BACKGROUND

As already mentioned, two major types of backgrounds are possible in the three gamma data sample (events with π^+, π^- and three gamma rays detected):

1. $\pi^- p \to \pi^+ \pi^- \pi^o n$
$$\pi^o \to \gamma\gamma$$

with one spurious gamma ray (created by the noise in the detectors or the analysis programs).

2. $\pi^- p \to \pi^+ \pi^- \pi^o \pi^o n$
$$\pi^o \to \gamma\gamma, \quad \pi^o \to \gamma\gamma$$

with a gamma ray from one of the π^o's not detected.

The detailed discussion in Chapter 5 applies to the three gamma data sample as well in so far as gamma ray detection is concerned. In the case of one gamma data we made a high gamma energy cut to eliminate background with a spurious gamma ray and to reduce the number of events with one lost gamma ray. In the case of the three gamma data the gamma energy cuts cannot be so high, since the average gamma energy is smaller in this data sample.

Figures 7-4, 7-5, 7-6 and 7-7 are the Monte-Carlo simulated 3C fit gamma ray energies and π^0 energy (E_{γ_1}, E_{γ_2}, E_{γ_3}, E_{π^0}) respectively for the reaction;

$$\pi^- p \rightarrow \rho n$$
$$\hookrightarrow \eta \gamma_3$$
$$\hookrightarrow \pi^+ \pi^- \pi^0$$
$$\hookrightarrow \gamma_1 \gamma_2$$

Figures 7-8, 7-9, 7-10, 7-11 are the same distributions for the three gamma data sample. From the comparison of these figures we can see that except for E_{γ_3} spectra (7-6 and 7-10) the data spectra and corresponding Monte-Carlo spectra look very similar. There are no obvious cuts for E_{γ_1}, E_{γ_2} and $E_{\gamma_1\gamma_2}$ that can eliminate background without losing many radiative decay events.

From the study of one gamma events we already know, that one of the reasons for "losing" a gamma ray is that it went in the same lead glass block with a "seen" gamma ray, making its energy higher. On the other hand if in a background event one of the π^0's came from an N^* decay and the gamma ray from the other π^0 was "lost" then we would have an event with a low energy π^0 and thus low energy γ_1 and γ_2. To minimize background with two gamma rays in the same block we should make cuts on high side of the spectra in Fig.7-8, 7-9, 7-10, 7-11 and to minimize background with an N^* we should make cuts on low side of the spectra in these figures.

For E_{γ_1}, E_{γ_2} and E_{π^o} we make very loose cuts;

$$0.6 < E_{\gamma_1} < 3.2 \text{ Gev}$$

$$0.4 < E_{\gamma_2} < 2.0 \text{ Gev}$$

$$1.0 < E_{\gamma_1\gamma_2} < 4.5 \text{ GEv}$$

since they are so similar to Monte-Carlo spectra.

For E_{γ_3} the comparison of Fig.7-6 and 7-10 shows there is larger number of low energy γ_3's in the data sample. These γ's could be coming from an N^* whose decaying π^o lost a gamma ray or they may be spurious. To discriminate against these events we make the cut

$$1.0 < E_{\gamma_3} < 4.5 \text{ Gev}$$

In this data sample there are only 1265 events (Fig.7-3) and we have to make a compromise between a very tight cut and statistics. We also have to make a cut around the η mass to reduce a large fraction of background, where the π^+, π^-, π^o do not come from an eta meson decay.

$$M_{\pi^+\pi^-\pi^o} \; 1C < 0.60 \text{ Gev}$$

Fig.7-12, 7-13, 7-14 and 7-15 are the $M_{\gamma_1\gamma_2}$, $M_{\pi^+\pi^-\pi^o}$, $M_{\pi^+\pi^-\pi^o}$ 1C and M_{mes} (the invariant mass of $\pi^+\pi^-\pi^o\gamma$) spectra respectively after all the above cuts. Fig.7-16 is the M_{mes} spectrum after the 3C fit with the same cuts. Fig.7-15 has an enhancement around 0.8 Gev which after the 3C fit (Fig.7-16) has become a sharp ρ-ω peak. In this data sample there still is a large number of background events.

From Fig.7-12 it is clear that we need to make the cut $0.105 < M_{\gamma_1\gamma_2} < 0.165$ Gev to isolate events with a π^0 in the final state, and from Fig.7-14 one can see that a tighter $M_{\pi^+\pi^-\pi^o}$ 1C < 0.58 Gev cut can be made to reduce background not associated with eta meson. Fig.7-17 is the M_{mes} 3C fit spectrum after these cuts.

Fig.7-18 is the missing mass squared ($Mrec^2$) spectrum after these cuts and Fig7-18a is the Monte-Carlo simulated 3C fit ($Mrec^2$) for the reaction

$$\pi^- p \longrightarrow \rho n$$
$$\rho \rightarrow \eta\gamma$$
$$\eta \rightarrow \pi^+\pi^-\pi^o$$

Fig.7-19 is M_{rec} spectrum only for the events in the $\rho(\omega)$ mass region ($0.72 < M_{mes} < 0.88$ Gev). For these events one can "see" a separate neutron mass squared peak. From these plots it is clear that we can reduce most of the background with the cut;

$$0.5 < M^2_{rec} < 1.2 \text{ Gev}^2$$

Fig.7-20 shows the M_{mes} 3C fit spectrum for the final data sample with all above cuts. In this sample there are 152 events with very little background around the $\rho(\omega)$ mass region.

Table 7-2 shows the number of events in the original data sample (with the cuts from Table 7-1) and the number of events left after each stage of the cuts.

To obtain the numbers for the ρ, $\omega \rightarrow \eta\gamma$ radiative decays we calculated

(i) the experimental acceptance, which after including all the cuts discussed above is;

$$0.0565 \pm 0.0004 \ (7\% \text{ error})$$

(ii) correction factors for the event losses due to different factors like gamma conversion in the spectrometer, gamma failure to convert in the lead glass, chamber inefficiencies, trigger losses, etc. . We will study these factors in the next chapter.

CHAPTER 8. INEFFICIENCY CORRECTIONS

Table 8-1 summarizes the inefficiency corrections for the apparatus and the reconstruction software for the 3 γ data. This section discusses these corrections.

1.0 GAMMA RAY CONVERSION UPSTREAM OF THE LEAD CONVERTER

The loss of events due to gamma rays converting inside the hydrogen target was included in the acceptance calculation. The loss due to conversion along their trajectories towards the converter was determined by calculating the amount of material traversed by the gammas. The effect is due mostly to the presence of the spectrometer chambers that contained aluminum and mylar sheets. From the known collision lengths in aluminum and mylar the probability of conversion of two gammas was calculated to be $(9.8 \pm 0.9)\%$ [1].

For three gamma events it is simply $(14.3 \pm 0.3)\%$.

2.0 EVENT REJECTION BY GAMMA HODOSCOPE

In Chapter 2 we saw that an event trigger was initiated if at least two "no-yes" combinations were found in the paired gamma hodoscope. A backscattered electron from the lead glass or a charged track near a gamma ray, seen by GHR, will cause a loss of a "no-yes" pair. This problem was investigated by a previous experiment [1] with a sample of 2500 ω^0 events taken with a weaker trigger requiring only one "no-yes" pair. The efficiency of this trigger was greater than 99%. With the trigger demanding two "no-yes" pairs the loss of a good 2γ event was experimentally found to be $(12.2 \pm 0.6)\%$. The loss of a 3γ event is much smaller since to reject a good 3γ event two of the three "no-yes" combinations should be lost. We calculate the loss of a 3γ event in the following way:

Let P be the probability of losing one "no-yes" combination. Then 2γ event will be rejected if one or both "no-yes" combinations were lost with probability;

$$P*(1-P) + P*(1-P) + P*P = 0.122 \quad \text{(measured)}$$

$$\therefore \quad 0.122 = 2P - P^2$$

$$\therefore \quad P = 0.063$$

To reject a good 3γ event any two of three or all three "no-yes" pairs have to be lost. The probability of this happening will be;

$$P*P*(1-P) + P*P*(1-P) + P*P*(1-P) + P*P*P$$

$$= 3P^2 - 2P^3 \Rightarrow 0.012$$

Thus the loss of a 3γ event due to the gamma hodoscope trigger requirement is $(1.2 \pm 0.1)\%$.

3.0 GAMMA SOFTWARE RECONSTRUCTION FAILURE

For 2 γ events 1000 events were handscanned on a CRT display by means of an interactive program that permited operator determination of gamma showers. The software reconstruction inefficiency for 2 γ events was found to be $(2\pm 2)\%$. For 3γ events it will be $(3 \pm 2.4)\%$.

4.0 DIGITIZATION SCALER RUNOUT

The possibility of losing a gamma shower due to an insufficient number of scalers in the experiments E420, E428 was studied using the 4γ data [3]. This was done by ploting spark positions for the Y-plane. A scaler runout would result in depletion of negative y-position. The y-position for 100,000 showers was found to be symmetric about the origin. Therefore the correction for digitization scaler runout for 4γ events was found to be negligible. For 3 γ events this correction should be even smaller.

5.0 GAMMA PARTIAL CHAMBER INEFFICIENCY

This is a time dependent correction and since largest fraction of our data had two gamma rays, the reconstruction program calculated the efficiency of each chamber and the single gamma efficiency for the 2 γ events at the end of each run, using the procedure described in Appendix C. The single gamma efficiency for all 2γ events was found to be 0.986 ± 0.002 .

For three gamma rays the efficiency is expected to be smaller since the same charge is distributed among more sparks. The single gamma efficiency for 3γ events was calculated [4] using a sample of

$$\pi^- P \to \omega\gamma\, n$$

events with the same method as described in Appendix C. The single gamma efficiency for these events was found to be 0.98 ± 0.02 . The net efficiency for the $\omega\gamma$ events is therefore 0.941 ± 0.04 . We use this number for the gamma chamber efficiency for our sample of $\eta\gamma$ events since these events have similar gamma energy spectra and same number of gamma rays as $\omega\gamma$ events.

6.0 CONVERSION EFFICIENCY OF LEAD CONVERTER

The gamma conversion efficiency for $\eta\gamma$ data sample is estimated the same way as it was estimated in Chapter 5 for the one gamma data. In this experiment the converter is 3.38 radiation lengths. Using this number we get an upper limit of 92.8% and a lower limit of 84.6% for the conversion efficiency of this detector. Averaging these values we get (88.7 ± 4.5)% conversion efficiency for one gamma ray. The conversion efficiency for 3γ is (0.698 ± 0.061).

7.0 BEAM CONTAMINATION

At 8.45 Gev/c, $(2.0 \pm 0.6)\%$ muon contamination was found in the beam, by measuring the amount of beam that traversed three feet of steel. Kaon contamination was estimated at 0.6% (published yield curves [57]) and electron contamination was estimated to be negligible.

8.0 CHARGED PION INTERACTION IN DETECTOR

Using the known cross sections of mylar, aluminum, etc. with pions, the probability of losing a pion is found to be $(2. \pm 1.)\%$ [3]. Thus, the probability of losing one or both pions is $(4.0 \pm 1.4)\%$.

9.0 CHARGED SPECTROMETER INEFFICIENCY

This is a time dependent correction which was handled by the reconstruction software (same way as the gamma rays). This factor was taken into account by the "offline" software in the calculation of the effective beam.

10.0 EVENT REJECTION BY TRIGGER

In this experiment the charged track part of the trigger demanded that two or three H2 scintillator elements be hit and the anti part of the trigger demanded that no TA element be set. To study the effects of these constraints, in a previous experiment, 20% of the data was collected using "loose" trigger requirements, demanding one or more H2 counters to be hit and allowing one TA to be set. The fraction of events lost due to different trigger requirements was found by tightening the trigger requirements with software. We used the numbers given in the study of the 4γ data of our experiment [3]. The loss caused by the H2 requirement was found to be (8.1 + 0.5)% , and the loss caused by the TA requirement was (15.6 + 0.14)% . The systematic error in the fraction of events lost due to TA requirement covers the t-dependent fluctuations of that correction.

The overall loss of events caused by the trigger requirements is

$$(24.4 \pm 1.4)\% .$$

11.0 OTHER CORRECTIONS

Losses due to scintilation counter inefficiencies (cracks, etc.) were calculated to be (3.2 ± 0.8)% by interactive scanning of 1000 events on a CRT.

As mentioned in Chapter 7, (10 ± 1)% of π^0's are lost in $\gamma_1\gamma_3$ and $\gamma_2\gamma_3$ combinations.

We ignore losses due to δ-ray creation inside the target, since there was a half-inch layer of polyethylen surrounding the target to stop low energy particles going into the detectors.

12.0 SUMMARY

The final overall correction factor for the 3γ data is calculated to be

$$\prod_i (1-C_i)$$

$$= 0.342 \pm 0.050 .$$

CHAPTER 9. EXPERIMENTAL RESULTS FOR THE WIDTHS $\Gamma[\rho\ \omega) \to \eta\gamma]$

In this chapter we will use the data sample from Fig.7-19 to calculate the widths $\Gamma(\rho \to \eta\gamma)$ and $\Gamma(\omega \to \eta\gamma)$.

1.0 THEORETICAL DISCUSSION.

The decays $\rho(\omega) \to \eta\gamma$ are M1 transitions. The quark model theory of M1 transitions is described in Appendix B. Appendix D has the calculation of the ratio R = $\Gamma_{\rho \to \eta\gamma}/\Gamma_{\omega \to \eta\gamma}$ using SU(6), and the Appendix E gives the differential cross section for the process $\pi^- p \to \eta\gamma n$ with $\eta\gamma$ invariant mass in the $\rho(\omega)$ mass range, with narrow resonance approximation.

From (B9) and (D2) the theoretical quark model predictions are

$$\frac{\Gamma_{\omega \to \eta\gamma}}{\Gamma_{\rho \to \eta\gamma}} = \left(\frac{\mu_{\eta\omega}}{\mu_{\eta\rho}}\right)^2 = \left(\frac{1}{3}\right)^2 \quad \text{and} \quad \frac{\mu_{\eta\omega}}{\mu_{\eta\rho}} > 0$$

Many different models [7]-[29] predict values for $\Gamma_{\omega \to \eta\gamma}$ between 0.17 Kev and 32 Kev and for $\Gamma_{\rho \to \eta\gamma}$ between 16.7 Kev and 138 Kev. Experimentally $\Gamma_{\rho \to \eta\gamma}$ and $\Gamma_{\omega \to \eta\gamma}$ have been measured from photoproduction of ρ and ω mesons [30], where two solutions were given;

$$\Gamma(\rho \rightarrow \eta\gamma) = 50 \pm 13 \text{ Kev}$$

and

$$\Gamma(\omega \rightarrow \eta\gamma) = 3.0^{+2.5}_{-1.8} \text{ Kev}$$

assuming the $(\omega, \rho) \rightarrow \eta\gamma$ relative decay phase is near zero; or

$$\Gamma(\rho \rightarrow \eta\gamma) = 76 \pm 15 \text{ Kev}$$

and

$$(\omega \rightarrow \eta\gamma) = 29 \pm 7 \text{ Kev}$$

assuming the decay phase is near 180°.

In photoproduction experiments it is very difficult to separate the $\omega \rightarrow \eta\gamma$ decays from the $\rho \rightarrow \eta\gamma$ decays since rho photoproduction dominates omega photoproduction by an order of magnitude and the t-dependence of the production cross section is the same.

In the reaction $\pi^- p \rightarrow \eta\gamma n$ total ρ production still dominates. However the t-dependence of the production cross section is different for rho ($\frac{d\sigma}{dt} \sim e^{-9.5t}$, $\pi + A$ exchange [53]) and omega ($\frac{d\sigma}{dt} \sim t{*}e^{-6.5t}$, $B + \rho$ exchange [1]) because of conservation of G-parity. Hence ω production exceeds ρ production for $|t| > 0.4$ $(Gev/c)^2$.

2.0 EXPERIMENTAL DETERMINATION OF $\Gamma(\rho\to\eta\gamma)$ AND $\Gamma(\omega\to\eta\gamma)$

In order to determine the values of $\Gamma_{\rho\to\eta\gamma}$, $\Gamma_{\omega\to\eta\gamma}$ and the sign of $\mu_{\eta\omega}/\mu_{\eta\rho}$, (E3) must be transformed to a form, where all quantities are experimentally measurable;

$$\frac{d^2\sigma}{dt\ dm} = A\cdot\Gamma_{\rho\to\eta\gamma}\left(\frac{d\sigma_\rho/dt}{|BW_\rho|^2} + R^2\frac{d\sigma_\omega/dt}{|BW_\omega|^2} + 2R\frac{d\sigma_{\rho-\omega}/dt}{|BW_\rho|^2|BW_\omega|^2}\times\right.$$

$$\left.\times(B\sin\phi_{\rho-\omega} + C\cos\phi_{\rho-\omega})\right) \qquad (1)$$

where $R = \mu_{\eta\omega}/\mu_{\eta\rho}$. A, B, C ~~are terms~~ depending on masses and width of ρ and ω and $\eta\gamma$ masses;

$$A = \frac{m}{\pi}\left(\frac{m_\rho(m^2-m_\eta^2)}{m(m_\rho^2-m_\eta^2)}\right)^3\cdot 2m$$

$$B = (m^2-m_\omega^2)m_\rho\Gamma_\rho\cdot\frac{m_\rho}{m}\left(\frac{m^2-4m_\pi^2}{m_\rho^2-4m_\pi^2}\right)^{3/2} + (m^2-m_\rho^2)\cdot m\Gamma_\omega \qquad (2)$$

$$C = (m^2-m_\omega^2)(m^2-m_\rho^2) - m\Gamma_\omega\cdot m_\rho\Gamma_\rho\cdot\frac{m_\rho}{m}\left(\frac{m^2-4m_\pi^2}{m^2-4m_\pi^2}\right)^{3/2}$$

$d\sigma_{\rho-\omega}/dt$ and $\phi_{\rho-\omega}$ are $\rho-\omega$ interference cross section and production phase respectively calculated from ref.[53], where these values were measured in $\rho-\omega$ interference experiments by comparing the cross sections for the reactions $\pi^- p \to \pi^+\pi^- n$ and $\pi^+ n \to \pi^+\pi^- p$ for beam momenta of 3, 4 and 6 Gev/c.

Within experimental errors, from reference [53] and [54], the interference cross section is;

$$\frac{d\sigma_{\rho-\omega}}{dt} = \sqrt{\frac{d\sigma_\rho}{dt}\cdot\frac{d\sigma_\omega}{dt}}$$

and the phase is close to $-\pi/2$ and does not vary, within statistics, with beam energy. This is good enough for the accuracy we need.

The $d\sigma_\rho/dt$ was extrapolated to 8.45 Gev/c beam momentum ($\sigma_\rho^{tot} \sim P_{Lab}^{-2.25}$ [54]) from the values given in ref [53] and $d\sigma_\omega/dt$ was extrapolated from beam momentum 6 Gev/c to 8.45 Gev/c ($\sigma_\omega^{tot} \sim P_{Lab}^{-2.38}$) from ref [1]. Since our experimental mass resolution is larger than ω width, to be able to fit the form (1) to experimental mass distribution, we smear (1) using a gaussian as a resolution function in the following way;

$$\left(\frac{d\sigma(m)}{dm\ dt}\right)_{exp} = \int \left(\frac{d\sigma(m')}{dmdt}\right)_{theor} \cdot R(m-m')dm' \tag{3}$$

where

$$R(m - m') = \frac{1}{\sqrt{2\pi}\sigma} e^{-(m-m')^2/2\sigma^2}$$

As integration limits we take $\pm 3\sigma$, where σ is our experimental resolution.

Since we know that at small transverse momenta ($|t'|$) most of the events in our sample come from $\rho \rightarrow \eta\gamma$ decay and for larger $|t'|$ most of the events come from $\omega \rightarrow \eta\gamma$ decay we separated the data sample into two $|t'|$ bins

$0 < |t'| < 0.2\ (Gev/c)^2$ and $0.2 < |t'| < \infty\ (Gev/c)^2$

and fitted all the data and those in the two $|t'|$ bins simultaneously to the integrals of the function (3) over corresponding $|t'|$ ranges. We left the fraction of differential cross sections for ρ or ω production in different $|t'|$ bins as free parameters in the fit and since we know the value of these fractions theoretically we used the results as one of the measures of reliability of the fits. Statistical limitations of our final data sample forced us to conclude that a fit of the functions (3) and a polynomial background to the data $\eta\gamma$ spectra for different $|t'|$ bins simultaneously was not very reliable and many solutions for the parameters were possible. We fixed the polynomials in these solutions and used the other parameters as starting values in an event by event maximum likelihood fit. We used the obtained parameters in a χ^2 fit with free polynomials again and iterated this process until the fits agreed for both procedures. These procedures converged for two different sets of parameters. Using the values of these parameters, the acceptances and the experimental correction factor of Table B-1 the widths $\Gamma_{\rho\to\eta\gamma}$, $\Gamma_{\omega\to\eta\gamma}$ and the ratio R = $\mu_{\eta\omega} / \mu_{\eta\rho}$ were calculated to be;

$$(i) \quad \left\{ \begin{array}{ll} \Gamma_{\rho \to \eta\gamma} = 50.73 \pm 15.80 \text{ Kev} & (31.1\% \text{ error}) \\ \Gamma_{\omega \to \eta\gamma} = 14.63 \pm 8.25 \text{ Kev} & (56.4\% \text{ error}) \\ R = 0.537 \pm 0.126 & (23.5\% \text{ error}) \end{array} \right.$$

or

$$\text{(ii)} \begin{cases} \Gamma_{\rho \to \eta\gamma} = 24.73 \pm 7.89 \text{ Kev} & (31.9\% \text{ error}) \\ \Gamma_{\omega \to \eta\gamma} = 10.74 \pm 6.49 \text{ Kev} & (60.4\% \text{ error}) \\ R = -0.695 \pm 0.169 & (25.6\% \text{ error}) \end{cases}$$

The χ^2 per degree of freedom in both solutions is less than 1. In both solutions the fractions for ρ and ω production differential cross sections were close to each other and to theoretical cross sections, and also the experimental resolution for our $\eta\gamma$ data mass spectrum (M_{mes}) was found to be;

$$\sigma_R = 49. \pm 8.$$

The major part of the errors in our calculations of the decay rate are due to correlations which are partly reflected in bad $\eta\gamma$ mass resolution. If these correlations were artificially set to zero, then the final error is due to our statistics only - this amounted to about 15%.

The fits for the $M_{\eta\gamma}$ spectrum for all the data (all $|t'|$'s) and for the large $|t'|$ bin give a slightly smaller χ^2 value for the solution (i), than for the solution (ii), but for the small $|t'|$'s the fit to the spectrum has a smaller χ^2 value for the solution (ii). Since the spectrum with all the data has approximately twice the statistics of the spectra for the $|t'|$ bins, the solution (i) seems to be preferable. The solution (i) within errors agrees with most of the theoretical predictions from ref [7]-[29], and also agrees with SU(6). Solution (i) also agrees with one of the two solutions from a previous experiment [30].

However there are some models (ref.[22,27]) in which the sign of R is not discussed and within errors both of the solutions could agree with these models.

CHAPTER 10. CONCLUSIONS

In our study of radiative decays of nonstrange mesons we obtained the following results:

1. We set a new upper limit for the branching ratio of the decay $\omega \to \pi^+\pi^-\gamma$ which is almost an order of magnitide smaller than the present value in the Particle Data Book (Br $\omega \longrightarrow \pi^+\pi^-\gamma < 5\%$).

This result cannot be compared with present theoretical predictions [48,49,50] since all the models use as input parameter the decay rate $\rho \to \pi\gamma$ for which there is no reliable experimental measurement. If, however, the most recent measurement of the decay rate $\rho \to \pi\gamma$ [51] is used in models of references [49], [50], our upper limit for the branching ratio of the decay $\omega \to \pi^+\pi^-\gamma$ falls within the range predicted in these models. This could be an indication that the recent value of the decay rate $\rho \to \pi\gamma$ [51] is a reliable measurement. As an aside, it should be noted that in almost every theoretical model [7-29] the prediction for this branching ratio $\rho \to \pi\gamma$ was considerably different (by about a factor of two) from previous experimental measurements (see Particle Data Book value). The recent measurement of this decay rate is, of cource, considerably closer to these theoretical predictions.

2. We obtained an independent high statistics measurement for the branching ratio Br($\eta' \rightarrow \rho\gamma$), which is in excellent agreement with more recent measurements [38-42] of this branching ratio.

3. We observed the the radiative decays $\rho\ (\omega) \rightarrow \eta\gamma$ in the reaction

$$\pi^- p \longrightarrow \rho\ (\omega)n$$
$$\hookrightarrow \eta\gamma$$

for the first time, and measured their rates. Because of our poor statistics the fits to the $\eta\gamma$ mass spectrum converged for two different sets of decay rates. One of these solutions is very close to most of the SU(6) predictions, and to one of the model dependent solutions obtained in a $\rho\ (\omega)$ photoproduction experiment [30].

This result can be improved upon by a future high statistics experiment, observing the reaction $\pi^- p \rightarrow \rho\ (\omega)n$ that has a high resolution gamma ray detector. In this connection it should be remarked that our earlier experimental apparatus (before the addition of extra lead) could, in principle, collect enough statistics of $\rho\ (\omega) \rightarrow \eta\gamma$ events in a long run, to obtain a meaningful selection between the two solutions presented in this thesis. This is so besause the addition of more lead worsened the gamma energy resolution. The greater statistics, hence the smaller statistical errors, gained by higher conversion probability, were overpowered by the errors due to correlations as reflected in, say, the bad $\eta\gamma$ mass resolution. The trigger in an experiment of this sort should demand events with three possible gamma rays and two charged pions after the magnet. We conclude by stating that if such an experiment leads to unique solution to the $\rho \to \eta\gamma$ and $\omega \to \eta\gamma$, that confirms our first solution, and if the decay rate for $\rho \to \pi\gamma$ obtained by S.M. Flatte et al [51] is also confirmed by another experiment, then it will be possible to state that all the radiative decays of light quarks u and d agree - within (10-15%) - with the quark model as suggested by N. Isgur [7], to mention one among many of the theoretical workers in the field (see ref [8,9,10,16,24,28]).

APPENDIX A. THE MONTE-CARLO SIMULATION OF THE DATA

To be able to calculate the branching ratios of different radiative decays the number of such detected events have to be corrected for losses due to the cuts and constraints of Table 5-1, and the additional cuts discussed in Chapter 5.

Monte-Carlo simulation programs were written to calculate these corrections for different radiative decays that were possible candidates in the sample of data with $\pi^+\pi^-$ and a gamma ray detected. Monte-Carlo simulation programs were written also for the possible background interactions where $\pi^+\pi^-$ and two gamma rays were produced but only one gamma was detected. These programs helped to understand and separate such events from true radiative decay events.

All the Monte-Carlo simulation programs used as input masses generated for the produced meson M_{mes} (η, ω, η') and its decay product $M_{\pi^+\pi^-}$ (ρ^0 or phase space).

Since η, ω and η' mesons have narrow widths their masses were generated in the simple Breit-Wigner form;

$$\Phi(m) \sim \frac{\Gamma_0}{(m^2-m_0^2)^2 + m_0^2\Gamma_0^2} \qquad (A1)$$

Then the decay of the particle with the mass M_{mes};

$$M_{mes} \dashrightarrow M_{\pi^+\pi^-} + M_3 \qquad \text{(A2)}$$

was simulated, where M_3 was either equal to zero for the $\pi^+\pi^-\gamma$ decay of the meson, or equal to the neutral pion mass for the $\pi^+\pi^-\pi^0$ decay of the meson. The $M_{\pi^+\pi^-}$ was generated with phase space distribution if π^+ and π^- were in S-state; if π^+ and π^- were in P-state, the $M_{\pi^+\pi^-}$ was generated as a ρ^0 meson with a P-wave Breit-Wigner form;

$$\Phi(m) \sim \frac{\Gamma(m)}{(m^2-m_0^2)^2 + m_0^2\Gamma^2(m)} \qquad \text{(A3)}$$

where in the case of $\rho^0 \dashrightarrow \pi^+\pi^-$ $(1^- \dashrightarrow 0^- 0^-)$ decay the width $\Gamma(m)$ has the following dependence on mass [58];

$$\Gamma(m) = \Gamma_0 \left(\frac{q}{q_0}\right)^3 \frac{m_0}{m} \qquad \text{(A4)}$$

where q is the momentum of a pion in the ρ^0 center of mass system.

The generated $\pi^+\pi^-$ invariant mass $M_{\pi^+\pi^-}$ was then weighed by the product of the decay matrix element [59,60] (shown in Table A-1 for different decays) and the phase space weight:

PS=phase space weight $\sim$ p*q

(where p is the momenum of the gamma or π^0 (corresponding to M_3 in (A2)), in the decaying meson center of mass system and q is the pion momentum in the $\pi^+\pi^-$ center of mass system). In table A1 the same p,q notation for the momenta is used.

The Monte-Carlo simulation programs for the radiative $\pi^+\pi^-\gamma$ decay of the mesons consist of three sections;

1. Generation of 4-vectors

2. Geometric, kinematic and trigger constraints of the experiment (Table 5-1)

3. Charged pion decay in flight and charged pion and gamma ray interactions in the target.

The Monte-Carlo simulation programs for the $\pi^+\pi^-\pi^0$ decay used the same sections as the radiative decay Monte-Carlo programs, but in a different sequence. After section (1) for generating 4-vectors, section (3) of the radiative decay Monte-Carlo program was called. If the charged particles did not decay in flight or interact in target and only one gamma ray interacted in the target, section (2) was called and if all the constraints of this section were satisfied the event was kept as a good background event. If no gamma rays interacted in target, section (2) was called requiring the constraints to satisfy only for the charged pions, and one of the gamma rays from the $\pi^0 \to \gamma\gamma$ decay. If both gamma rays survived the constraint cuts of section (2), an additional section (4) to simulate "loss" of a gamma ray was called. Then the section (2) constraints were applied on the surviving gamma ray.

We now proceed to describe the sections (1),(2),(3) and the section to simulate "loss" of a gamma ray in more detail.

(1) Generation of the 4-vectors

In all different reactions studied the events were described by the following kinematic quantities: the beam momentum, the four momentum transfer squared (t) and the masses M_{mes} and $M_{\pi^+\pi^-}$.

To generate the 4-vector we have used some of the routines (INITL, RY, GO, ORDR, RAZ) of the bubble chamber program SAGE [61] by J.Friedman. We modified the routine GO, where the simulation of the kinematics of the reaction is done, in order to generate 4-vectors using different $d\sigma/dt$

distributions for different $|t'| = |t - t_{min}|$ ranges, and to generate 4-vectors in a certain $|t'|$ bin. Before these modifications the routine GO generated events in all $|t|$ range, with one given $d\sigma/dt$ distribution.

Our experimental acceptance is t-dependent (becomes very small at large $|t'|$). This t-dependent simulation with experimental $d\sigma/dt$ distributions will decrease the errors of the acceptances determined for different interactions. Also we were able to increase the speed of the 4-vector generation part of the Monte-Carlo simulation programs, by generating events in a limited $|t'|$ range ($|t'| < 1.5$ (Gev/c)^2).

For different reactions there were different main programs, calling the same routines, for simulating the 4-vectors, using as input the nesessary $d\sigma/dt$ and decay angular distributions for that interaction.

The radiative decay Monte-Carlo simulation program produced events of the form:

$$\pi^- p \to P_{meson} + n$$
$$\qquad \hookrightarrow P_{\pi^+\pi^-} + \gamma$$
$$\qquad\qquad \hookrightarrow \pi^+\pi^-$$

The background Monte-Carlo simulation programs produced events of the form

$$\pi^- p \dashrightarrow P_{meson} + n$$
$$\quad\quad \hookrightarrow P_{\pi^+\pi^-} + \pi^0$$
$$\quad\quad\quad \hookrightarrow \pi^+\pi^- \quad \hookrightarrow \gamma\gamma$$

For each decay step the pair of routines RY and GO were called, which used as input;

a) The mass and the 4-vectors of the decaying particle (or the center of mass system of the decayed particles).

b) The $d\sigma/dt$ distribution of the system (π^- p) or cosine of the decay angle generated according to the theoretical angular distributions, shown in the Table A-1, where the angle θ is the angle ($\vec{p} * \hat{q}$). For each decay step the routine RY uses the corresponding independent variables (4-vectors, the mass and the direction of the decay product) to initialize the generation of the 4-vectors by the routine GO.

(2) The geometric, kinematic and trigger constraints.

After generating the 4-vectors of an event the point of interaction in the target was generated. This target point distribution was taken to be randomly distributed in the forward direction with uniform distribution in the area and with a 1/R distribution in the radial direction. Then the positions of each particle at different planes were calculated, which were required to satisfy the geometric constrains of Table 5-1.

The 4-vectors were also required to satisfy the kinematic cuts of the Table 5-1 and the additional cuts of discussed in Chapter 5. Then the trigger constraint demanding only one H2 hodoscope element to be set for each charged particle was checked.

(3) Charged pion decay in flight, charged pion and gamma ray interaction in hydrogen target

1. The probability of a charged pion decay in flight is:

$$\frac{\text{(distance in inches from target to last chamber)}}{\beta*(307.2)}$$

where $\beta = v/c$ is the velocity of the charged pion.

2. The probability of π^+, π^- interaction in target is:

(path length hydrogen target in inches)*0.00325,

assuming an interaction cross section of 30 mb.

3. The probability of conversion of a gamma ray is:

(path length in hydrogen in inches)*0.00198,

assuming a scaling of the thickness by 0.69 radiation length.

Events were rejected statistically using the above probabilities to account for event losses due to these reasons.

(4) Simulation of "loss" of a gamma ray in 3π events

In 3π Monte-Carlo programs events were rejected if:

1. A charged pion did not satisfy the requirements of sections (2) and (3).

2. Both gamma rays satisfied the sections (2) and (3), both gammas converted in the lead converter and were not too close to be seen as one (their distance was more than lead

glass array cell width of 7.5 inches).

If only one gamma ray did not satisfy the geometric constraints, or got converted in the target, or failed to convert in the lead converter but was farther than 7.5 inches from the other gamma ray, the event was treated like a radiative decay event, after adding the energy of the undetected gamma ray to the neutron energy to have energy conservation in the reaction.

If both gamma rays satisfied the geometric cuts and both did not convert in the target, they could sometimes be detected as one if:

(i) The two gamma rays converted less than 7.5 inches apart in the lead converter. All the π^0 energy was deposited in one lead glass block and had to be treated as a high energy gamma ray.

(ii) The gamma rays were less than 7.5 inches apart but only one of them converted.

Such data events got a gamma energy correction assuming that there was one high energy gamma, instead of two lower energy gammas. Hence the energy that escaped the lead glass would normally be calculated incorrectly. We remedied this as follows.

We fit Monte-Carlo $M_{\pi^+\pi^-\gamma}$ peak to data $M_{\pi^+\pi^-\gamma}$ peak, in η and ω regions using energy dependent functions;

$$F_e = a_e - b_e * \ln(E_e)$$

$$F_\gamma = a_\gamma - b_\gamma * \ln(E_\gamma)$$

for fractions of energy deposited by each gamma ray with a_γ, b_γ, a_e and b_e as parameters. F_e is used if the gamma ray got converted with $E_e = E_\gamma/2$ approximately. F_γ is used if the gamma ray did not convert. The starting values for a_e, b_e, a_γ, b_γ are calculated from references [62,56] and they are changed to get good fits for $\pi\pi\gamma$ mass spectrum. We obtained stable values for a_e, b_e, a_γ, b_γ at minimum χ^2/degree of freedom = 1.12, with a 2-3% change for 2-3% parameter changes.

Fig 6-1, 6-2 and 6-3 show the good agreement of Monte-Carlo $M_{\pi^+\pi^-\gamma}$, E_γ and $M_{\pi^+\pi^-}$ spectra with the data.

APPENDIX B. M1 RADIATIVE DECAYS IN QUARK MODEL

The electromagnetic transitions between two particles ($a \to b + \gamma$) corresponding to $\Delta j = 0, +1$ and no parity change can occur via l=1 magnetic (M1) photon emission. The hamiltonian for these transitions is:

$$H_{int} = -\hat{\mu} * \hat{B} \tag{B-1}$$

where $\hat{B}$ is the vacuum electromagnetic field operator and $\hat{\mu}$ is the magnetic dipole operator.

In the simple quark model the quark constituents of the particles a and b are in relative S state. Thus the magnetic moment operator corresponding to a given particle will be [63]:

$$\hat{\mu} = \sum_i \hat{\mu}_i = \mu_q \sum_i \frac{e_i}{e} \hat{\sigma}_i \tag{B-2}$$

where e_i, $\hat{\sigma}_i$ and μ_q are the charge, the spin operator, and the magnetic moment for the i-th quark respectively.

The interaction hamiltonian of the i-th quark and a photon with polarization ε_γ and momentum k will be [64]:

$$H_i = \mu_q \frac{e_i}{e} \hat{\sigma}_i (\hat{k}\times\hat{\varepsilon}_\gamma) e^{i\hat{k}\hat{r}_i} \qquad \text{(B-3)}$$

The decay rate (a --> b+γ) is determined by the matrix element [64];

$$D_{ba} = \langle\psi (b)|\sum H_i|\psi (a)\rangle \qquad \text{(B-4)}$$

and the matrix elements of the magnetic moment between the particles a and b [63];

$$\mu_{ba} = \langle \psi (b)|\sum \hat{\mu}_i|\psi (a)\rangle \qquad \text{(B-5)}$$

where ψ (a) and ψ(b) are wave functions of the particles a and b expressed by the wave functions of their quark constituents.

The decays of the vector mesons into a pseudoscalar meson and a photon (V --> P+γ) or pseudoscalar mesons into a vector meson and a photon (P --> V+γ) occur via M1 photon emission since the parities and spinsof vector and pseudoscalar mesons are;

$$\pi_V = -1 , \qquad j_V = 1 \qquad \text{(B-6)}$$

$$\pi_P = -1 , \qquad j_P = 0$$

respectively.

The decay rates $\Gamma(V\to P+\gamma)$ [or $\Gamma(P\to V+\gamma)$] are obtained by multiplying the squares $|D_{PV}|^2$ (or $|D_{VP}|^2$) of the matrix elements for the transitions V --> P+γ (or P --> V+ γ), summed over the polarization states of the final photon and averaged over the spin direction of the vector meson by [65]:

$$(2\cdot\pi\rho\cdot f/2k)*N \tag{B-7}$$

Here $2\pi\rho\cdot f$ is the phase space factor, which in its relativistic form is [65]:

$$2\cdot\pi\rho\cdot f = 2\pi\frac{4\pi}{(2\pi)^3}k^2\frac{\omega_k}{M_V} = \frac{k^2}{\pi}\frac{\omega_k}{M_V} \tag{B-8}$$

where k is the energy of the photon, ω_k is the energy of the pseudoscalar meson and M_V is the mass of the vector meson. In (B-7) 1/2k is the photon normalization factor, and the factor $N = M_o/\omega_k$ is used to relate the relativistic decay amplitude with the nonrelativistic case which does not have the term ω_k/M from (B-8). Thus the rate for M1 transitions is given by [6];

$$\Gamma(V\to P\gamma) = \frac{1}{2\pi}k|D_{PV}|^2 \quad \text{or} \quad \Gamma(P\to V\gamma) = \frac{3}{2\pi}k|D_{VP}|^2$$

$$\Gamma(V \to P\gamma) = \frac{1}{3\pi}k^3\mu_{PV}^2 \qquad \text{or} \qquad \Gamma(P \to V\gamma) = \frac{1}{\pi}k^3\mu_{VP}^2 \tag{B-9}$$

where μ_{PV} is the magnetic dipole transition moment as in (B-5) and k is the energy of the photon.

$$k = (M_V^2 - M_P^2)/2M_V, \text{ for } V \dashrightarrow P+\gamma$$

and

$$k = (M_P^2 - M_V^2)/2M_P, \text{ for } P \dashrightarrow V+\gamma$$

APPENDIX C. GAMMA SHOWER CHAMBER EFFICIENCY CALCULATION

In the gamma detection system there were two views - plane X and elevation Y - with three planes each. We label the three X planes 1, 2, 3 and the three Y planes 4, 5, 6. A shower was accepted if one view had at least two planes firing, and the other view had at least one plane firing.

We define

$$\varepsilon_i = \text{Efficiency of Chamber Plane } i$$

$$= \frac{\text{\# of times the plane contained a spark}}{\text{\# of tracks through the chamber}}$$

and

$$P_i = \text{Participation Ratio of Plane } i \text{ for a Found Event}$$

$$= \frac{\text{\# of times the plane fired in a found event}}{\text{\# of found events}}$$

The probability $P(\geq 2)$ of at least two of the three planes in one view firing is given by:

$$P(\geq 2) = \varepsilon_i \varepsilon_j (1-\varepsilon_k) + \varepsilon_i (1-\varepsilon_j) \varepsilon_k + (1-\varepsilon_i) \varepsilon_j \varepsilon_k + \varepsilon_i \varepsilon_j \varepsilon_k$$

$$= \varepsilon_i\varepsilon_j + \varepsilon_i\varepsilon_k + \varepsilon_j\varepsilon_k - 2\,\varepsilon_i\varepsilon_j\varepsilon_k \qquad \text{(C-1)}$$

where $(i,j,k) = (1,2,3)$ or $(4,5,6)$

Therefore, the probability P_γ of finding a shower when one is present, can be easily written:

$$P_\gamma = P_x(>2)*P_y(>2)+P_x(>2)*(\varepsilon_4(1-\varepsilon_5)(1-\varepsilon_6)+\varepsilon_5(1-\varepsilon_4)(1-\varepsilon_6))$$

$$+ P_y(>2)*(\varepsilon_1(1-\varepsilon_2)(1-\varepsilon_3)+\varepsilon_2(1-\varepsilon_1)(1-\varepsilon_3)) \qquad \text{(C-2)}$$

Next, we can write expressions for the participation ratios using the definition for P and the expressions (C-1) and (C-2). For

$$P_1/\varepsilon_1 = [P_y(>2)+(\varepsilon_2+\varepsilon_3-\varepsilon_2\varepsilon_3)*(\varepsilon_4(1-\varepsilon_5)(1-\varepsilon_6)$$

$$+\varepsilon_5(1-\varepsilon_4)(1-\varepsilon_6))]/P_\gamma \qquad \text{(C-3)}$$

$$P_2/\varepsilon_2 = [P_y(>2)+(\varepsilon_1+\varepsilon_3-\varepsilon_1\varepsilon_3)*(\varepsilon_4(1-\varepsilon_5)(1-\varepsilon_6)$$

$$+\varepsilon_5(1-\varepsilon_4)(1-\varepsilon_6))]/P_\gamma \qquad \text{(C-4)}$$

$$P_3/\varepsilon_3 = [P_y(>2)*(\varepsilon_1+\varepsilon_2-\varepsilon_1\varepsilon_2)]/P_\gamma \qquad \text{(C-5)}$$

Identical expressions hold for the planes of the second view under the exchange (1,2,3) <--> (4,5,6).

To calculate the single shower efficiency P_γ we needed the efficiencies ε_i, given the P_i from the recorded data. This was done by solving for ε_i in (C-2) to (C-5) using an iterative procedure. The starting values for ε_i on the RHS of (C-3,4,5) were taken as the P_i. A new set of ε_i were then found and the process was repeated until stable results were reached, usually after only a few iterations. The single shower efficiency was obtained by substituting these final chamber efficiencies into (C-2), and the double and triple shower efficiencies were easily deduced thereafter.

APPENDIX D. ρ (ω) --> $\eta\gamma$ DECAYS

In the standard 3 quark model the wave functions (ψ) for the particles ρ^0, ω and η are [65];

$$\psi(\rho) = (1/\sqrt{2})(a_1\bar{a}_1 - a_2\bar{a}_2)*f(r)$$

$$\psi(\omega) = (2+\lambda_\omega^2)^{-1/2}(a_1\bar{a}_1 + a_2\bar{a}_2 - \lambda_\omega a_3\bar{a}_3)*f(r) \qquad \text{(D-1)}$$

$$\psi(\eta) = [2(2+\lambda_\eta^2)]^{-1/2}[(a_1\bar{b}_1 - \bar{a}_1 b_1) + (a_2\bar{b}_2 - a_2\bar{b}_2) - \lambda_\eta(a_3\bar{b}_3 - \bar{a}_3 b_3)]*f(r)$$

where a_i, b_i are the spin functions (with spin up and spin down respectively) for a quark (i=1,2,3) and $\bar{a}_i$, $\bar{b}_i$ are the corresponding spin functions for an antiquark. The values of the parameters λ_ω and λ_η are model dependent. According to the conventional $\phi-\omega$ mixing problem, where ω consists of only nonstrange quarks $\lambda_\omega = 0$, and if η is the pure pseudoscalar octet meson ($\eta-\eta'$ mixing angle $\theta_P = 0$) $\lambda_\eta = 2$.

Using (B-4) and (D-1) the squares of the matrix elements for the transitions ρ (ω) --> $\eta\gamma$ will be [65];

$$|D_{\omega\eta}|^2 = \mu_p^2 \, k^2 \, \frac{8}{27} \frac{1}{2+\lambda_\omega^2} \frac{1}{(2+\lambda_\eta)^2} (1-\lambda_\eta\lambda_\omega)^2$$

$$|D_{\rho\eta}|^2 = \mu_p^2 k^2 \frac{4}{3} \frac{1}{(2+\lambda_\eta)^2} \qquad (D-2)$$

where μ_p is the proton magnetic moment and k is the quark momentum.

Here we used $\mu_q = \mu_p$ which is easy to check by using (B-5) to calculate proton's static magnetic moment, given by the diagonal matrix elements of the third component of $\hat{\mu}$. Also in (D-2), following SU(6), ρ, ω have been assumed in pure $^3S_1$ state, and the space part of the wave function f(r) has been assumed to be the same for vector and pseudoscalar mesons.

By substituting (D-2) in (B-9) we can get the $\overline{\Gamma(\rho(\omega)}$ --> $\eta\gamma)$ decay rates as a function of parameters λ_ω and λ_η.

It is easy to notice that when λ_ω = 0 (no strange quarks in ω) the ratio;

$$R^2 = \frac{\Gamma(\omega\to\eta\gamma)}{\Gamma(\rho\to\eta\gamma)} = \left(\frac{1}{3}\right)^2 \qquad (D-3)$$

and is independent of the value of the parameter λ_η (measure of $\eta-\eta'$ mixing).

APPENDIX E. THE REACTIONS $\pi^- p \to \rho(\omega)n$

In the study of the reaction $\pi^- p \to V n$ ($V \to \eta\gamma$) we will use the narrow resonance approximation. When V is the ω meson we can do this, because ω has narrow width. The reason why this can be done for the ρ meson as well is given in ref.[6].

For the ρ meson the only isospin invariant coupling to two pions has the form $\varepsilon_{ijk}\rho^{\mu}\pi_i\rho_{\mu}\pi_k$ so the terms proportional to $p^{\mu}p^{\nu}$ in the ρ meson propagator do not have any effect. This means that for the two pion decay of the virtual ρ it is possible to make the replacement $p^{\mu}p^{\nu}/m_{\rho}^2 \to p^{\mu}p^{\nu}/m^2$ in the ρ propagator.

The differential cross section for the reaction $\pi^- p \to V n$ ($V \to \eta\gamma$) in the narrow resonance approximation is [6];

$$\frac{d^2\sigma}{dt\,dm^2} = \left(\frac{m\Gamma_{V\to\eta\gamma}(m^2)}{\pi|BW_V(m^2)|^2}\right)\frac{d\sigma}{dt}\left(\pi^- p \to V(m^2)n\right) \qquad \text{(E-1)}$$

where for the ρ meson $BW_{\rho}(m^2)$ is the relativistic P-wave Breit-Wigner amplitude:

$$BW_\rho(m^2) = m^2 - m_\rho^2 + i m_\rho \Gamma_\rho \left(\frac{m_\rho}{m}\right) \left(\frac{m - 4m_\pi^2}{m - 4m_\pi^2}\right)^{3/2}$$

and for the ω meson $BW_\omega(m^2)$ is:

$$BW_\omega(m^2) = m^2 - m_\omega^2 + i m_\omega \Gamma_\omega$$

where the mass dependence of Γ_ω was ignored because of the narrow width of omega meson.

Assuming that the amplitude for the process $\pi^- p \to Vn$ does not depend on m^2 very much in the mass range of interest, the differential cross section for this process can be written in this form [6];

$$\frac{d\sigma}{dt}\left(\pi^- p \to V + n\right) = \sum_{\lambda_\nu, \lambda_n, \lambda_p} \left|P'(\lambda_\nu, \lambda_n, \lambda_p)\right|^2 \qquad \text{(E-2)}$$

and with the narrow resonance approximation the differential cross section for the overall process $\pi^- p \to \eta\gamma\, n$ with $\eta\gamma$ invariant mass in the ρ, ω mass range is [6];

$$\frac{d^2\sigma}{dt\,dm^2} = \frac{m\Gamma_{\rho\to\eta\gamma}}{\pi} \left(\frac{m_\rho (m^2 - m_\eta^2)}{m(m_\rho^2 - m_\eta^2)}\right)^3 \times \qquad \text{(E-3)}$$

$$\times \sum_{\lambda_\nu, \lambda_n, \lambda_p} \left| \frac{P'_\rho(\lambda_\nu, \lambda_n, \lambda_p)}{BW_\rho(m^2)} + \frac{\mu_{\eta\omega}}{\mu_{\eta\rho}} \frac{P'(\lambda_\nu, \lambda_n, \lambda_p)}{BW_\omega(m^2)} \right|^2$$

APPENDIX F. TABLE OF THE CALCULATED VALUES OF THE DECAY RATES

$\Gamma_{\rho\to\eta\gamma}$, $\Gamma_{\omega\to\eta\gamma}$, $\Gamma_{\rho\to\pi\gamma}$ and $\Gamma_{\eta'\to\rho\gamma}$

TABLE F-1

REFERENCE	$\Gamma_{\rho\to\eta\gamma}$	$\Gamma_{\omega\to\eta\gamma}$	$\Gamma_{\rho\to\pi\gamma}$	$\Gamma_{\eta'\to\rho\gamma}$
7. N.Isgur (76)	46	4.9	75	95
9. F.Gilman,I.Karlinger (74)	57	7	94	120
10. R.Torgerson (74)	56	6.2	94	92
11. D.Boal,R.Graham,J.Moffat(76)	84,82 26	12,10 24	85,93 35	89,62 130
12. P.Hays,M.Ulehla (75)	37.4	5.4	–	–
13. P.O'Donnell (76)	40	6	64	77
14. Etim-Etim,M.Greco (77)	55	7.3	93	118
15. A.Bohm,R.Tesse (77)	3.9,4.8 5.0	.18,.22 .23	35	–
16. R.Thews (76)	12,14.5 47	–, – 4.7	35	250,31 98
17. E.Takasugi (76)	138	12	–	–
18. T.Barnes (76)	45,15	5.9,1.9	91,88	38,10
19. G.Gounaris (76)	55.4,55 55.5	9.6,8.1 4.2	90,73 73	106,68 85
20. L.Broun,P.Singer (77)	16.7	.17	77	21
21. B.Edwards,A.Kamal (76)	76.5,127 24	6.8,11.4 1.9	80,107 28	112,135 43.8
22. G.Grunberg,F.Renard (76)	56,26.8	5,13.01	90, –	88.5, –
23. N.Chase,M.Vaughn (76)	37.3 (32.4)	4.8 (4.17)	82.6	109.9

continued...

TABLE F-1 (continued)

REFERENCE	$\Gamma_{\rho\to\eta\gamma}$	$\Gamma_{\omega\to\eta\gamma}$	$\Gamma_{\rho\to\pi\gamma}$	$\Gamma_{\eta'\to\rho\gamma}$
24. B.Edwards, A.Kamal (77)	53, 42 30, 45	10, 32 28, 3.4	81, 49 87, 86	160, 120 4.5, 150
25. C.Albright, R.Oakes (77)	20	2.53	94.3	79.6, 53.4 35.3
26. L.Maharana, P.Misra (78)	16.9	.85	36.6	45.5
27. L.Urruita (78)	39, 30.8	3.6, 4.3	98.4, 82.3	152, 168
28. B.Edwards, A.Kamal (79)	55, 26	7.2, 24	92, 35	120, 130
29. Riazuddin, Fayyazuddin (79)	59	7.3	92	111
EXPERIMENT	50 ± 13 76 ± 15	$3^{+2.5}_{-1.8}$ 29 ± 7	35 ± 10 (67 ± 7)*	89 ± 27

*) recent experiment by Berg et al., PRL 44, 706 (80).

REFERENCES

1. M.S. Shaevitz "A high statistics study of ω production at 6.0 Gev/c", Ph.D. Thesis, Ohio State University (1975).
2. J.A. Dankowych "A Partial Wave Analysis of the reaction $\pi^- p \rightarrow \pi^+\pi^-\pi^0 n$ at 8.45 Gev/c", Ph.D. Thesis, University of Toronto (1980).
3. P.J. Brockman "B^0 (1235) production in the reaction $\pi^- p \rightarrow \omega\pi^0 n$ at 8.45 Gev/c", Ph.D. Thesis, McGill University (1981).
4. C.J. Zanfino "Experimental investigation of the radiative decay $\eta' \rightarrow \omega\gamma$", M.Sc. Thesis, McGill University (1976).
5. B.Gobby et al., PRL 33, 1450 (74).
   A.Brownman et al., PRL 32, 1067 (74).
6. Chi-Kwong Kung & Nathan Isgur, Can.J.Phys. 55, 1716 (77).
7. N.Isgur, PRL 36, 1262 (76).
8. B.G.Kenny, PR D7, 7 (73),
   B.G.Kenny & G.N.Taylor, PR D21, 2720 (80).
9. F.J.Gilman & Inga Karliner, PR D10, 2194 (74).
10. R.Torgepson, PR D10, 2951 (74).
11. D.H.Boal, R.H.Graham, J.W.Moffat, PRL 36, 714 (74).
12. P.Hays & M.V.K.Ulehla, PR D13, 1339 (76).
13. P.J.O'Donnell, PRL 36, 177 (76).
14. Etim-Etim & M.Greco, NC 42, 124 (74).
15. A.Bohm & R.B.Jesse, PR D18, 330 (77).
16. Robert L.Thews, PR D4, 3021 (76).

17. E.Takasugi, Preprint, COO-1545-176 (76).

18. T.Barnes, PL 63B, 65 (76).

19. G.J.Gounaris, PL 63B, 307 (76).

20. Laurie M.Brown & Paul Singer, PR D15, 3484 (77).

21. B.J.Edwards & A.N.Kamal, PRL 36, 241 (76).

22. G.Grunberg & F.M.Renard, NC 33A, 617 (76).

23. N.Chase & M.T.Vaughn, PL 61B, 175 (76).

24. B.J.Edwards & A.N.Kamal, PR D15, 2019 (77).

25. C.H.Albright & R.J.Oakes, PR D15, 888 (77).

26. L.Maharana & P.S.Misra, PR D18, 2530 (78).

27. L.F.Ursutia, PR D18, 819 (78).

28. B.J.Edwards & A.N.Kamal, Preprint, SLAC-PUB-2303 (79).

29. Riazuddin & Fayyazuddin, Hadronic Journal 1, 1581 (78).

30. D.E.Andrews et al., PRL 38, 198 (77).

31. R.G.Kalbfleisch et al., PRL 13, 349 (64).

32. P.M.Dauher et al., PRL 13, 449 (64).

33. M.Goldberg et al., PRL 13, 249 (64).

34. J.Badier et al., PL 17, 337 (65).

35. R.Davis et al., PL 27B, 532 (68).

36. M.Aguilar-Benitez et al., PR D6, 29 (72).

37. M.Aguilar-Benitez et al., PRL 25, 1635 (70).

38. J.S.Danburg et al., PR D8, 3744 (73).

39. S.M.Jacobs et al., PR D8, 8 (73).

40. G.R.Kalbfleisch et al., PR D11, 978 (75).

41. D.M.Binnie et al., PL 83B, 141 (79).

42. G.S.Abrams et al., PRL 43, 477 (79),

W. Bartel et al., PL 113B, 190 (82),

A. Cordier, Talk given at the 4-th Seminar on Physics, College de France, March 11-12,1982, Preprint, LAL 82/12.

43. M.Aguilar-Benitez et al., PR D8, 18 (73).

44. D.Benaksar et al., PL 42B, 511 (72).

45. J.L.Rosner & E.W.Colglazer, PRL 26, 933 (71).

46. J.Babcock & J.L.Rosner, PR D14, 1286 (76).

47. N.Stanton et al., PL 92B, 353 (80).

48. Paul Singer, PR, 1989 (62).

49. R.Aviv & S.Nossinov, PR D2, 209 (70).

50. Naomi Levi & Paul Singer, PR D3, 2134 (71).

51. S.M.Flatte et al., PR 145, 1050 (66).

52. D.Berg et al., PRL 44, 706 (80).

53. A.B.Wicklund et al., PR D17, 1197 (78).

54. B.N.Ratcliff et al., PL 38B, 345 (78).

55. B. Rossi, "High Energy Particles", Prentice-Hall, (pages 81-83).

56. H. Messel and D.F. Crawford, "Electron-Photon Shower Distribution Function Tables For Lead, Copper and Air Absorber", Pergamon Press (1970).

57. ZGS User's Handbook, Argonne National Laboratory (1974).

58. J.D. Jackson, NC 34, 1644 (64).

59. Suh Urk Chung, CERN report 71-8 (71).

60. Charles Zemach, PR 133, B1201 (64).

61. Jerry Friedman, SAGE, A General System for Monte Carlo Event Generation with Preferred Phase Space Density Distributions, University of California, Lawrence Radiation Laboratory, Group A Programing note #P-189 (71).

62. Longo and Sestilli, NIM 128, 283-307 (75).

63. Feld, Bernard T., Models of Elementary Particles, Blaisdell Publishing Company, 1969 (Chapter 15).

64. Kokkede J.J., The Quark Model, W.A. Benjiamin, Inc. 1969 (Chapters 11 and 12).

65. Becci & Morpugo, PR 140, B687 (65).

Abbreviations:

PR - Physical Review

PRL - Physical Review Letters

PL - Physics Letters

NC - Nuovo Cimento

NIM - Nuclear Instruments & Methods

FIGURE CAPTIONS

Fig.5-11(a-j) Fit of Monte Carlo background $M(\pi\pi\gamma)$ spectra ($\circ$) to data (__ the solid line), where different energy correction factors were used in Monte Carlo.

Fig.5-12(a,b) Fit of Monte Carlo background $M(\pi\pi\gamma)$ spectrum ($\circ$) to data (__).

a) Monte Carlo ω background spectrum shifted down by 10 Mev.

b) Gaussian, used for bonafide $\omega \rightarrow \pi\pi\gamma$ decays, shifted down by 10 Mev.

Fig.6-1 Fit of the data (__) $M(\pi^+\pi^-\gamma)$ to the sum of the Monte-Carlo generated $M(\pi^+\pi^-\gamma)$ with one gamma missing spectra for η and ω, gaussians for η' and η and a polynomial background ($\circ$).

Fig.6-2 Fit of data E_γ (__), to the sum of Monte-Carlo generated E_γ spectra scaled to the numbers of events obtained from the fit to the mass spectrum $M(\pi^+\pi^-\gamma)$, and a polynomial background ($\circ$).

Fig.6-3 Fit of the data $M(\pi^+\pi^-)$ (__) to the sum of Monte-Carlo generated $M(\pi^+\pi^-)$ spectra scaled to the number of events obtained from the fit to the mass spectrum ($M(\pi^+\pi^-\gamma)$), and a polynomial background ($\circ$).

Fig.6-4 $M(\pi^+\pi^-\gamma)$ with all cuts from Fig.5-10, for the events with $M(\pi^+\pi^-)$ in the ρ mass range $0.65 < M(\pi^+\pi^-) < 0.85$ Gev.

Fig.7-17 $M(\eta\gamma)$ with gamma energy cuts and $M(\pi^+\pi^-\pi^0) < 0.58$ Gev.

Fig.7-18a M(rec) Monte-Carlo with gamma energy cuts and $M(\pi^+\pi^-\pi^0) < 0.58$ Gev.

Fig.7-18b M(rec) with gamma energy cuts and $M(\pi^+\pi^-\pi^0) < 0.58$ Gev.

Fig.7-19 M(rec) with gamma energy cuts, $M(\pi^+\pi^-\pi^0) < 0.58$ Gev and $0.72 < M(\eta\gamma) < 1.2$ Gev.

Fig.7-20 $M(\eta\gamma)$ with gamma energy cuts, $M(\pi^+\pi^-\pi^0) < 0.58$ Gev and $0.5 < M(rec) < 1.2$ Gev.

TABLE 2-1

BEAM CHARACTERISTICS

Momentum -	8.45 Gev/c
Beam Spill -	600 msec (FWHM)
Final Focus Spot Size -	.5" * .5"
Flux -	6 * 10^4 pions per pulse
Production Angle -	1.5 degrees
Momentum Bite -	2.5%
$\Delta P/P$ -	.005
Beam Spark Chamber:	
Spacing -	36"
Position Resolution -	Δx = .02" (FWHM)
Beam Direction:	
Angle resolution -	$\Delta\theta$ = .00002 rad
Measurement -	$\Delta x_{intercept}$ = .030"
Focus -	120" downstream of Hydrogen target
Hydrogen Target -	2" diameter * 16" length

TABLE 2-2

CHARGED PARTICLE SPECTROMETER CHARACTERISTICS

1. Spark Chambers-

		Rotation	Active Area	Distance from Target
Upstream	1	0°	24" * 16"	19.00"
	2	45°	28" * 18"	24.50"
	3	0°	40" * 30"	29.75"
	4	45°	42" * 36"	35.00"
	5	0°	40" * 40"	40.50"
Downstream	1	15°	5' * 7'	91.50"
	2	15°	5' * 7'	97.50"
	3	0°	5' * 7'	103.50"
	4	0°	5' * 7'	109.50"
	5	0°	5' * 7'	115.50"

2. Magnet-

Type	Picture Frame	SCM-104
Nominal $\int B \cdot dl$	240 kGauss-inches	
Central Field	5.9 kGauss	
Size	84" W * 40" H * 40" D	
Center Position	63" from L_{H2} target	

continued...

TABLE 2-2

CHARGED PARTICLE SPECTROMETER CHARACTERISTICS (continued)

3. Chamber High Voltage-

Method	capacitor bank discharge
Capacitance	10 nfarads per 5' * 7' area of chamber
Pulse Hight	6.8 KV
Risetime	150 nsec
Delay	550 nsec
Clearing Field	75 V DC
Pulsed Field	1 KV - 600 nsec

4. Readout-

Method	magnetostrictive
System	SAC Midas, 6 scalers per plane

5. Resolution-

Position	0.05" (FWHM)
Momentum	4% (FWHM) at 2 Gev/c

TABLE 2-3

SCINTILLATION COUNTERS

NAME	SIZE	POSITION (Z_0 at L_{H_2} target Z downstream)	PURPOSE
S1	1/16"* 2" *1.5"	------	Detect Beam
B1	1/8" * 3" * 3"	-170"	
B2	1/16" * 2" * 2"	-36"	
BHR(ight)	1/4" * 16" * 24"	-25"	Reject Beam Halo
BHL(eft)	with 1" hole		
HO	1/8" * 17" 24" with 2" hole	+14"	Signals a Charged Particle at an Angle > 4° to the Beam
AA1	opening 26" * 16"	+23"	Rejects Particles Outside Fiducial Volume
AA2	Opening 40" * 40"	+42"	
H2	30 counters Each 1/8"*4"*42"	+122.8"	Charged Particle Hodoscope
BV1	1/4" * 4" * 4"	+124"	Reject Non-Interacting Beam
BV2		+129"	
GHF(ront)	16 counters	+140"	No Gamma Hodoscope
GHR(ear)	Each 1/4"*7.5"*30"	+143.5"	Yes Gamma Hodoscope
Target Anti-Counters	See Figure 2-6		Reject Extra Particles at Wide Angles from Target

TABLE 5-1

KINEMATIC CUTS.

1. Charged particle momenta	> 0.4 Gev/c
2. Gamma ray energy	> 0.7 Gev
3. Recoil particle mass	> 1.5 Gev

GEOMETRIC CUTS.

1. All charged and gamma ray trajectories are within the detector by	1"
2. Gamma ray to charged particle distance at lead converter	> 5"

TABLE 5-2

# OF EVENTS	CUTS
45577	All DST Events
29661	E_γ > 1.5 Gev
8997	E_γ > 1.5 gev, $\|t'\|$ > 0.2 $(Gev/c)^2$
6495	E_γ > 1.5 gev, $\|t'\|$ > 0.2 $(Gev/c)^2$, T_{MM} < 0.22 Gev, $T_{\pi^\pm}$ > 1.0 Gev
4647	E_γ > 1.5 gev, $\|t'\|$ > 0.2 $(Gev/c)^2$, T_{MM} < 0.22 Gev, $T_{\pi^\pm}$ > 1.0 Gev, χ^2_{prob} > 0.1

TABLE 5-3

MONTE-CARLO CALCULATED ACCEPTANCES

	$\eta\to\pi^+\pi^-\gamma$	$\eta\to\pi^+\pi^-\pi^0$	$\omega\to\pi^+\pi^-\gamma$	$\omega\to\pi^+\pi^-\pi^0$	$\eta'\to\rho\gamma$
Acc.	0.0446	0.0167	0.0709	0.0269	0.0565
Error	7%	7%	7%	7%	7%

TABLE 7-1

KINEMATIC CUTS.

1. Charged particle momenta	> 0.4 Gev/c
2. E_{γ_1} and E_{γ_2} (energy of gamma 1 and 2)	> 0.4 Gev
2. E_{γ_3} (energy of gamma 3)	> 0.7 Gev
4. Recoil particle mass squared	$0 < M^2_{rec} < 1.6$ Gev ^{2}

GEOMETRIC CUTS.

1. All charged and gamma ray trajectories are within the detector by	1"
2. Gamma ray to charged particle distance at lead converter	> 5"

TABLE 7-2

# OF EVENTS	CUTS (in addition to the cuts from Table 7-1)
1265	$M_{\pi^+\pi^-\pi^o} < 0.65$ Gev
596	$0.6 < E_{\gamma_1} < 3.2$, $0.4 < E_{\gamma_2} < 2.0$, $1. < E_{\gamma_3} < 4.5$ Gev $1. < E_{\gamma_1\gamma_2} < 4.5$, $M_{\pi^+\pi^-\pi^o} < 0.58$ Gev
335	$0.6 < E_{\gamma_1} < 3.2$, $0.4 < E_{\gamma_2} < 2.0$, $1. < E_{\gamma_3} < 4.5$ Gev $1. < E_{\gamma_1\gamma_2} < 4.5$, $0.105 < M_{\gamma_1\gamma_2} < 0.165$, $M_{\pi^+\pi^-\pi^o} < 0.58$ Gev
152	$0.6 < E_{\gamma_1} < 3.2$, $0.4 < E_{\gamma_2} < 2.0$, $1. < E_{\gamma_3} < 4.5$ Gev $1. < E_{\gamma_1\gamma_2} < 4.5$, $0.105 < M_{\gamma_1\gamma_2} < 0.165$, $M_{\pi^+\pi^-\pi^o} < 0.58$ Gev $0.5 < M^2_{rec} < 1.2$ Gev^2

TABLE 8-1

3 γ EXPERIMENTAL CORRECTIONS

1.	Gamma conversion upstream of Lead converter	0.143 ± 0.013
2.	Gamma hodoscope rejection of good events	0.012 ± 0.001
3.	Gamma software reconstruction failure	0.030 ± 0.024
4.	Digitization scaler runout	0.
5.	Gamma partial chamber inefficiency	0.059 ± 0.040
6.	Beam contamination	0.026 ± 0.006
7.	Charged pion interaction in detector	0.040 ± 0.014
8.	Counter inefficiency	0.032 ± 0.008
9.	Tight trigger losses	0.244 ± 0.014
10.	Gamma conversion inefficiency	0.302 ± 0.061
11.	π^0 losses in $\gamma_1\gamma_2$ and $\gamma_2\gamma_3$ convertors	0.10 ± 0.01

Overall correction 0.342 ± 0.050

TABLE A-1

DECAY MATRIX ELEMENTS AND ANGULAR DISTRIBUTIONS

	J^P	$l_{\pi^+\pi^-}$	$\lvert M\rvert^2$	$dN/d\theta$
$\eta\to\pi^+\pi^-\gamma$	0^-	1	$p^2 * q^2 * M^2_{\pi^+\pi^-}$	$1 - \cos^2\theta$
$\eta\to\pi^+\pi^-\pi^0$	0^-	0	$1 * (1+ a*Y)$ $a=-1.07,\ Y=3T_0/Q-1$	1
$\omega\to\pi^+\pi^-\gamma$	1^-	0	$p^2 * M^2_{\pi^+\pi^-}$	1
$\omega\to\pi^+\pi^-\pi^0$	1^-	1	$p^2 * q^2$	$1 - \cos^2\theta$
$\eta'\to\pi^+\pi^-\gamma$	0^-	1	$p^2 * q^2 * M^2_{\pi\pi}$	$1 - \cos^2\theta$

p - momentum of a pion in the $M_{\pi^+\pi^-}$ C.M.S.

q - momentum of the gamma (or π^0) in the meson C.M.S.

T - kinetic energy

Q - total energy

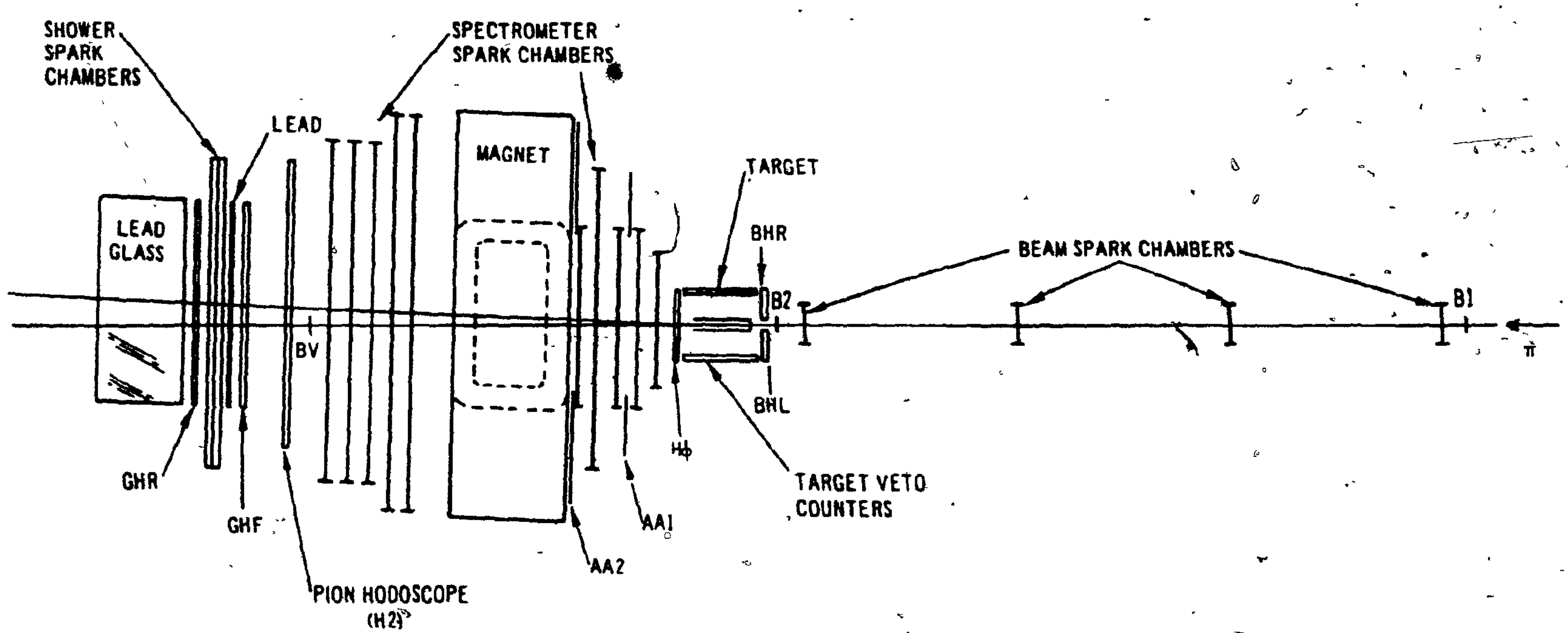

Fig. 2-1. Experimental Layout

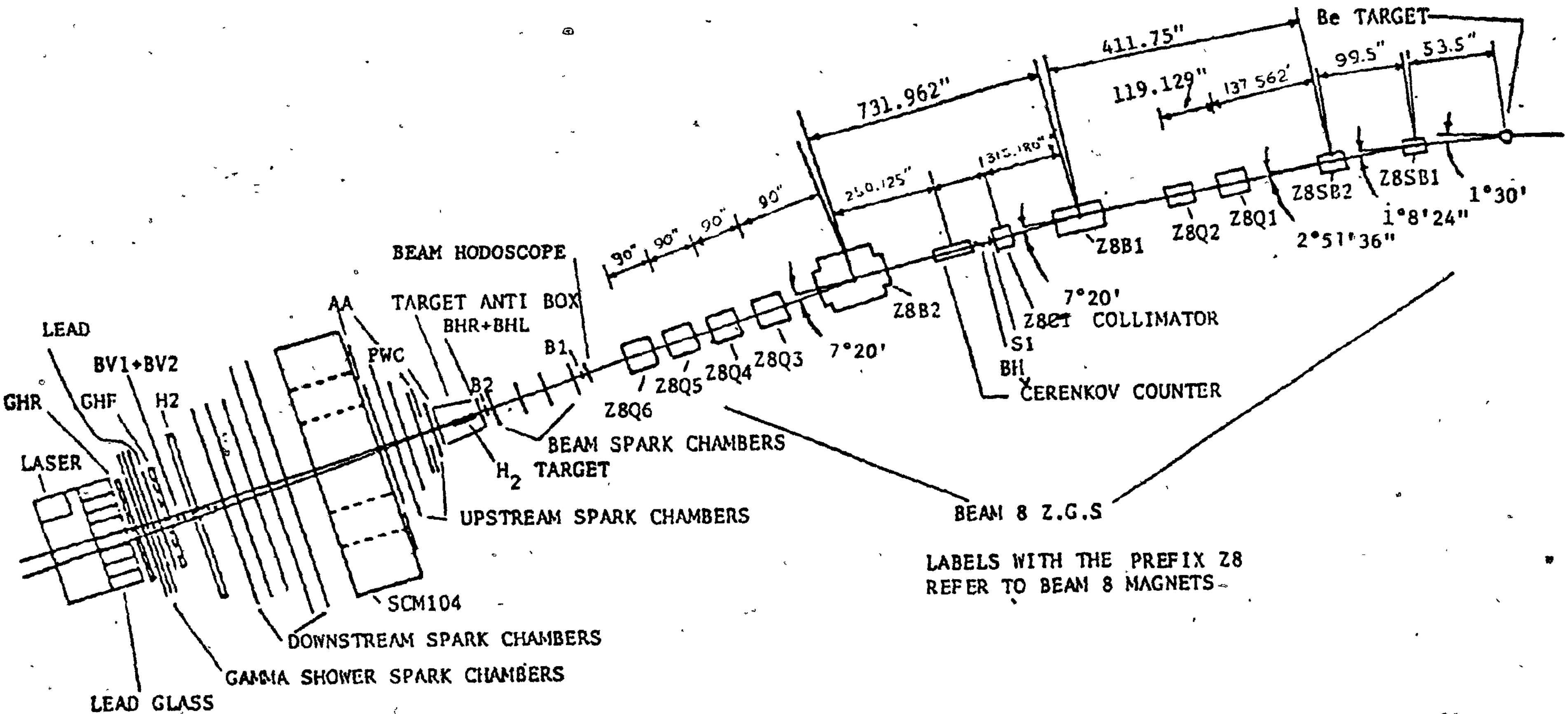

Figure 2-2 Beam Layout

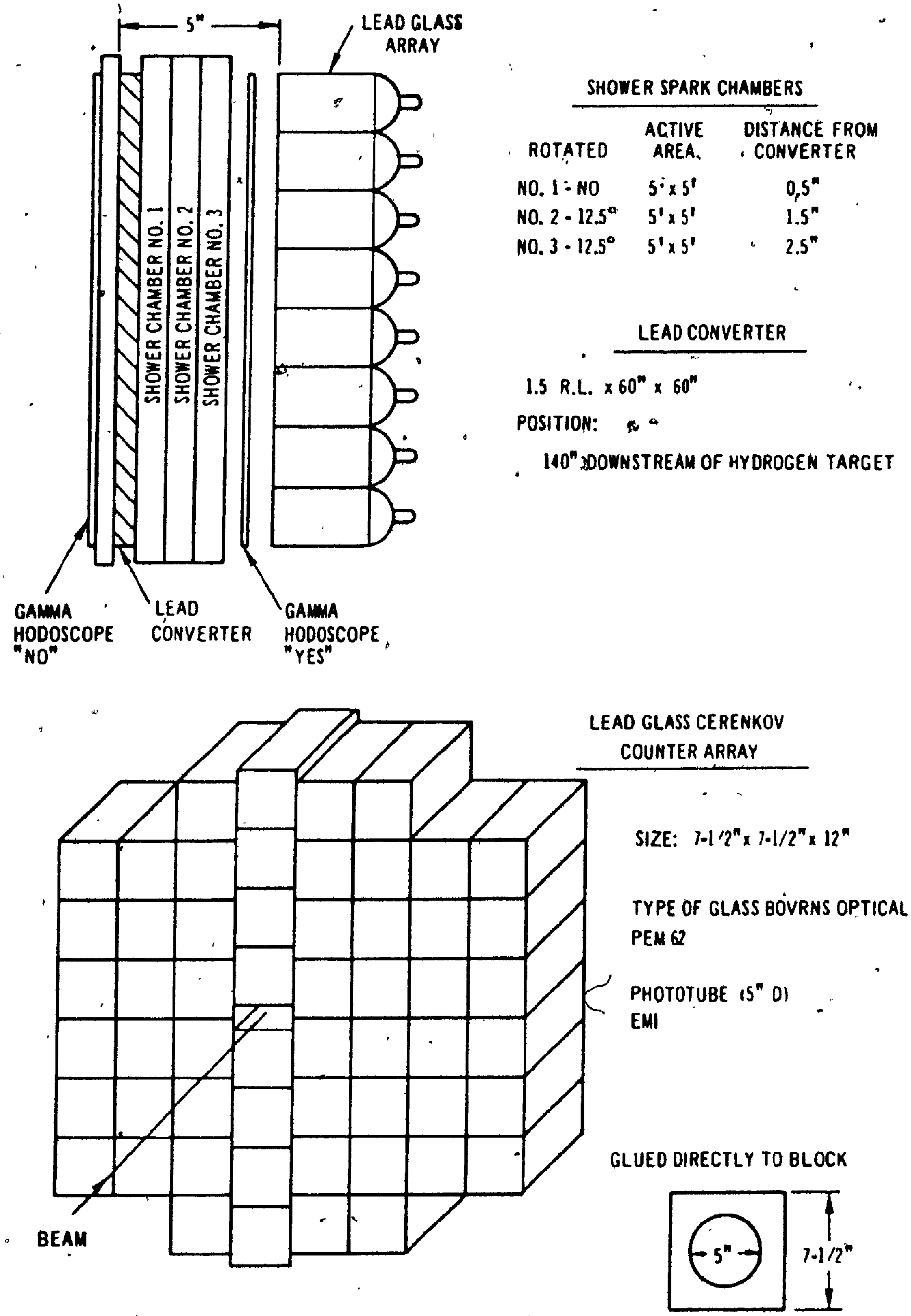

Figure 2–3. Gamma Detector

1) Formation of Histogram for Block #N

A) Calculate Di-Gamma Mass For All Block #N Events

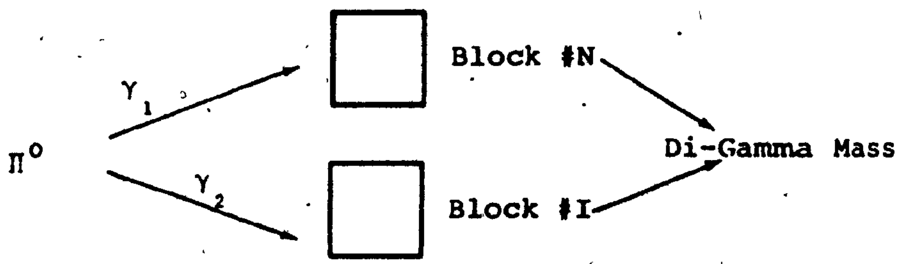

B) Sum Over All Blocks

$$\sum_{I=1}^{56}$$

C) Find Centroid Of Di-Gamma Mass Distribution And Compare With True π^0 Mass

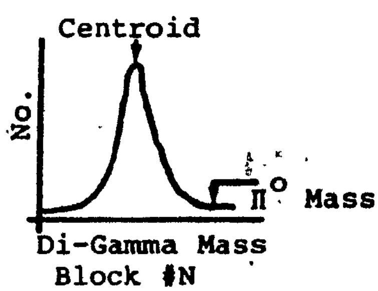

2) Correct Tube Gain For Block #N by Ratio

$$\left(\pi^0 \text{ Mass} \Big/ \text{Centroid Mass}\right)^{1/2}$$

Figure 2-4. Method For Lead Glass Energy Calibration

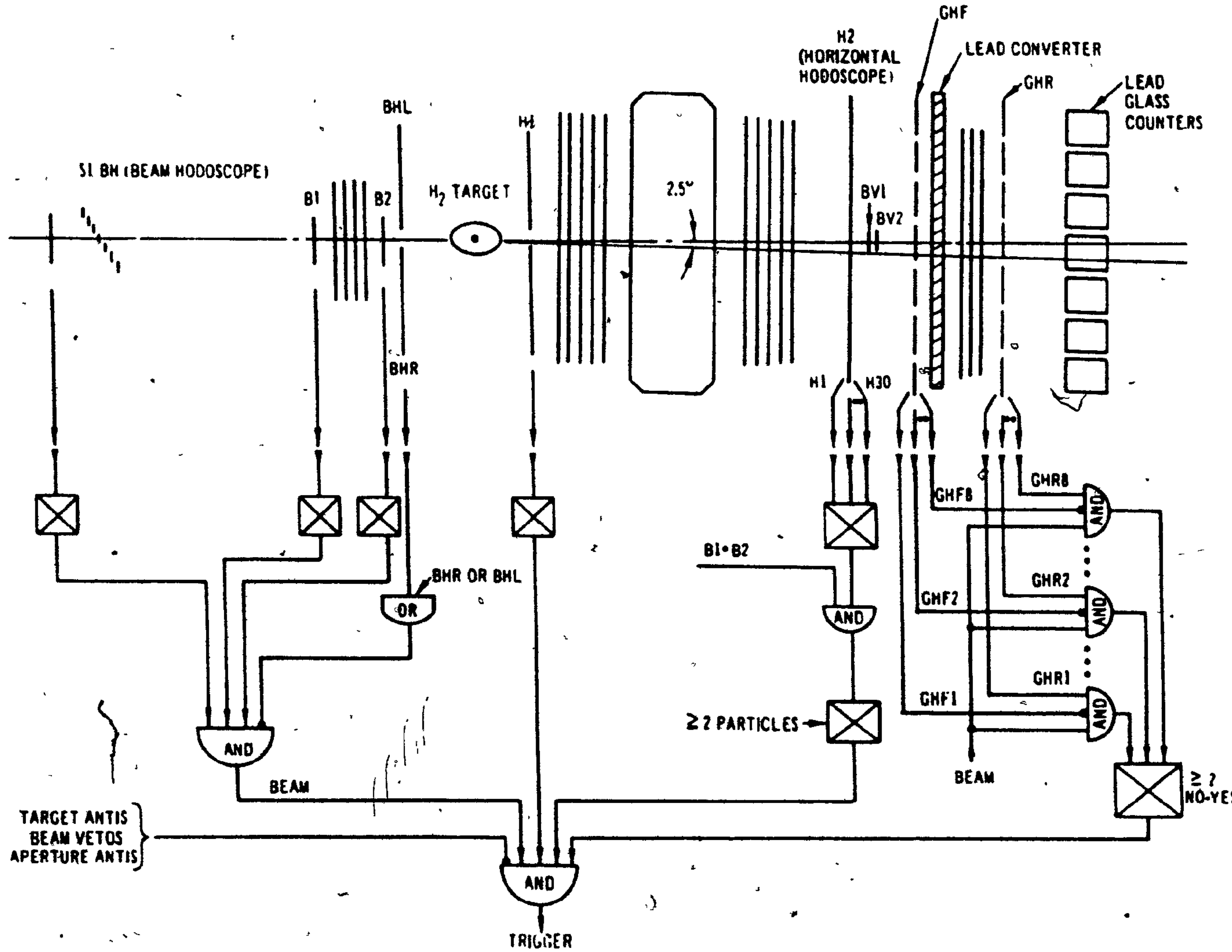

Fig.2-5. Simplified Trigger Diagram

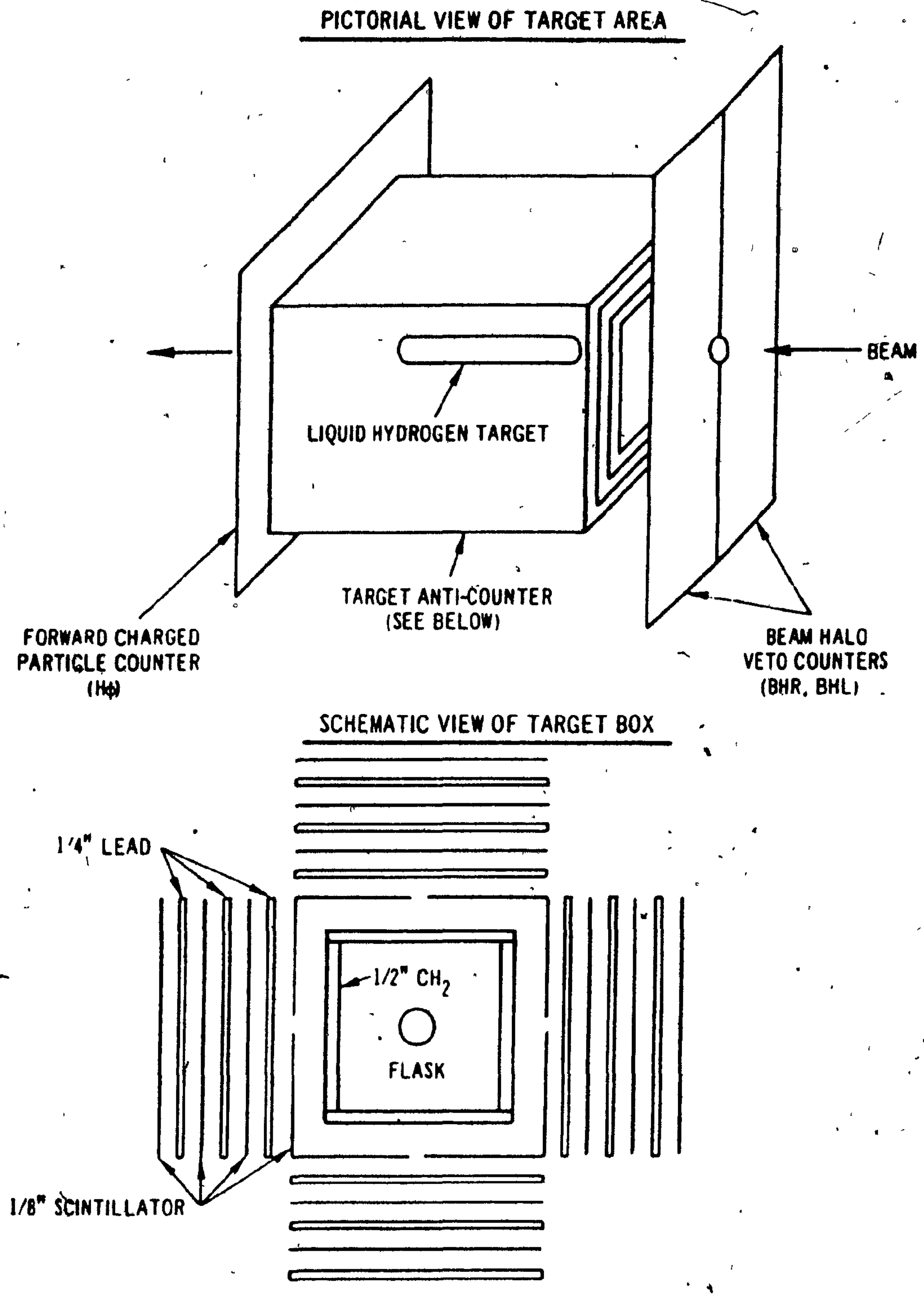

Figure 2–6 Target Anti-counter System

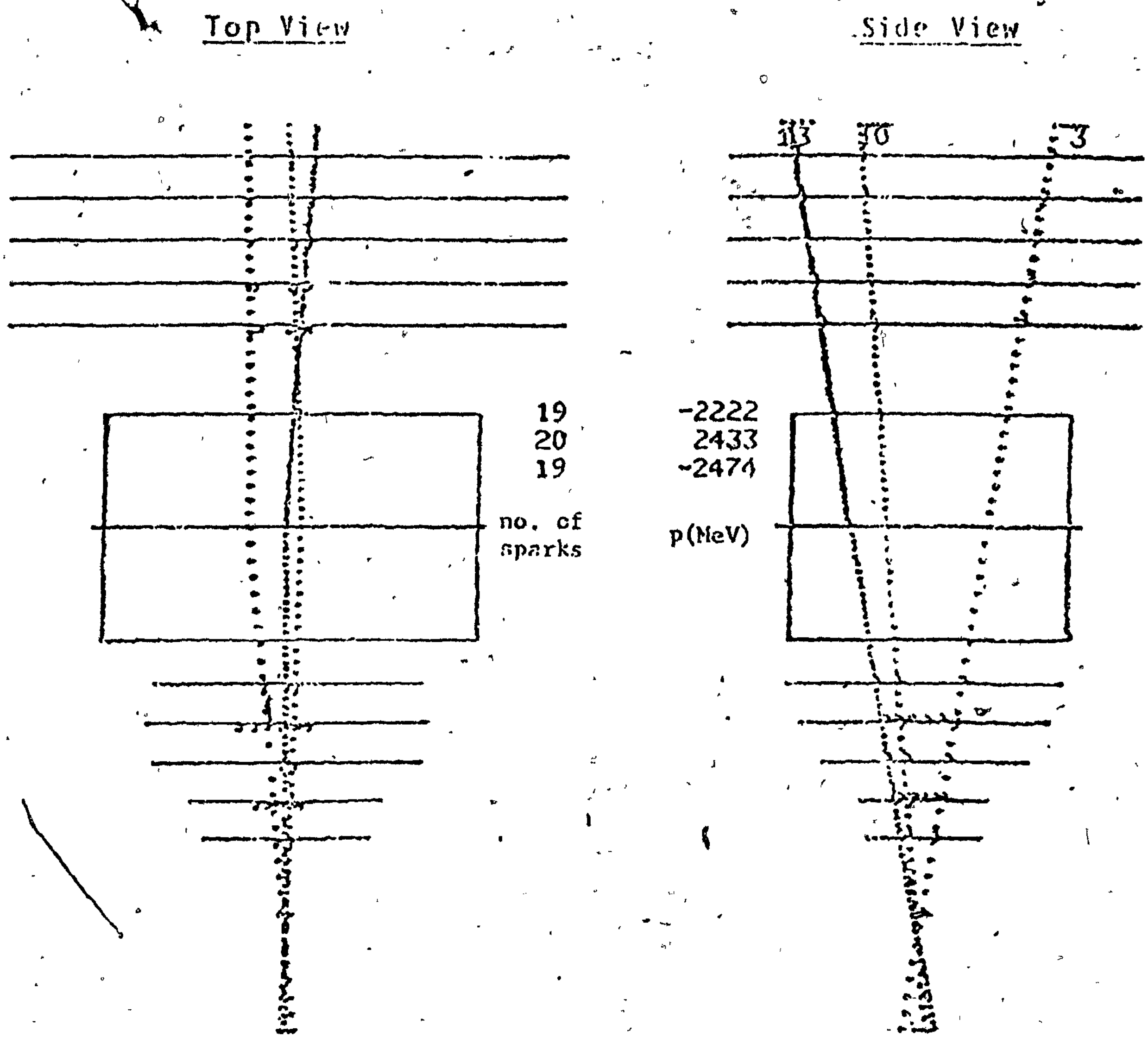

Figure 3-1. Example of a Reconstructed Three prong Event

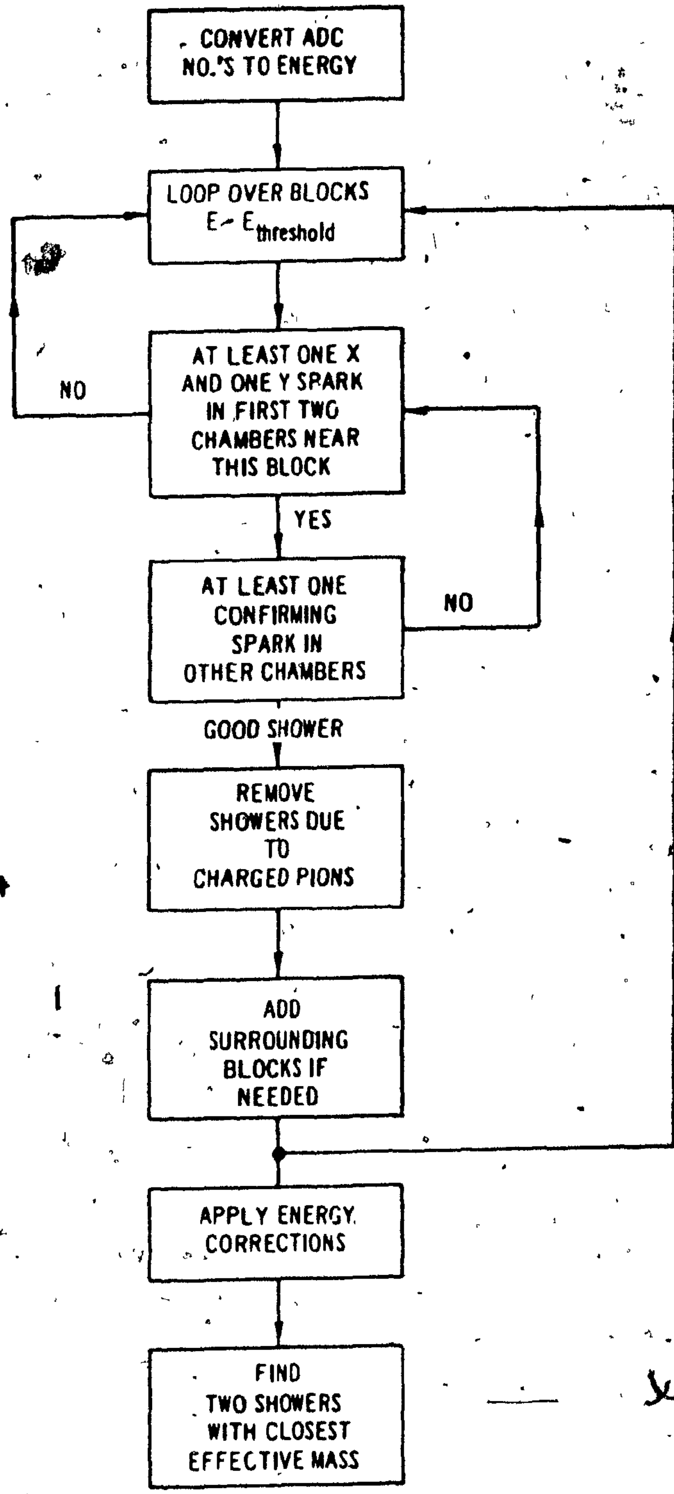

Figure 3-2 Flow Chart of Gamma Shower Reconstruction

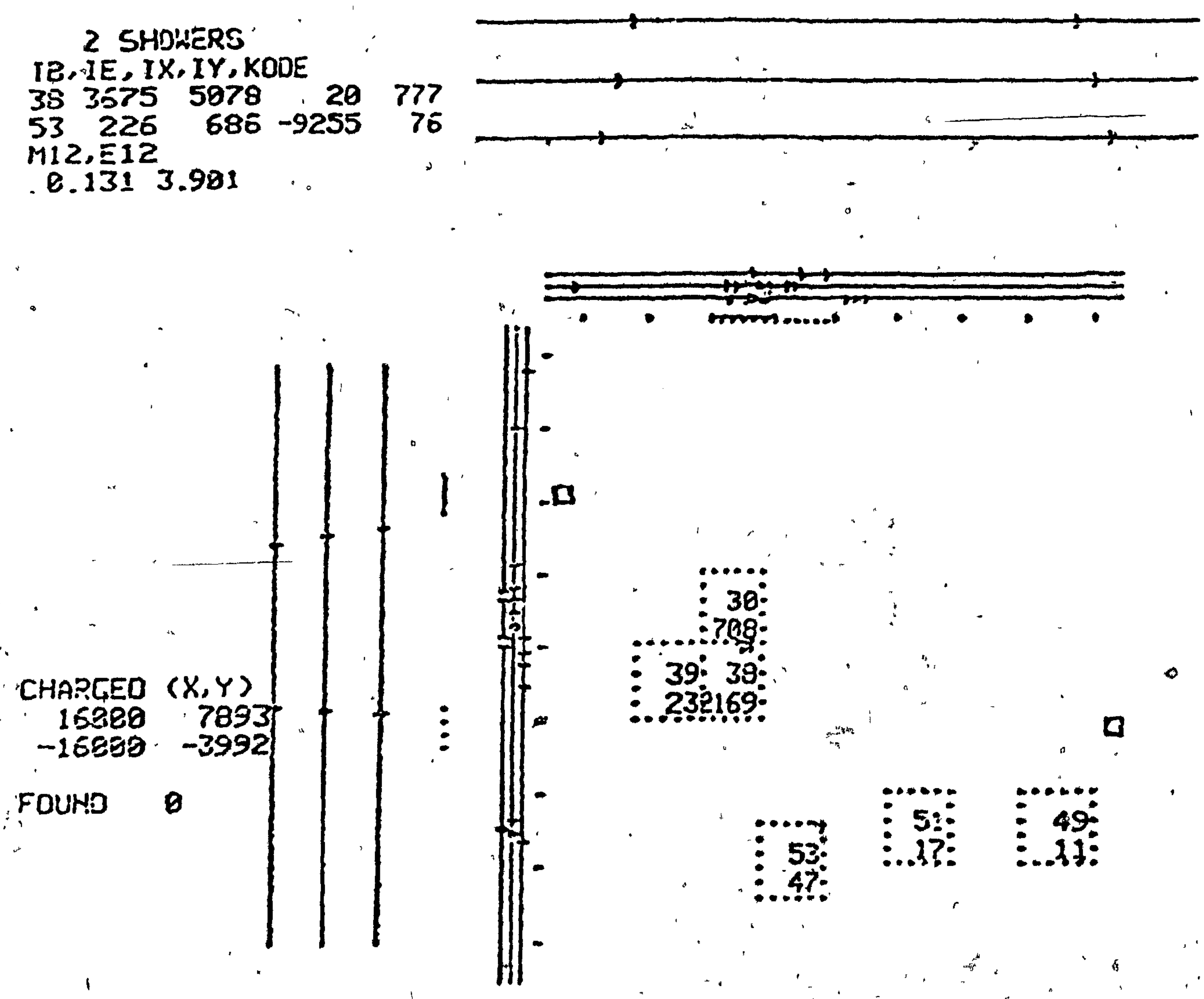

Figure 3.3 A Reconstructed 2γ Event

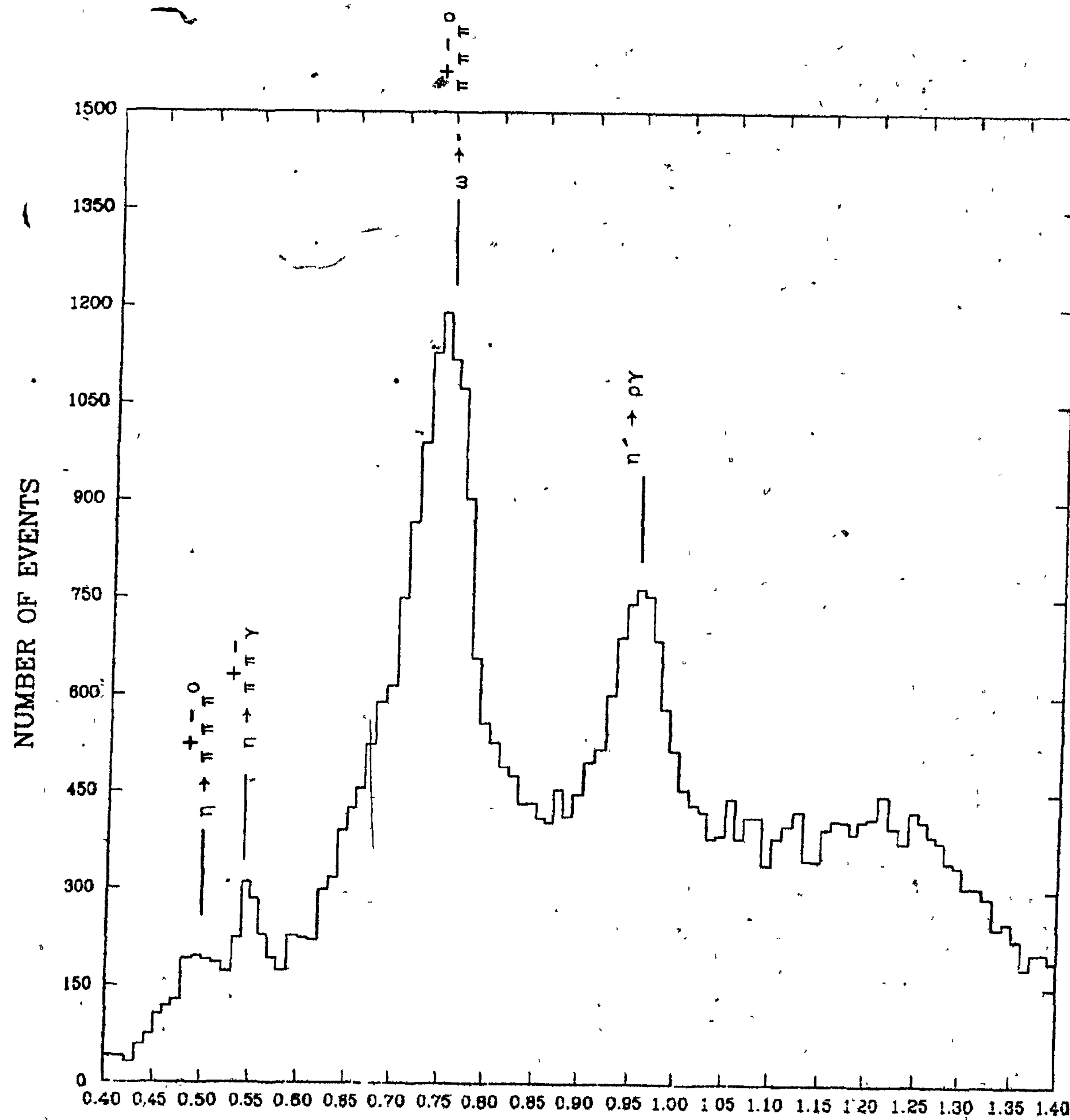

FIG.5-1. $M_{\pi^+\pi^-\gamma}$ unfitted. All DST events.

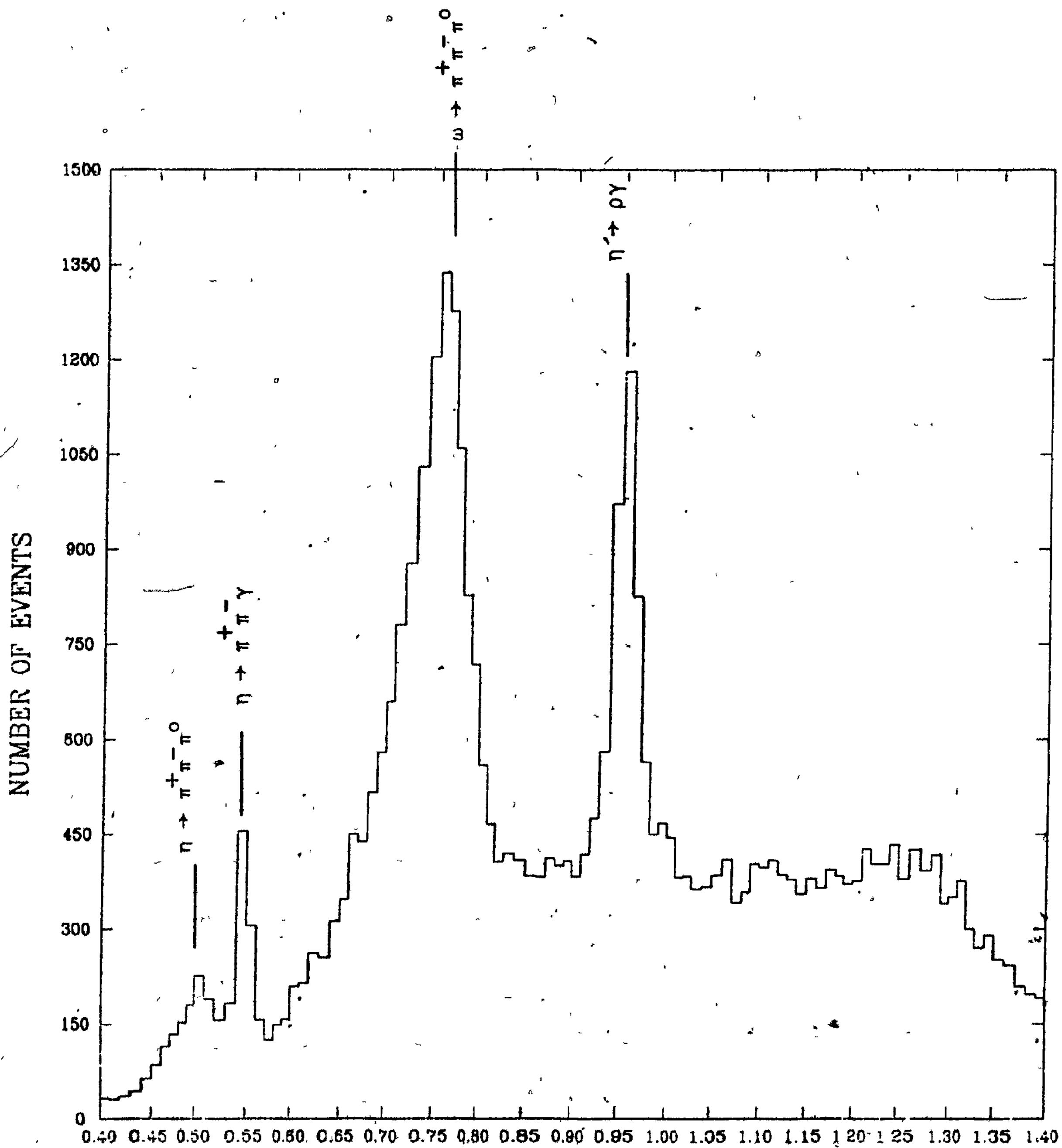

FIG.5−2. $M_{\pi^+\pi^-\gamma}$ 1C fit. All DST events.

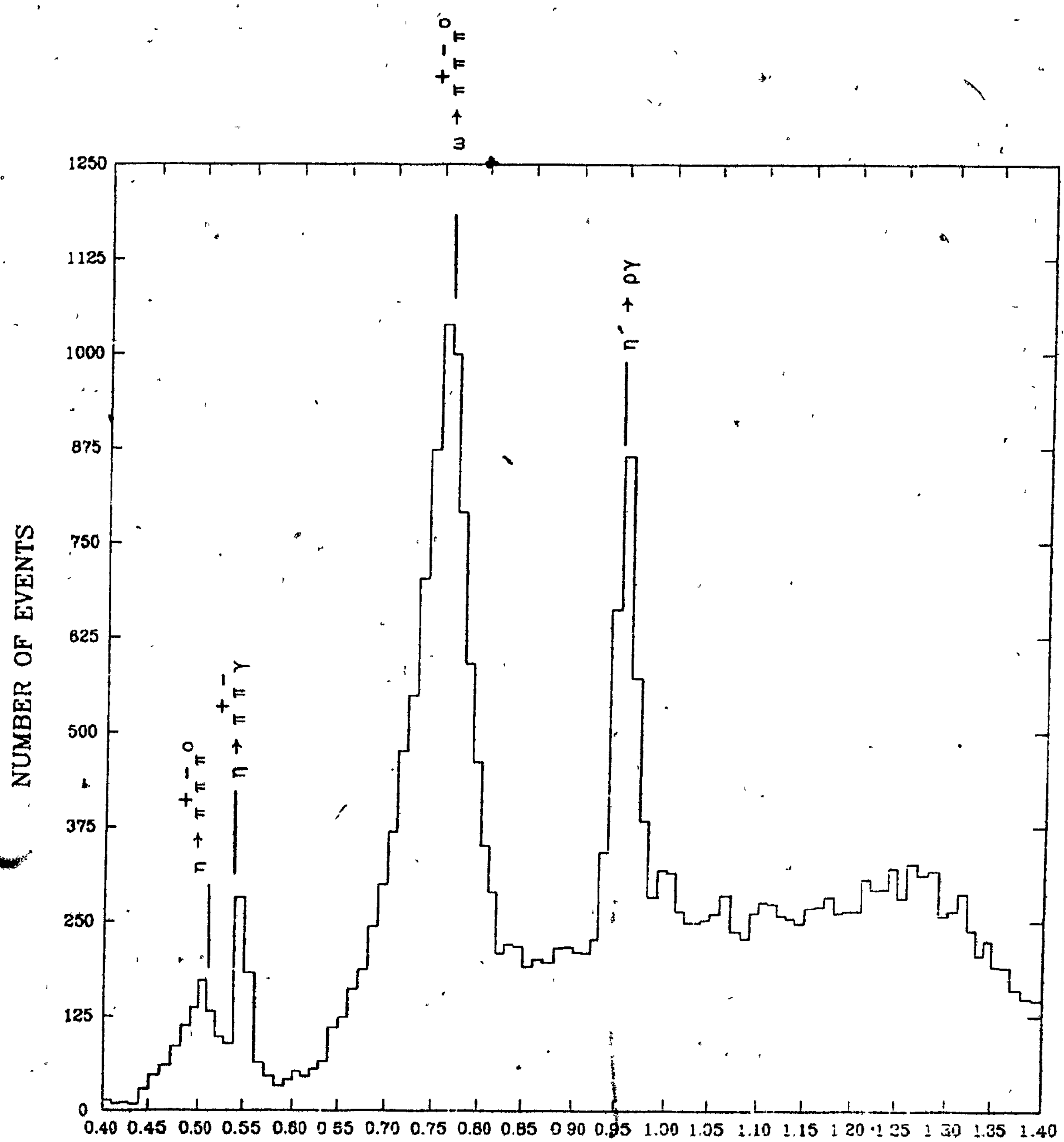

FIG.5–3. $M_{\pi^+\pi^-\gamma}$ 1C fit. $E_\gamma > 1.5$ Gev.

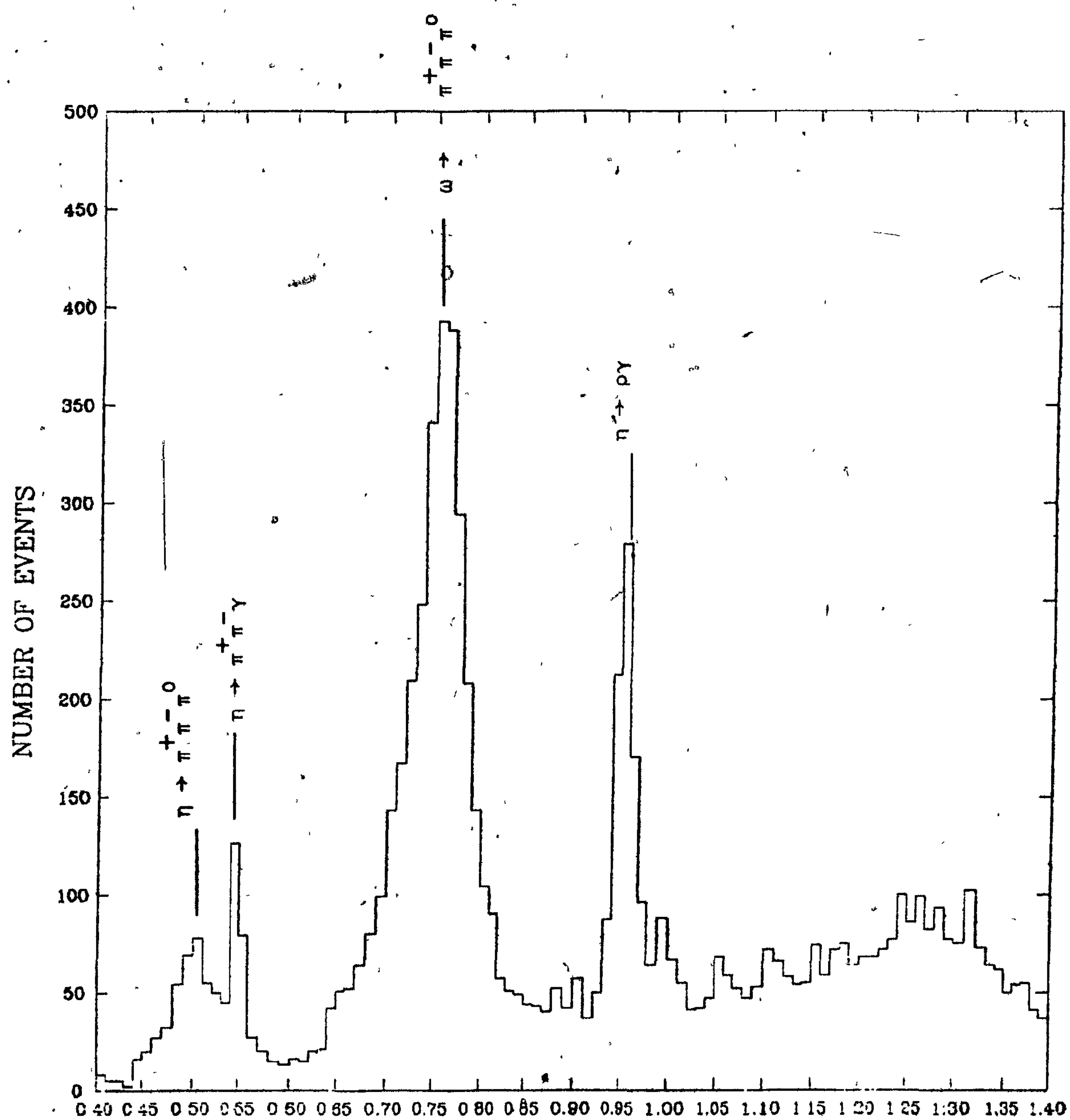

FIG.5−4 $M_{\pi^+\pi^-\gamma}$ 1C fit $E_\gamma > 1.5$ Gev, $|t'| > .2\ (\text{Gev}/c)^2$, $T_{MM} < .22$ Gev

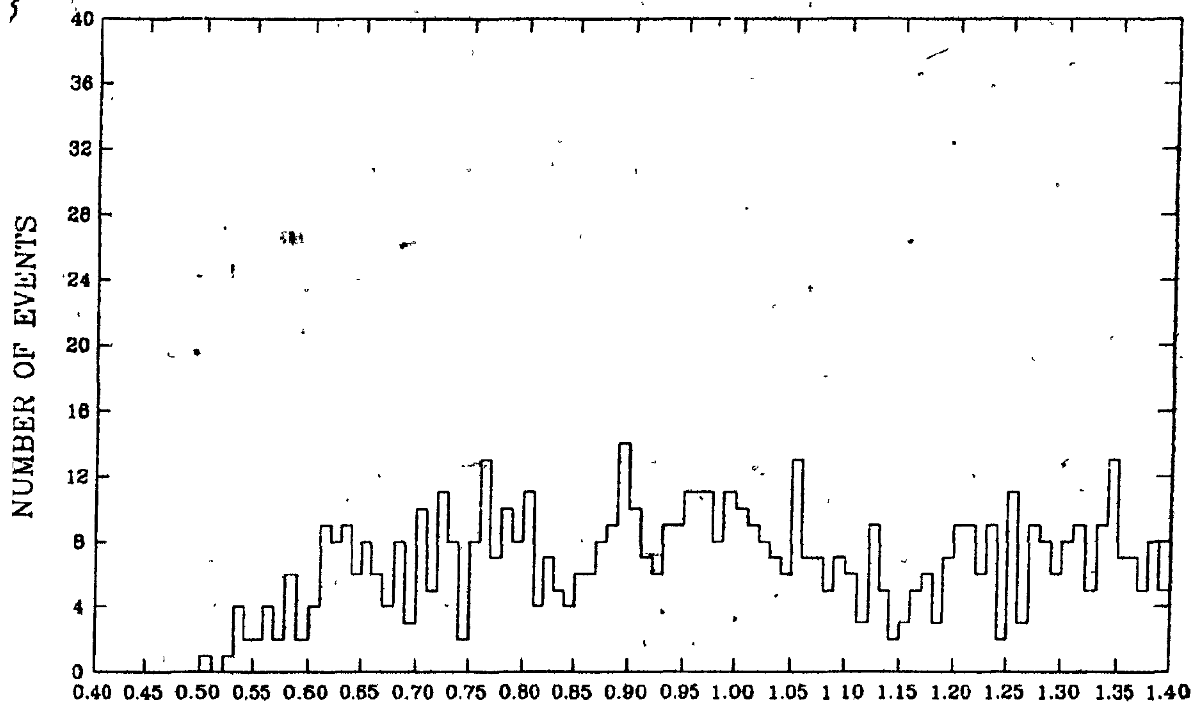

FIG.5–5. $T_{\pi}+$ for η mass region of Fig.5–4.

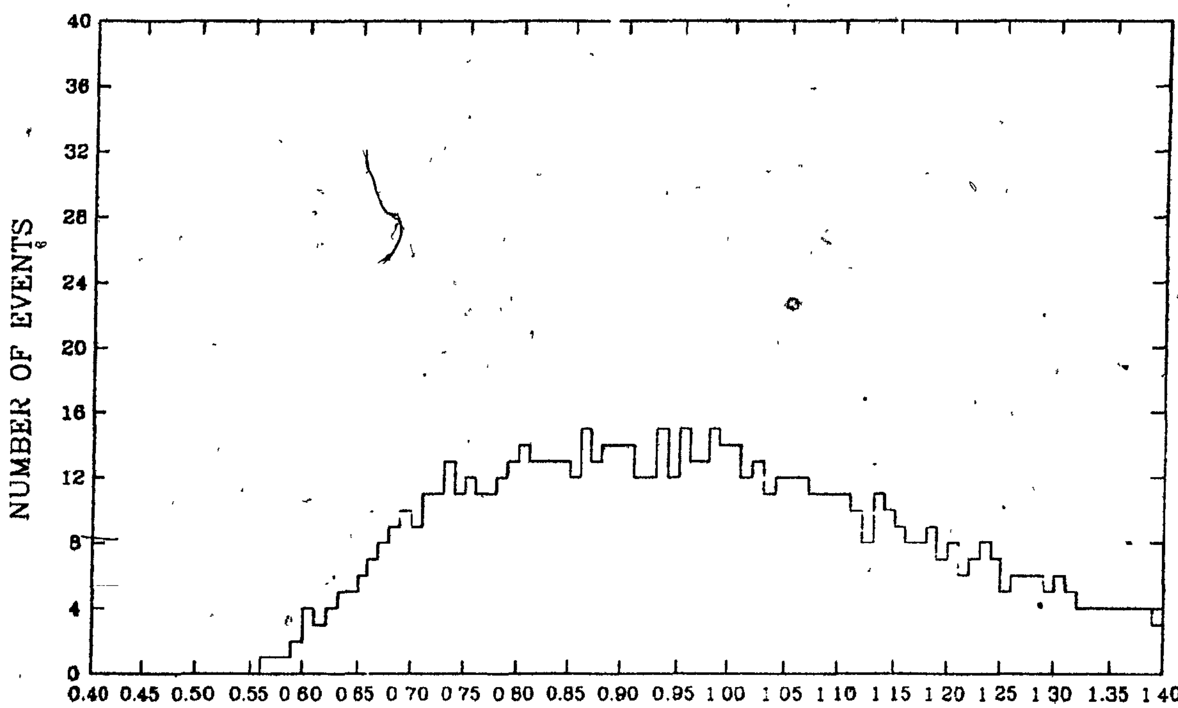

FIG.5–6. $T_{\pi}+$ Monte–Carlo for $\eta \dashrightarrow \pi^{+}\pi^{-}\gamma$ decay.

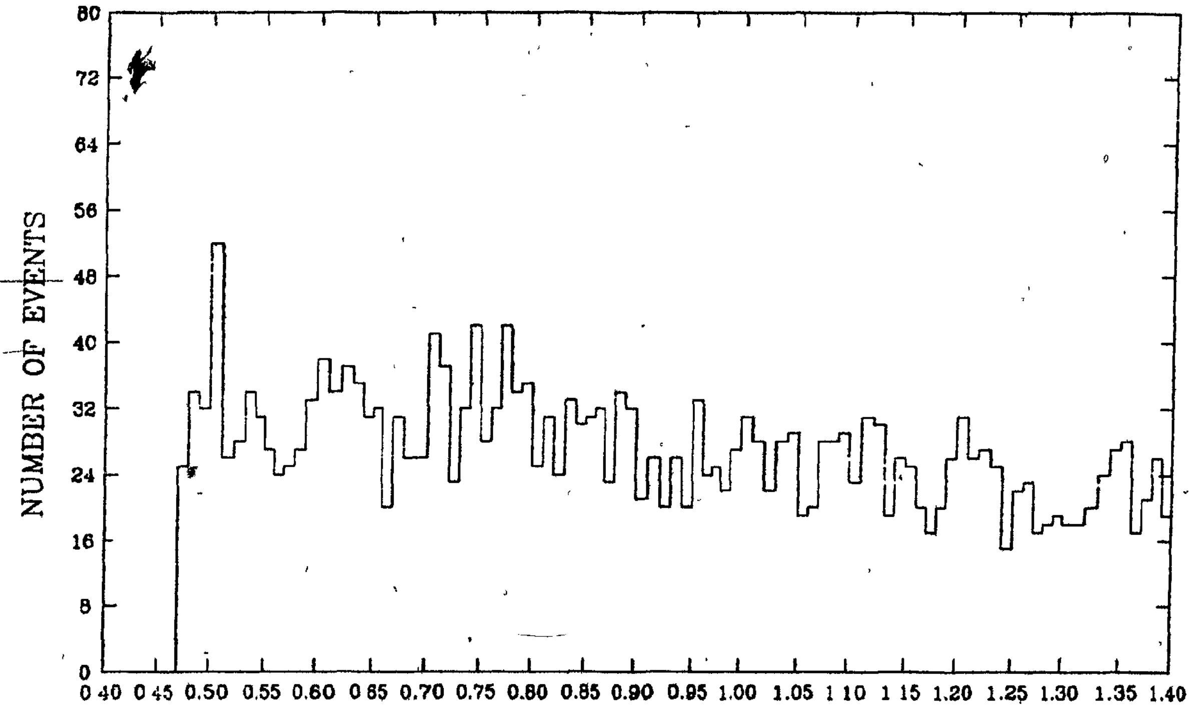

Fig.5-7. T_{π^+} for η' mass region of Fig.5-4.

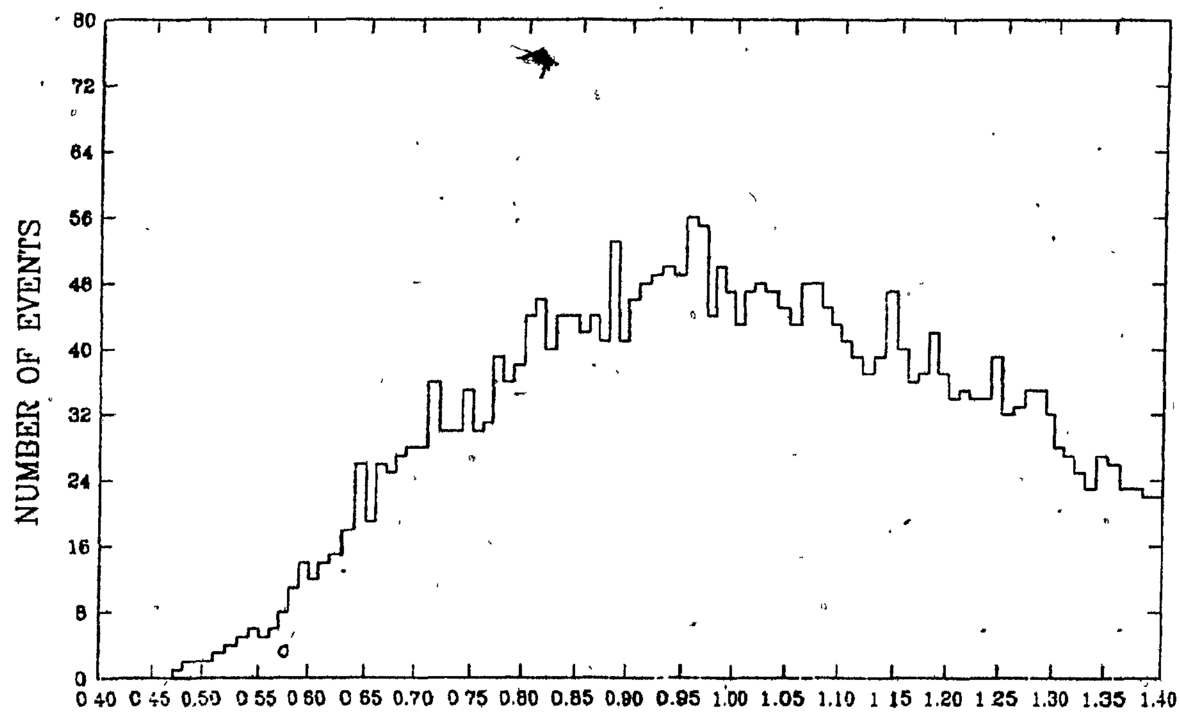

FIG.5-8. $T_{\pi}{}^{+}$ Monte-Carlo for $\eta' \dashrightarrow \rho\gamma$ decay, $T_{MM} < .22$ Gev

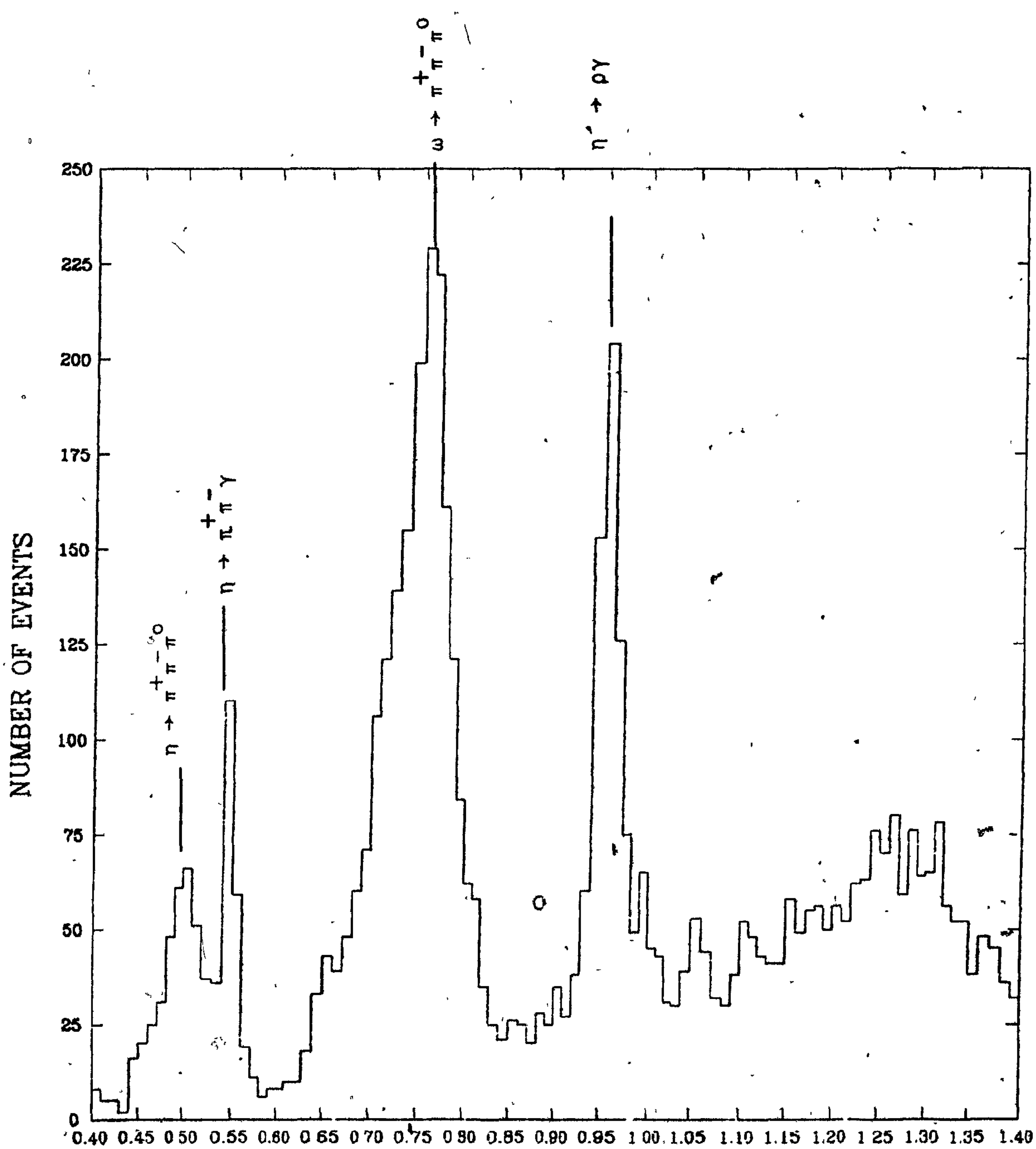

FIG.5-9. $M_{\pi^+\pi^-\gamma}$ 1C fit $E_\gamma > 1.5$ Gev, $|t'| > .2$ (Gev/c), $T_{\pi^\pm} > 1$ Gev

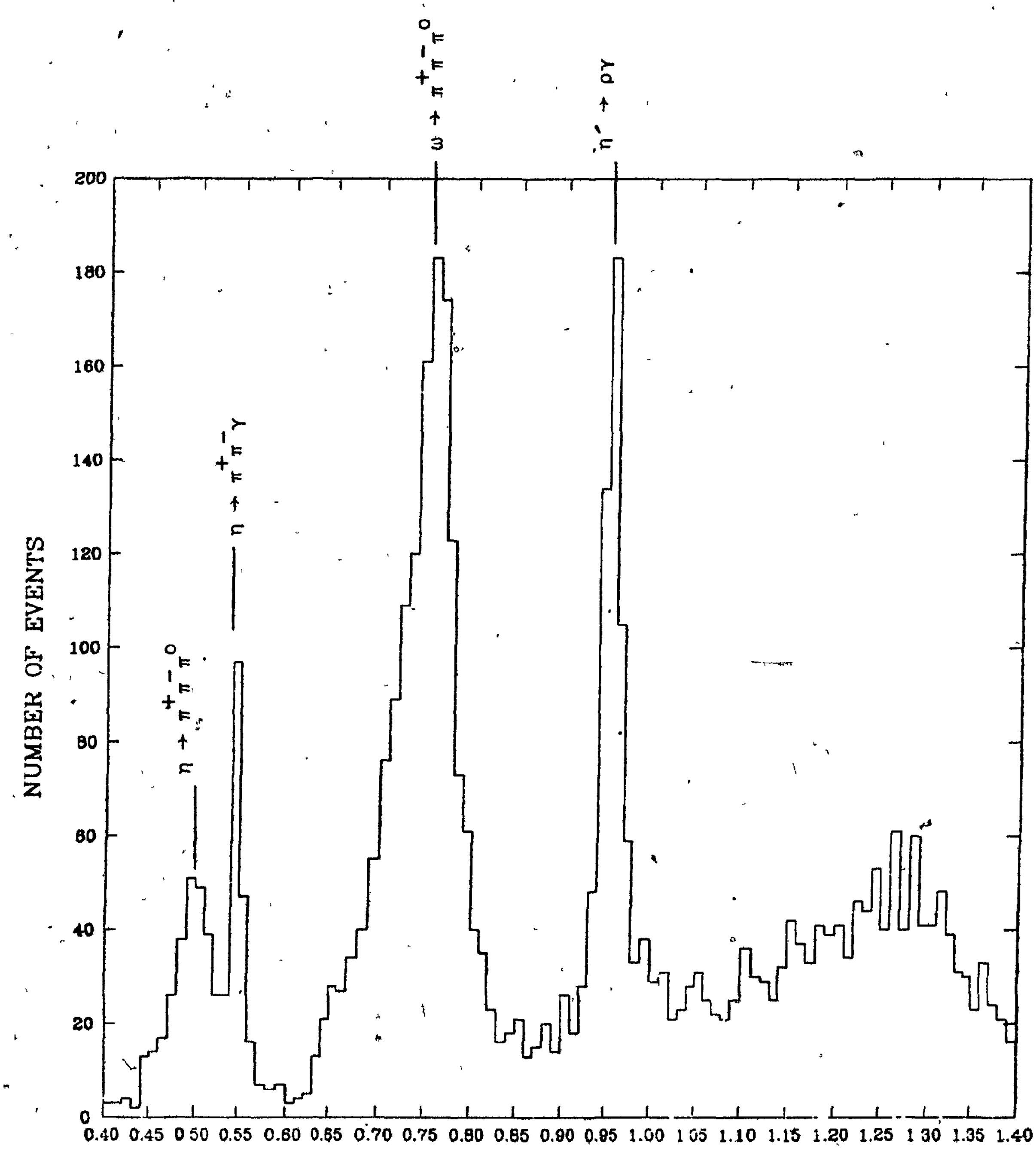

FIG.5–10. $M_{\pi^+\pi^-\gamma}$ 1C fit. $E_\gamma > 1.5$ Gev, $|t'| > .2\ (\mathrm{Gev}/c)^2$, $T_{\pi^\pm} > 1$ Gev,

$\chi^2_{\mathrm{probability}} > 0.1$

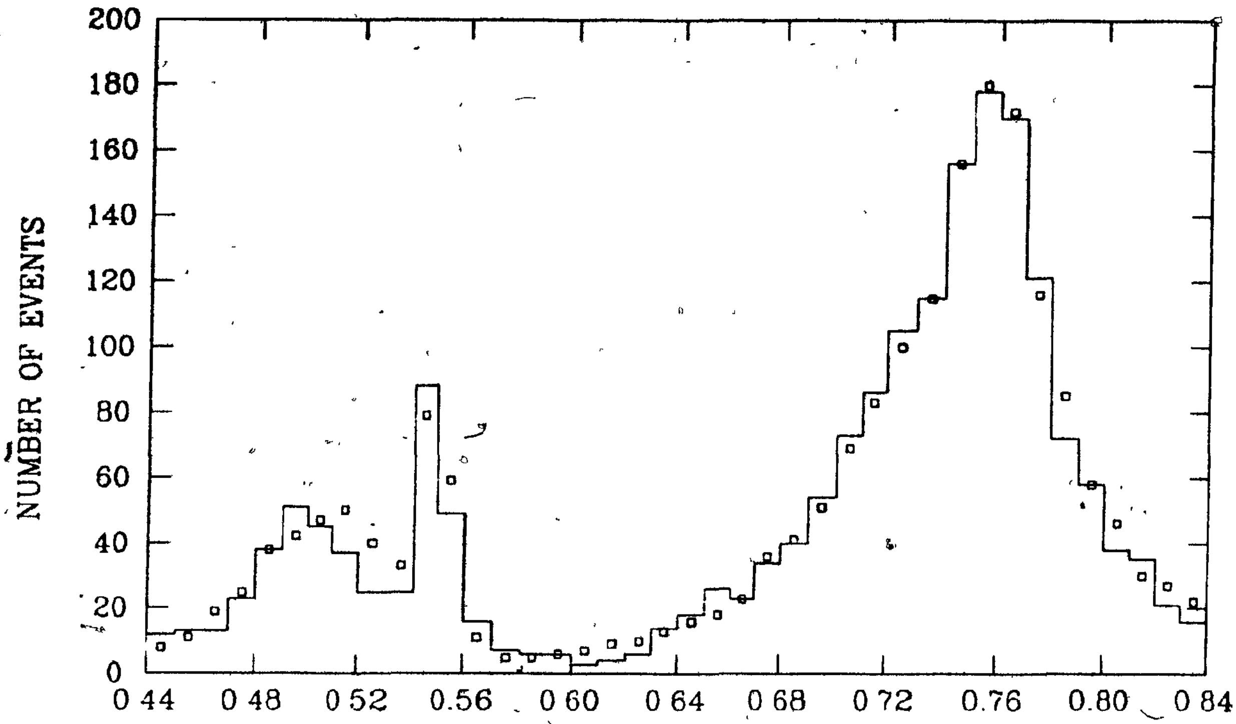

FIG.5-11a.

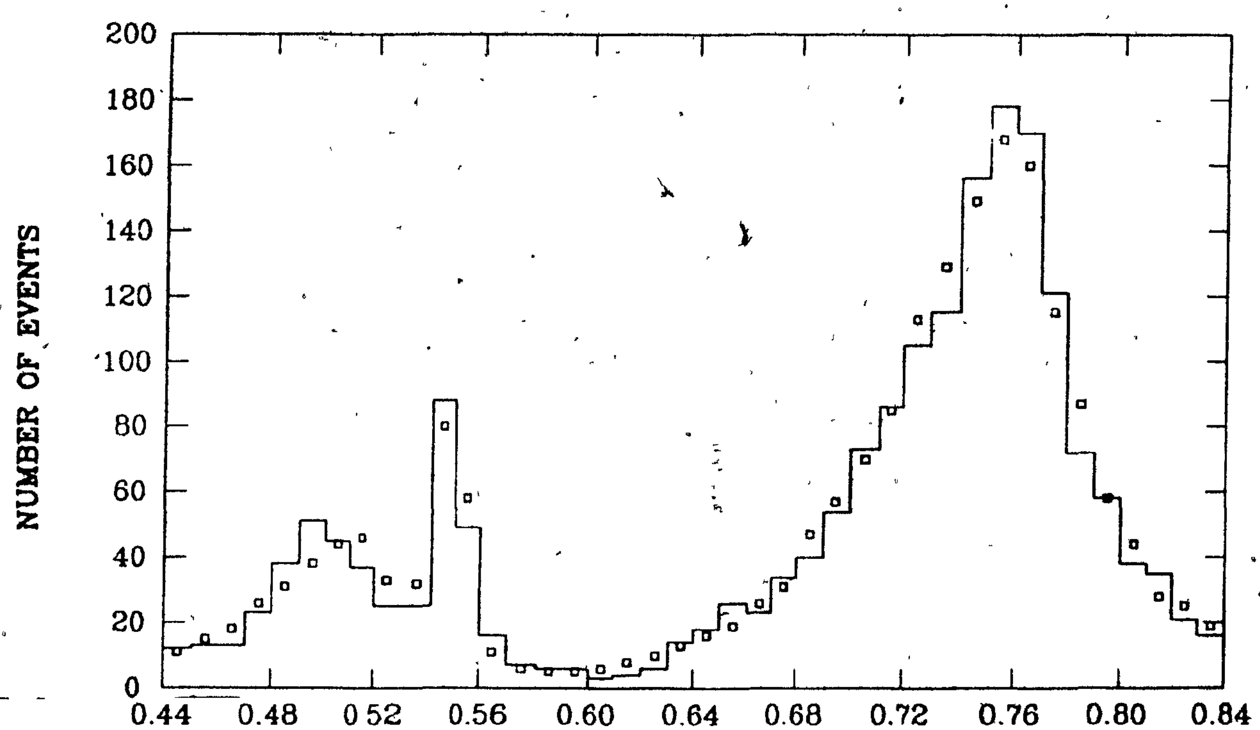

FIG.5-11b.

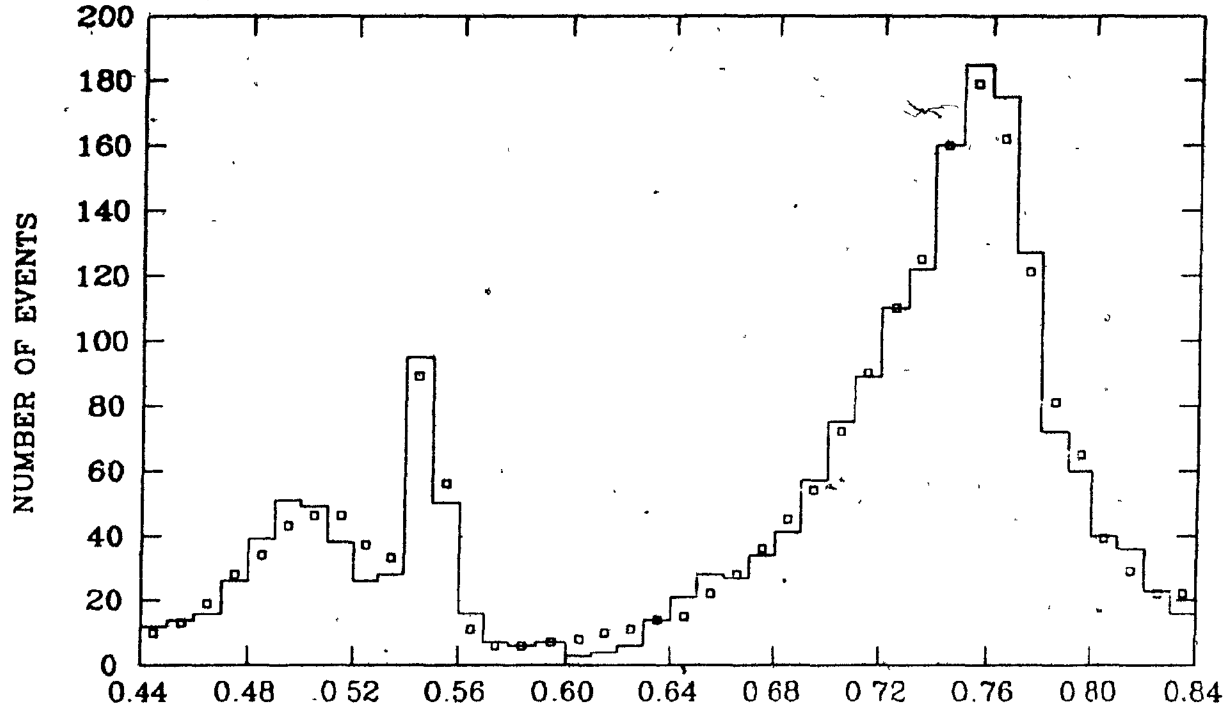

FIG.5-11c.

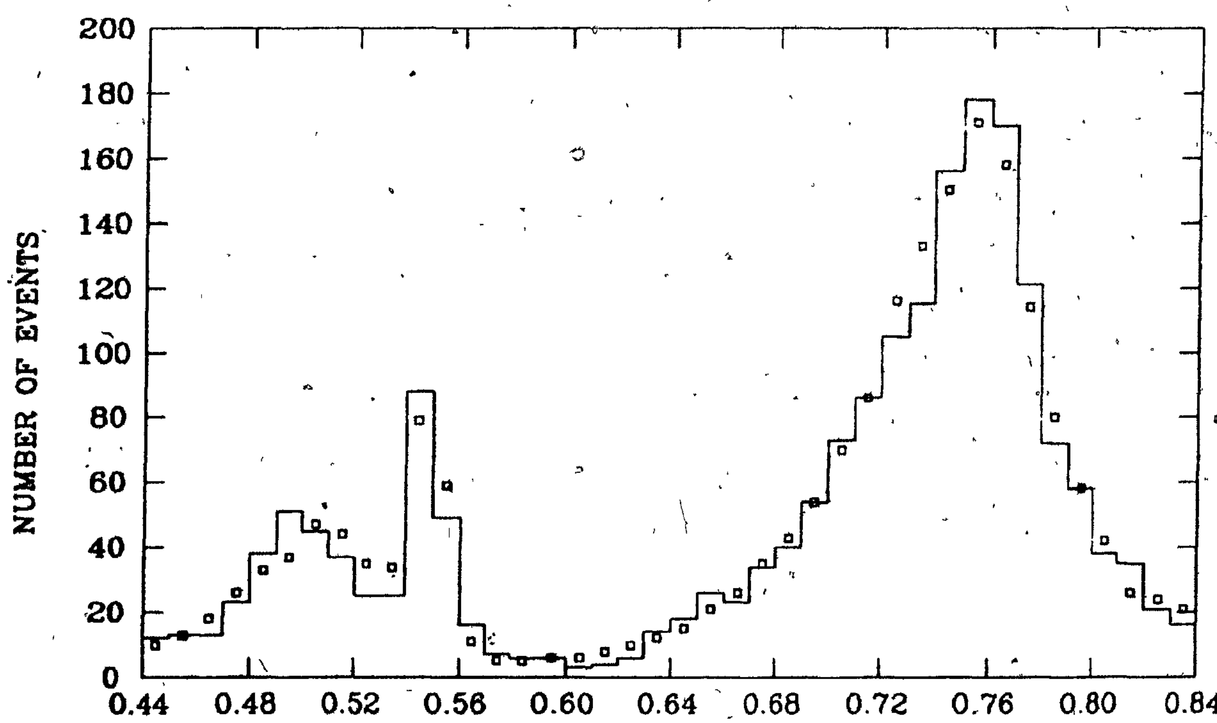

FIG.5-11d.

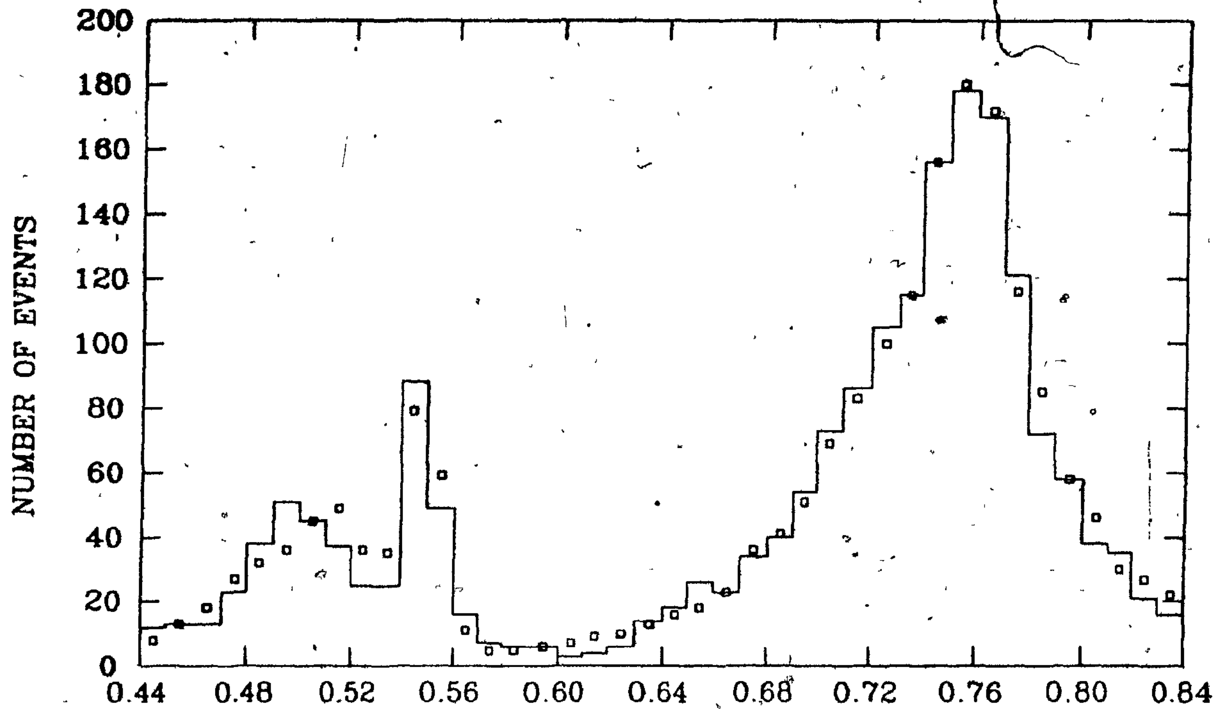

FIG.5−11e.

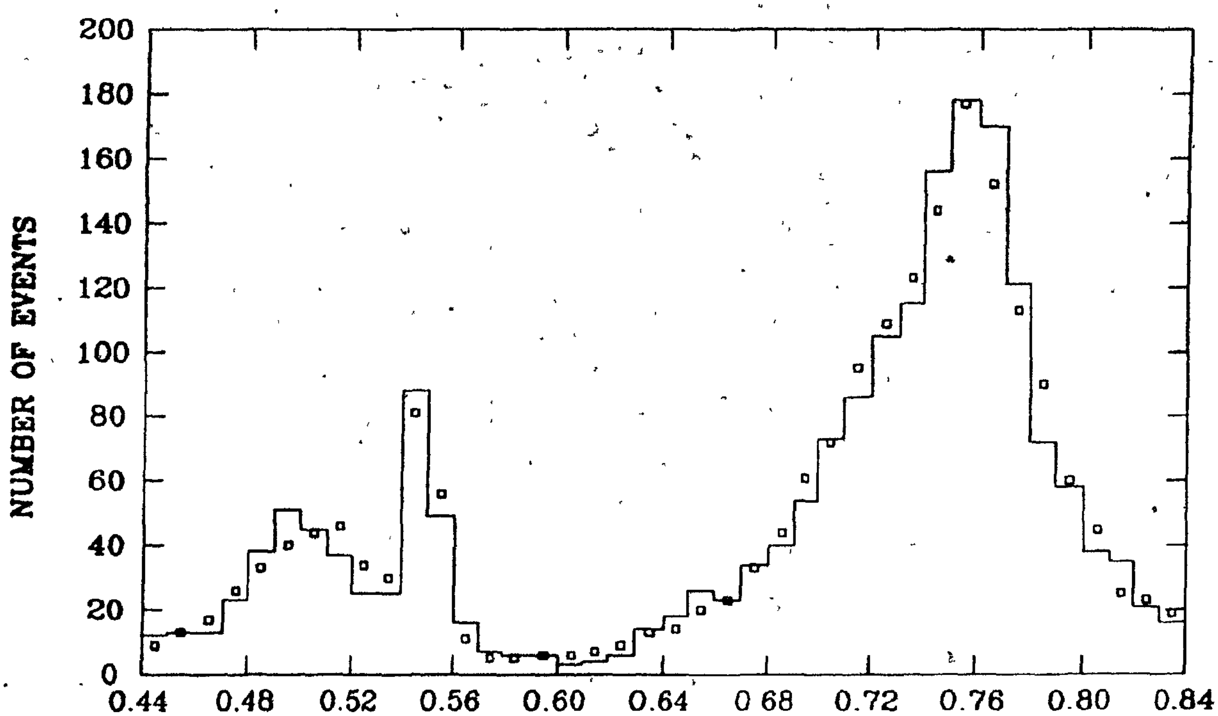

FIG.5−11f.

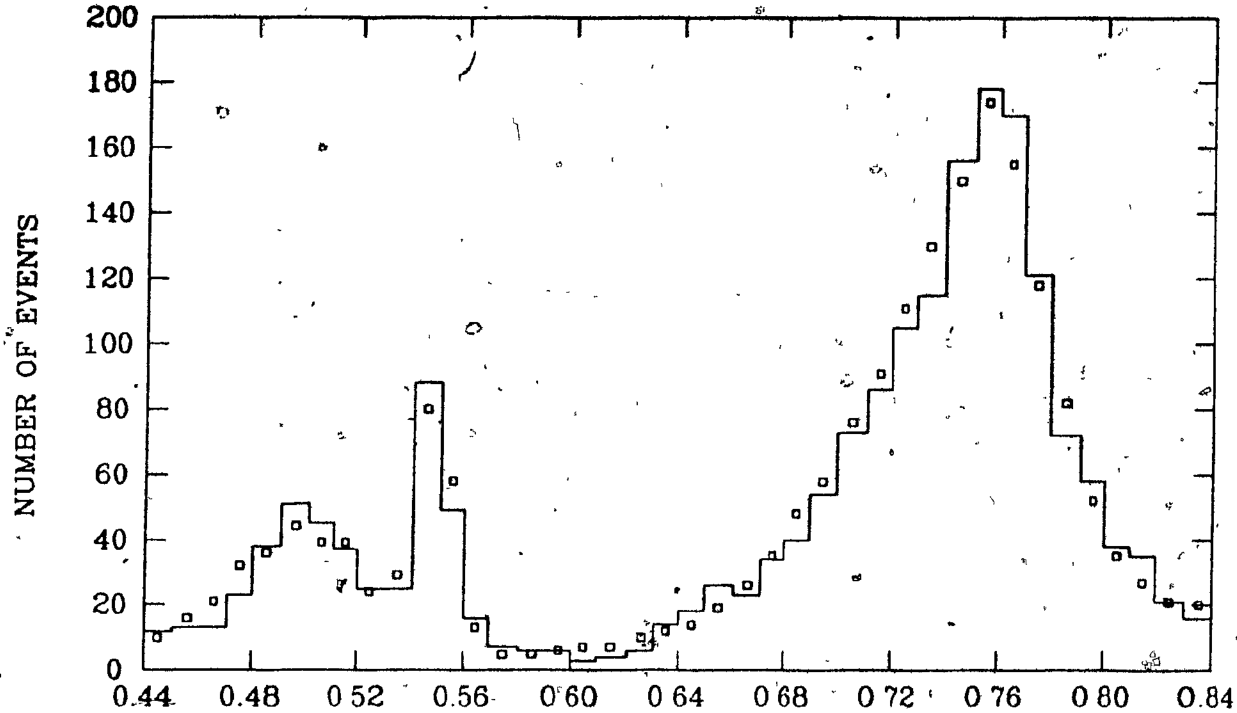

FIG.5–11g.

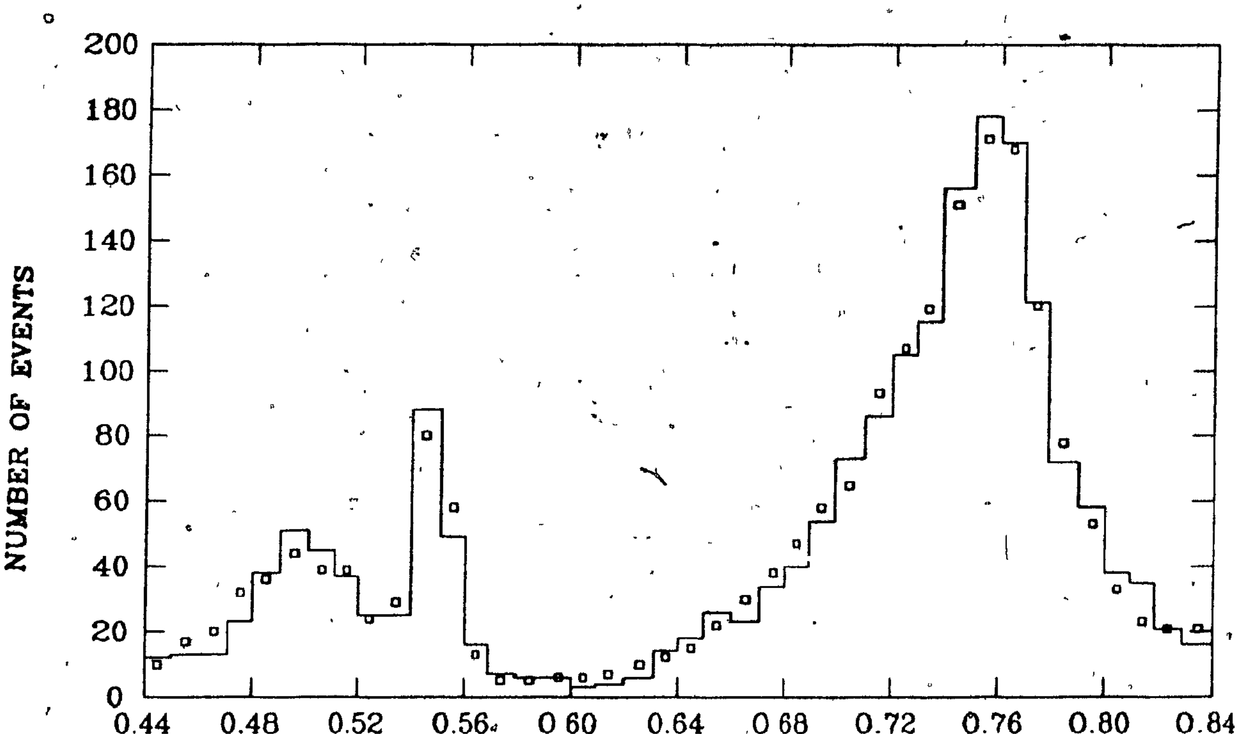

FhG.5–11h.

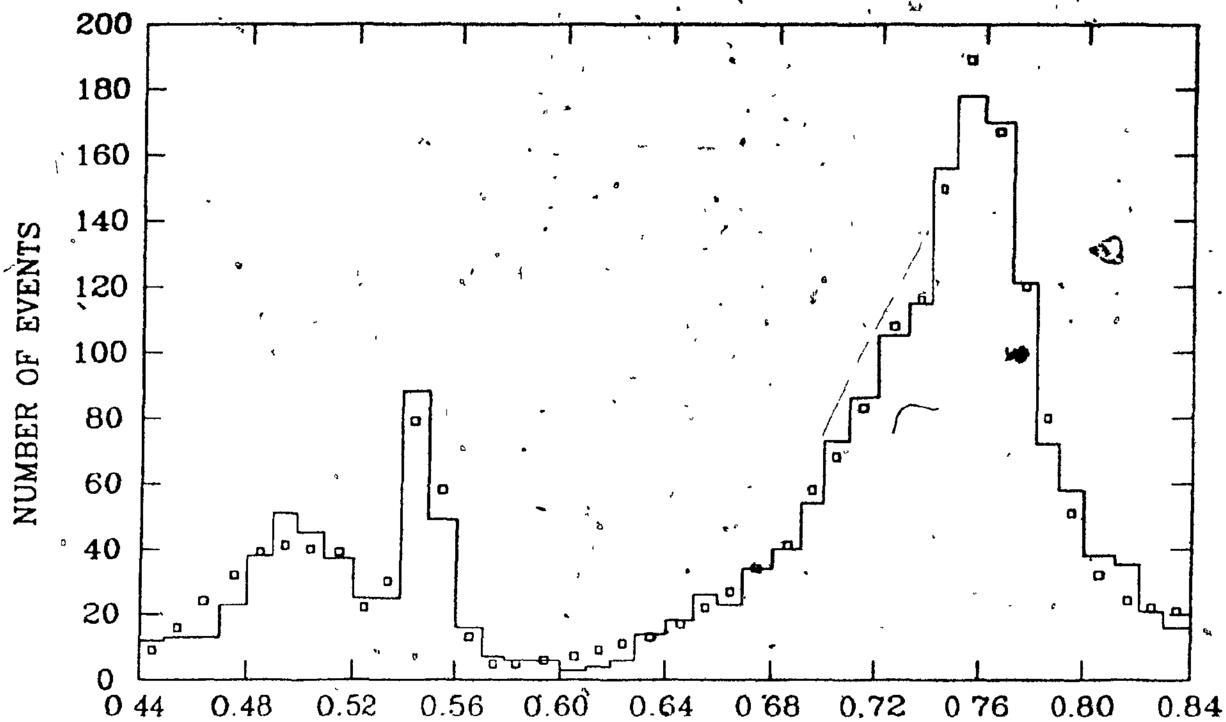

FIG.5−11i.

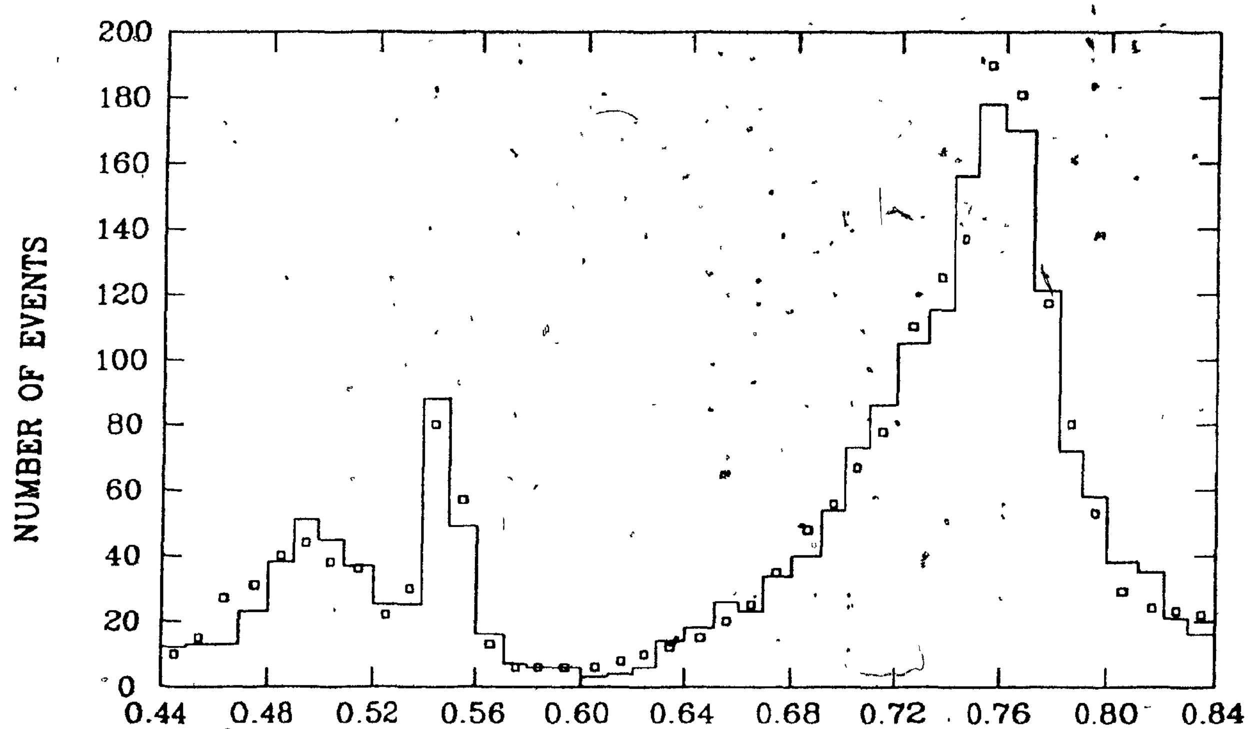

FIG.5−11j.

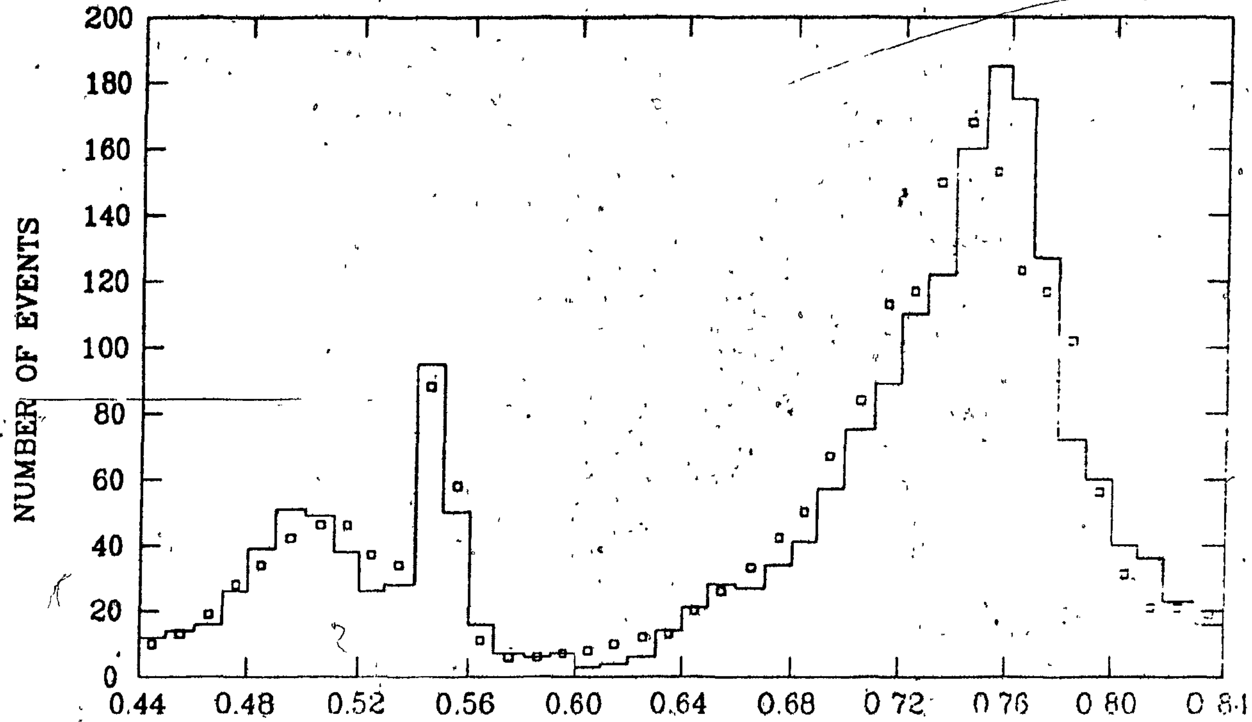

FIG.5–12a.

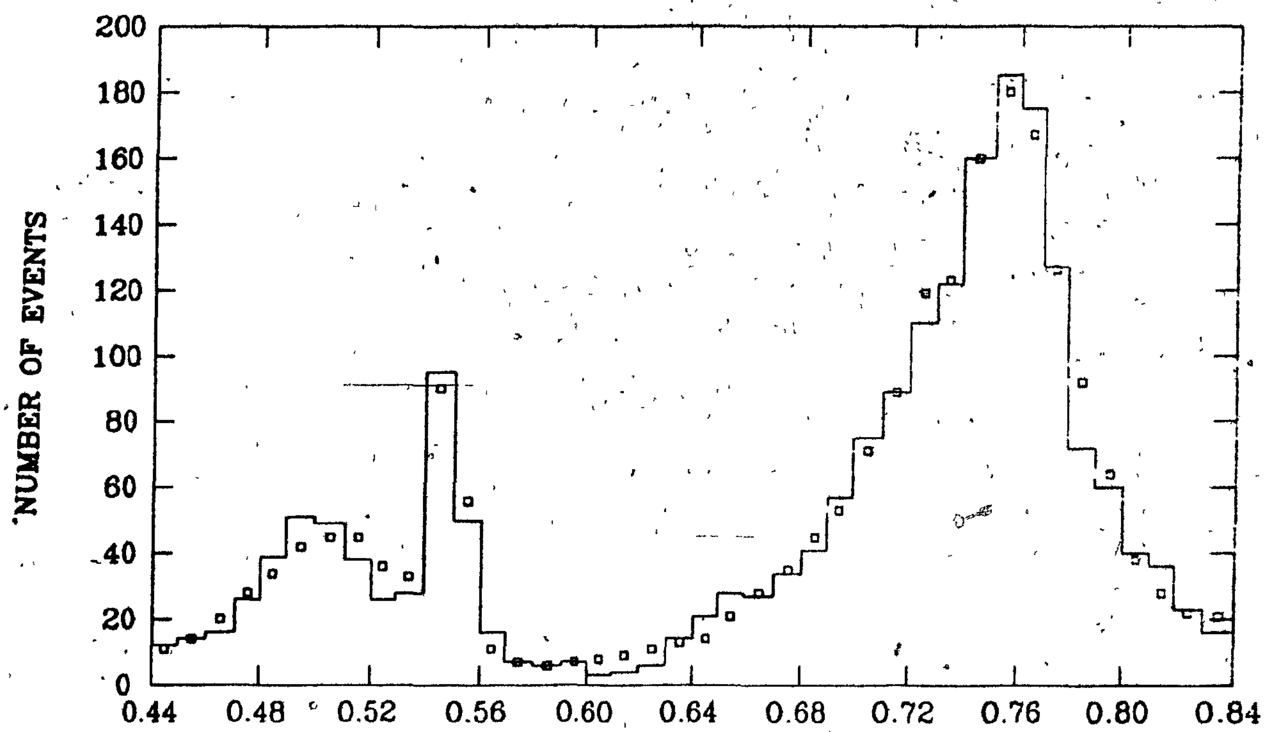

FIG.5–12b.

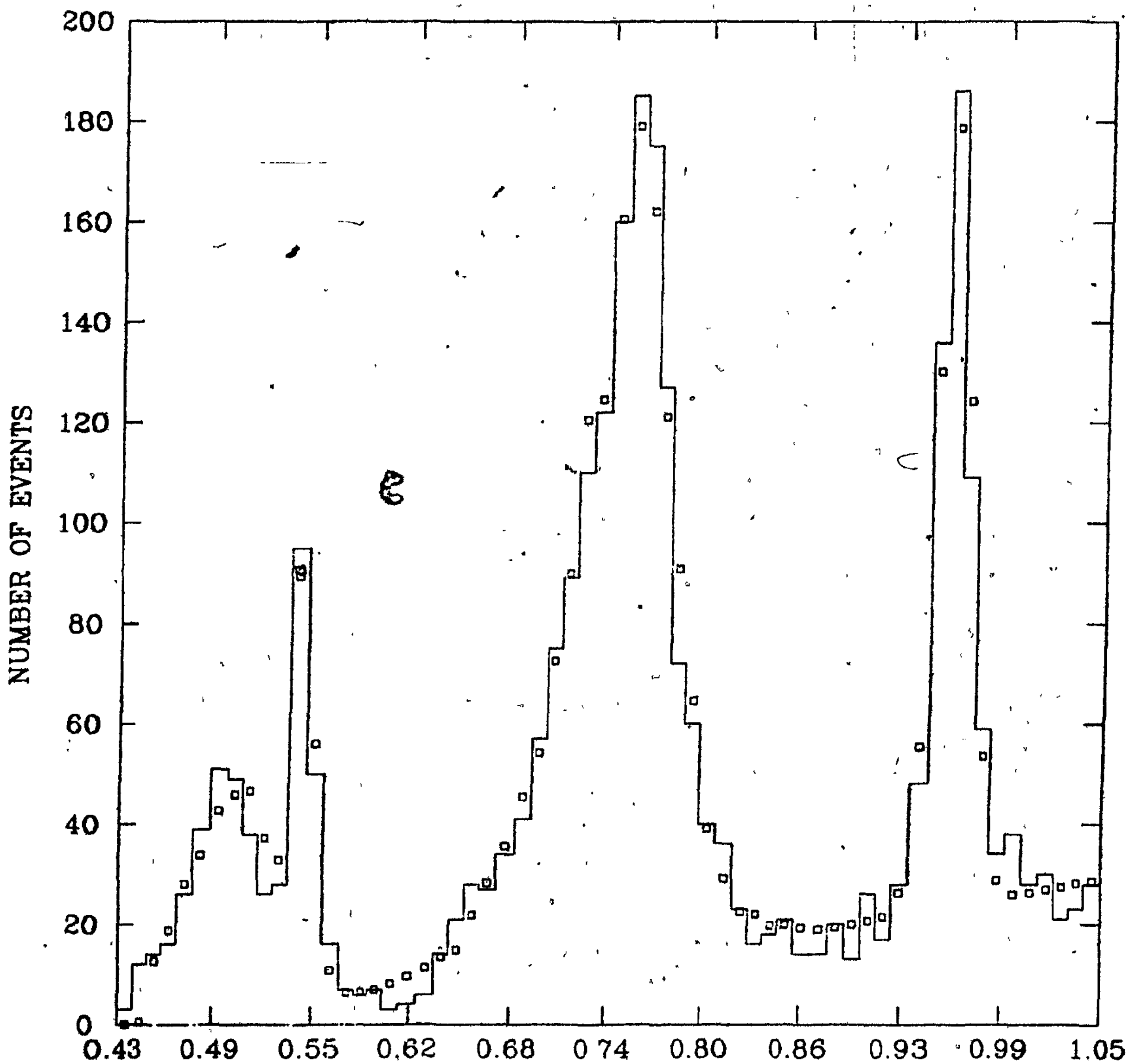

FIG.6-1. Fit to the data $M_{\pi^+\pi^-\gamma}$

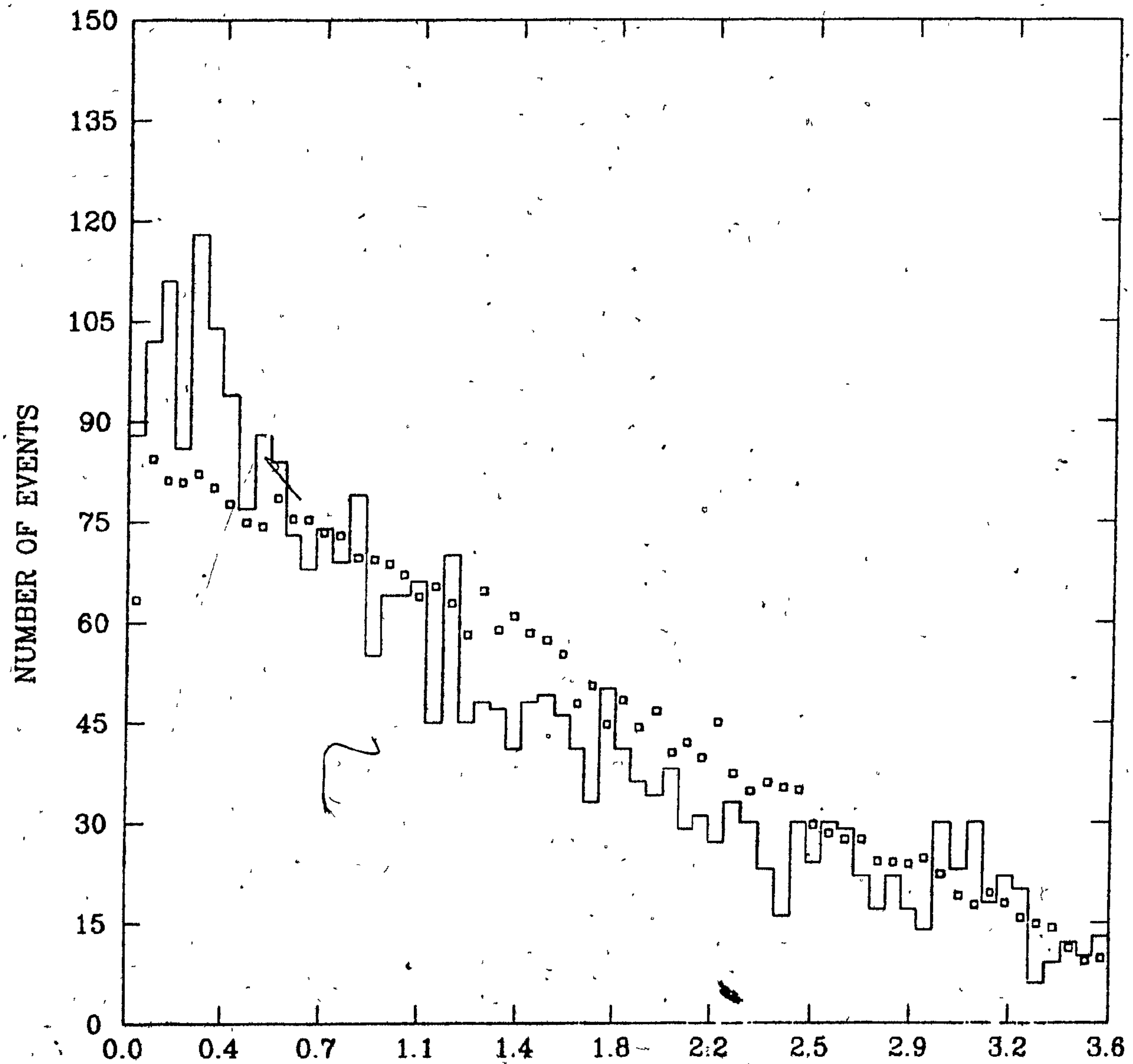

FIG.6-2. Fit to the data E_γ.

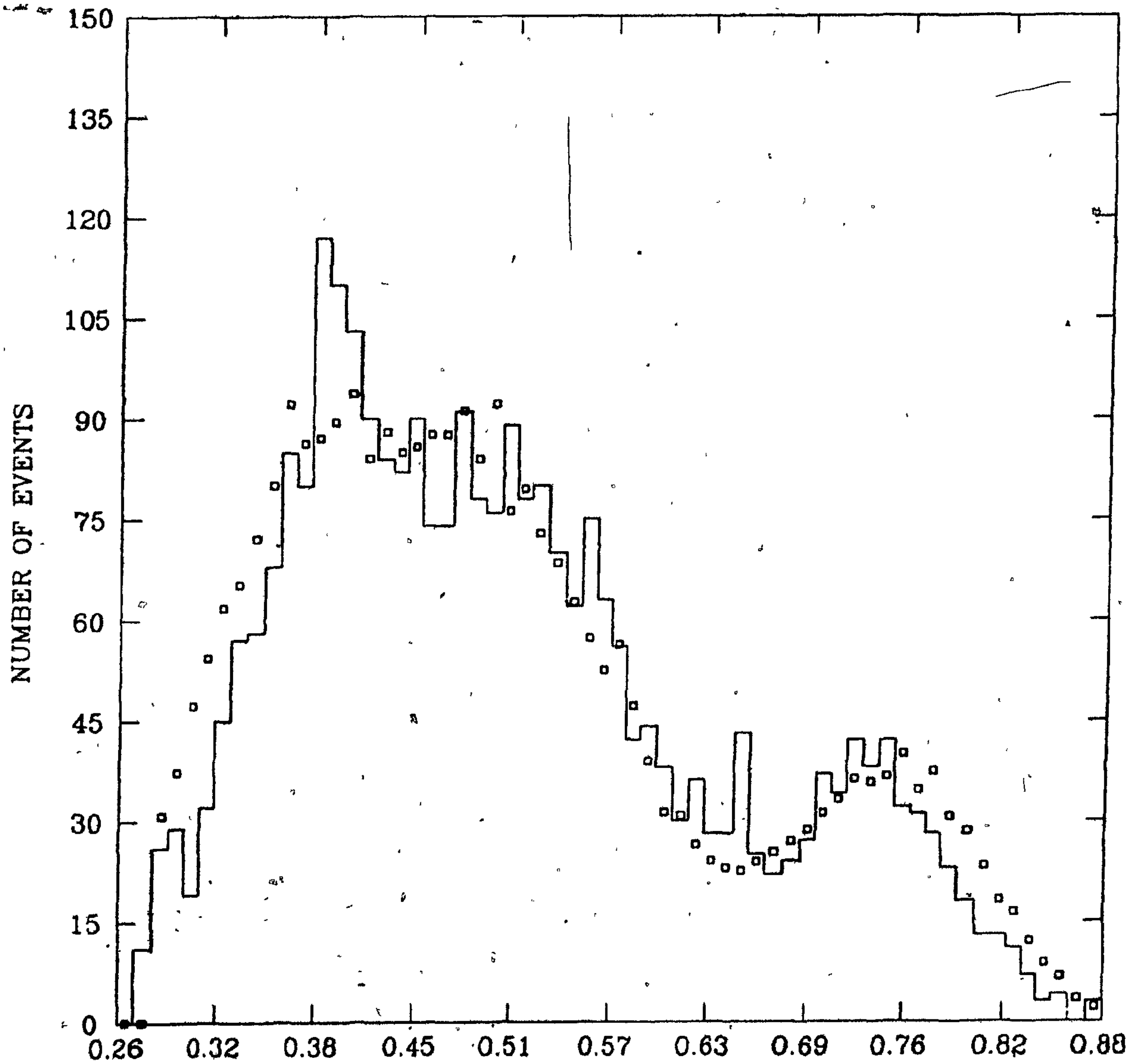

FIG.6-3. Fit to the data $M_{\pi^+\pi^-}$.

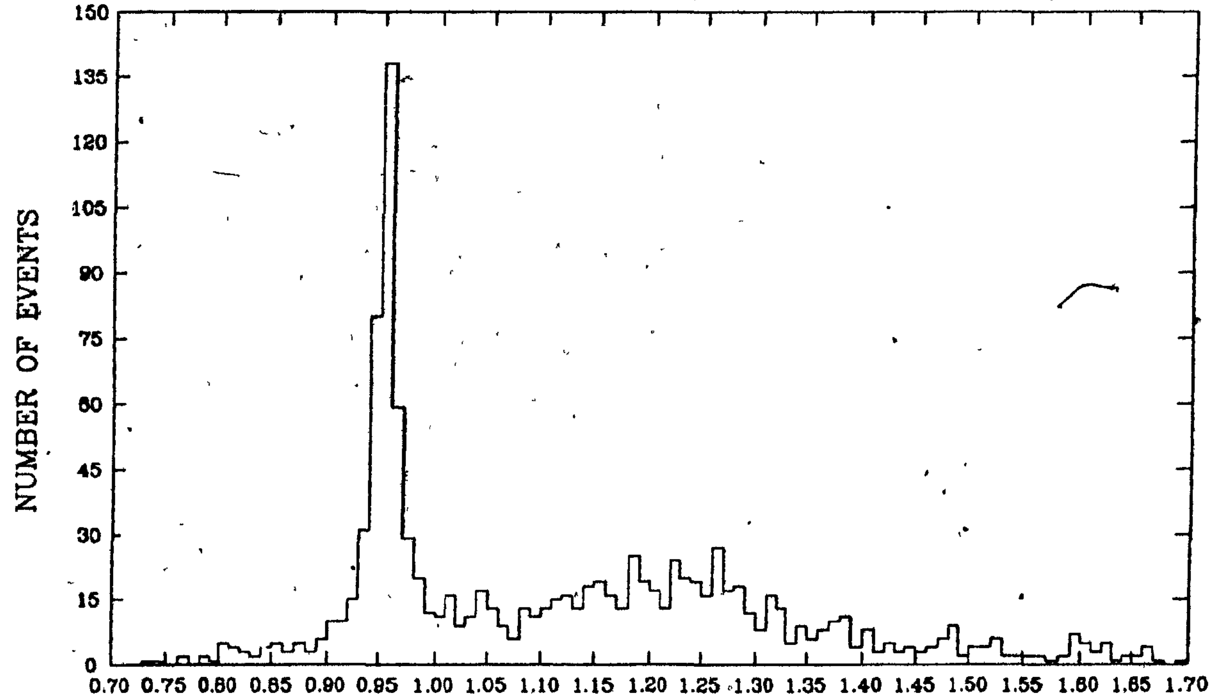

FIG.6–4. $M_{\pi^+\pi^-\gamma}$ with $M_{\pi^+\pi^-}$ in ρ mass region.

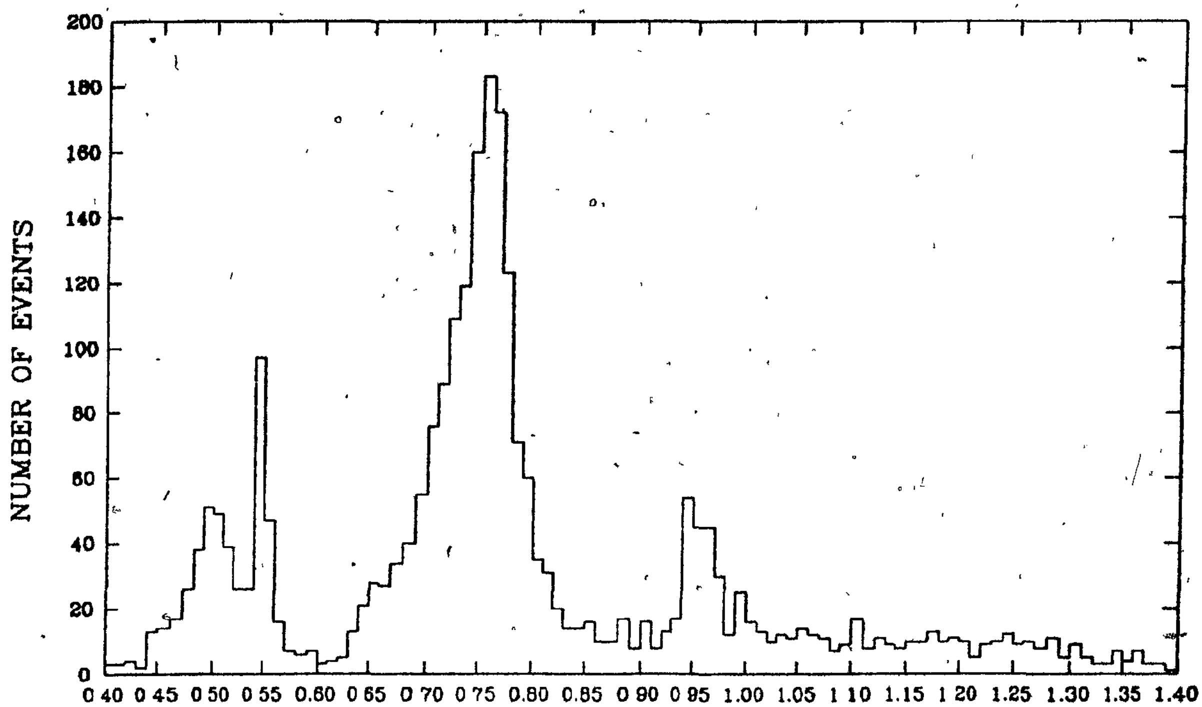

FIG.6–5. $M_{\pi^+\pi^-\gamma}$ with $M_{\pi^+\pi^-}$ out of ρ mass region.

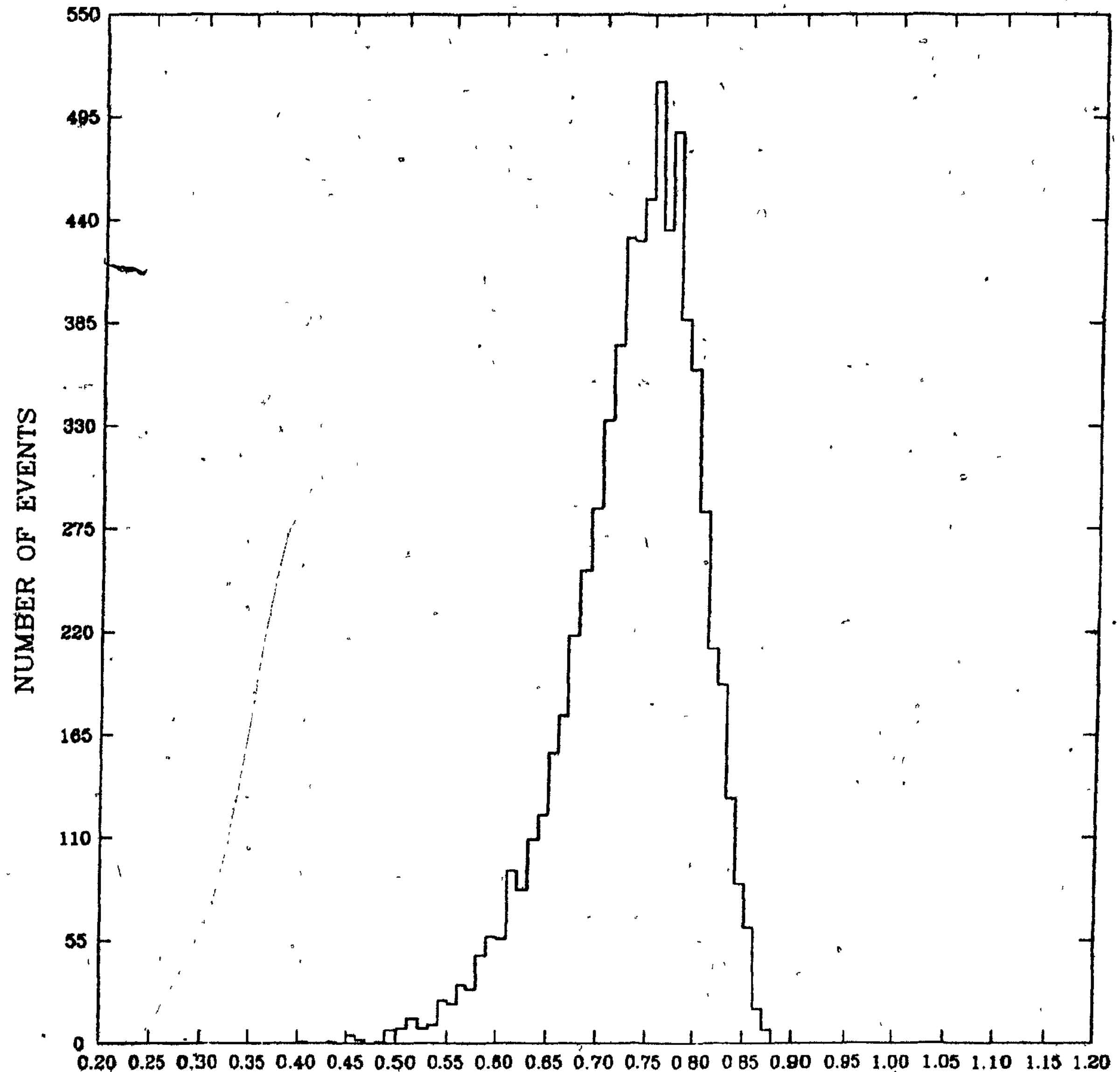

FIG.6-6. P-wave Breit-Wigner for $M_{\pi^+\pi^-}$.

from $\eta' \longrightarrow \rho\gamma$ Monte-Carlo

CHARACTERISTICS:

Cathode Readout

Operational Voltage: 5.1 - 5.8 kV

Spatial Resolution: 1 wire/mm, 16 strips (see below)

Maximum Frequency: 5 MHz

Magic Gas: 0.5% freon-13 B1 (CF_3Br)

24.5% isobutane (iso C_4H_{10})

75.0% argon

READOUT AND SUMMING CIRCUITRY:

TTL Logic

Input Voltage: 5 - 40 mV

Output Voltage: NIM

Clusters sizes @ 1 wire/mm

59 wires	40	35	30	25	20	15	10	10	15	20	25	30	35	40	59 wires

FIGURE 7-1 Proportional Wire Chamber

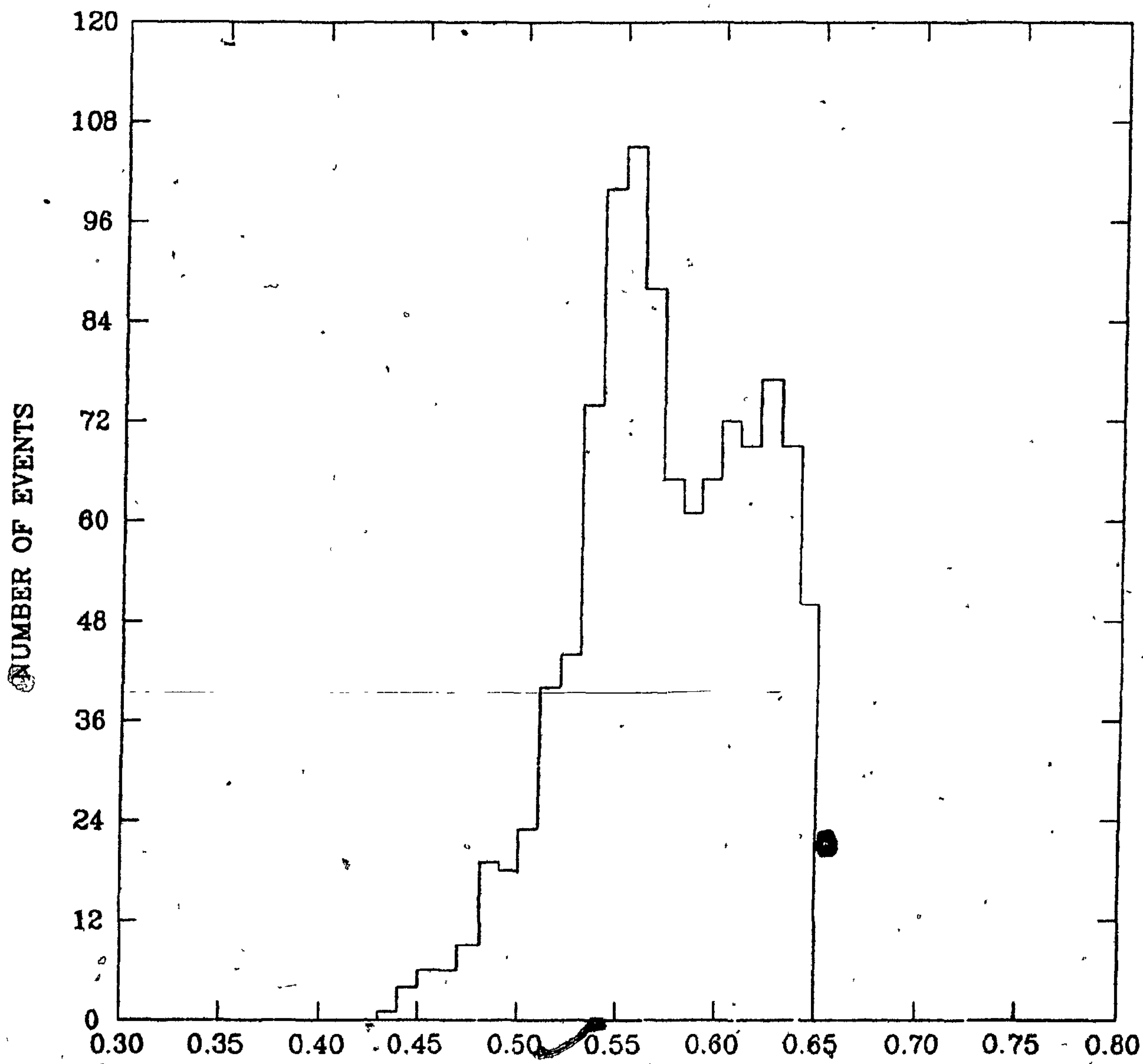

FIG.7–2. $M_{\pi^+\pi^-\pi^0}$ 1C fit for the 3_γ data.

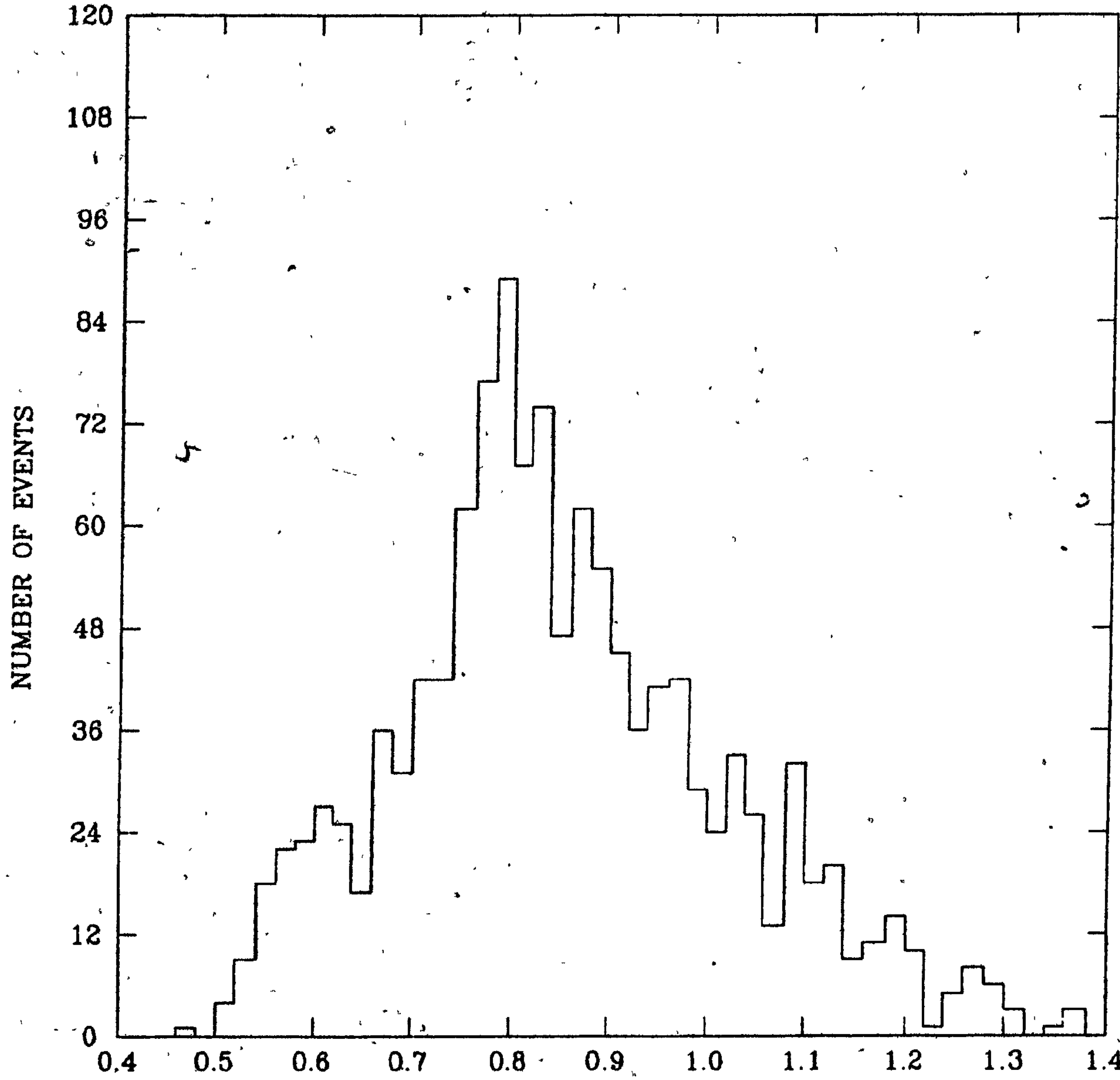

FIG.7–3. $M_{\pi^+\pi^-\pi^o\gamma}$ unfitted.

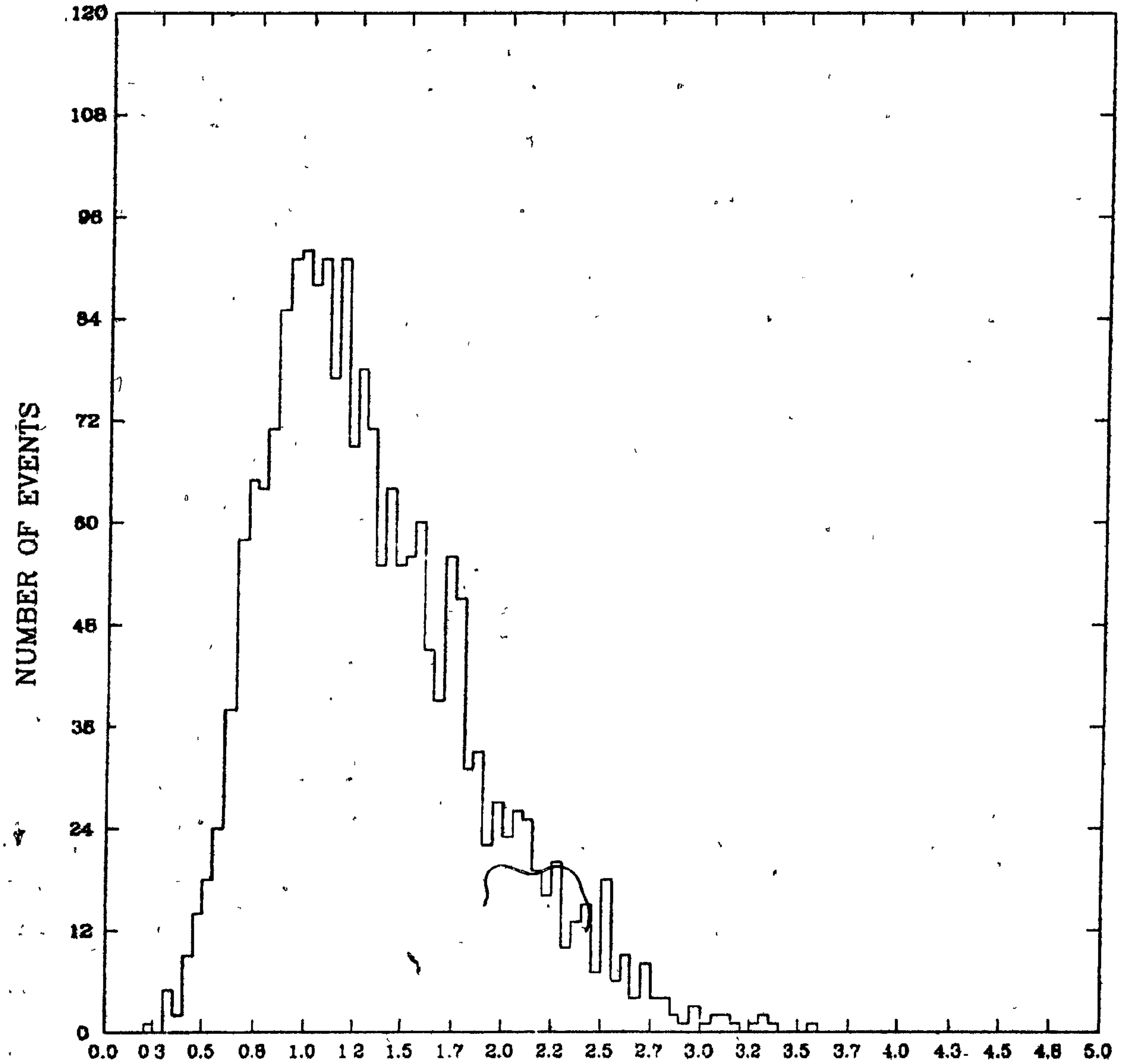

FIG 7–4. E_{γ_1} from $\rho \dashrightarrow \eta\gamma$ Monte-Carlo.

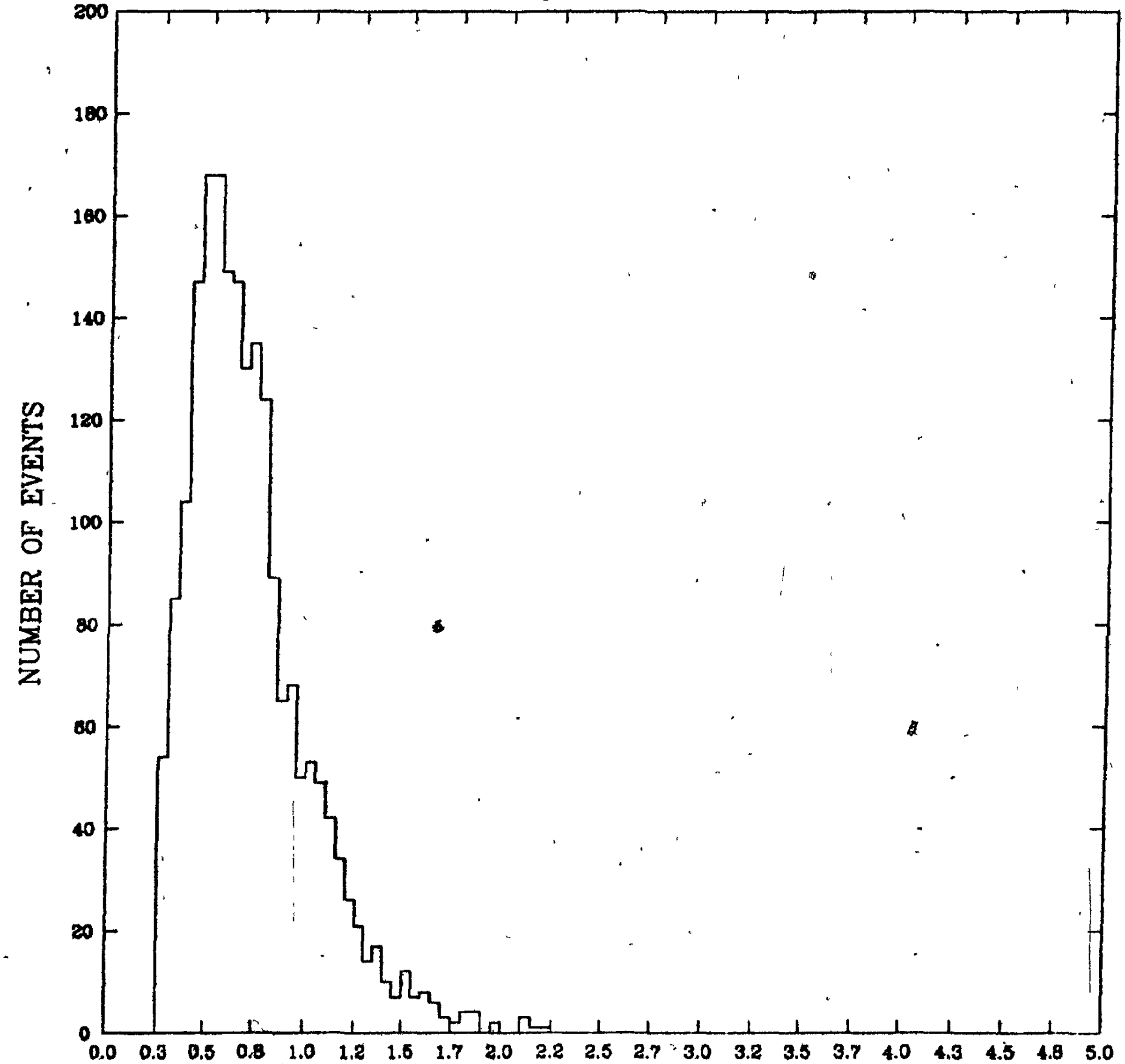

FIG.7–5. E_{γ_2} from $\rho \dashrightarrow \eta\gamma$ Monte-Carlo.

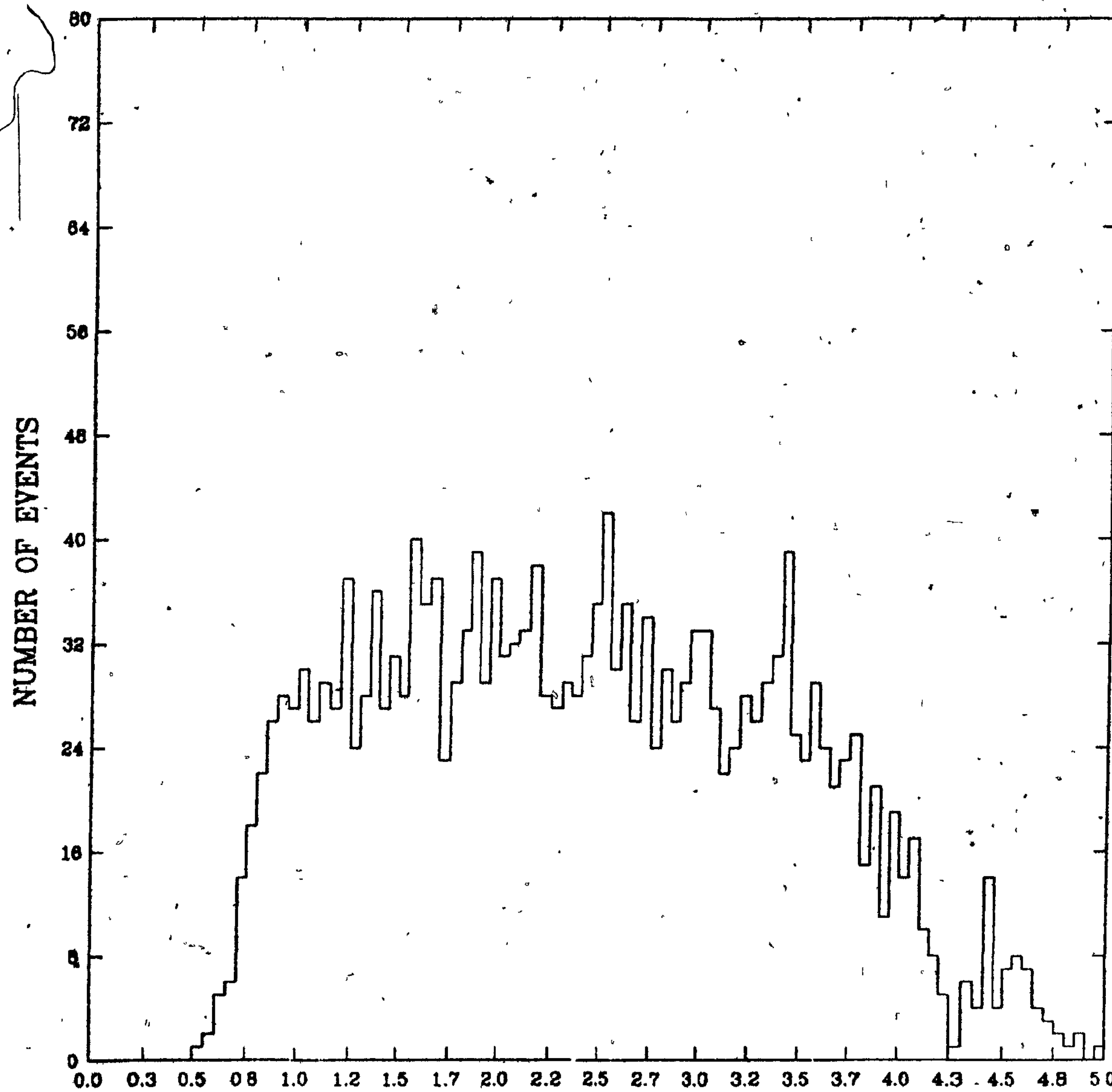

FIG.7-6 E_{γ_3} from $\rho \dashrightarrow \eta\gamma$ Monte-Carlo.

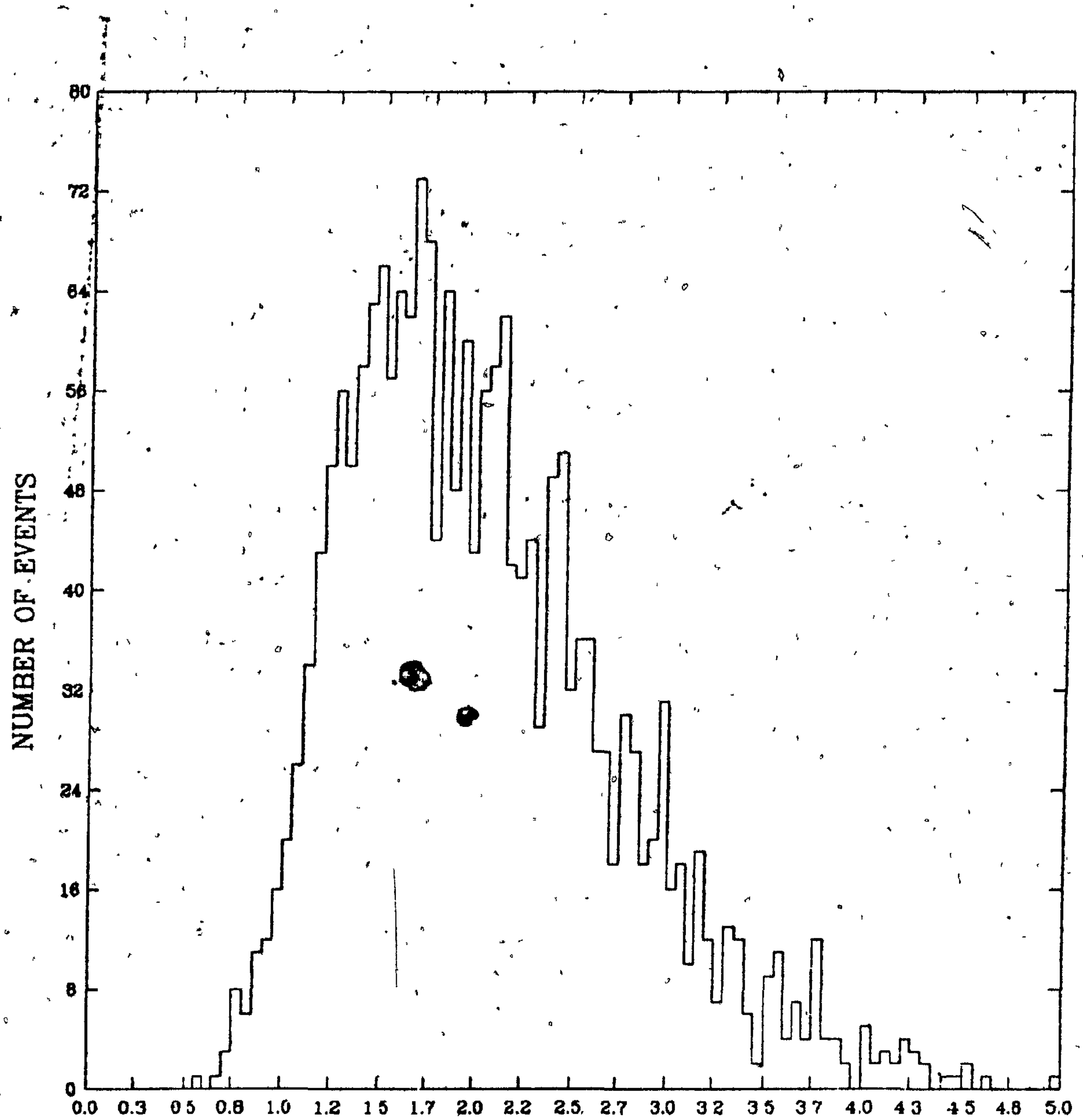

FIG 7-7. $E_{\gamma_1\gamma_2}$ from $\rho \dashrightarrow \eta\gamma$ Monte-Carlo.

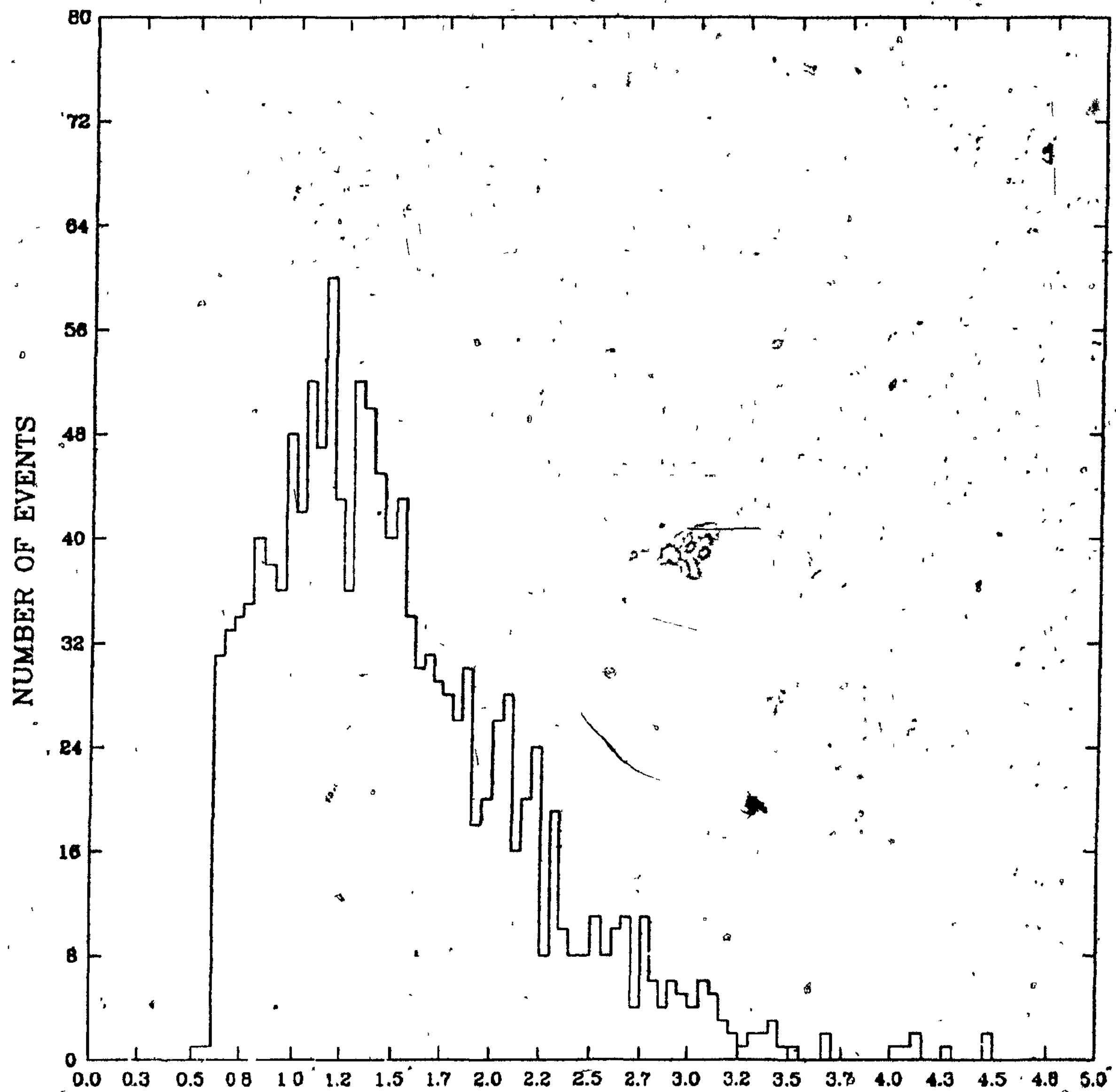

FIG.7-8. E_{γ_1} for the 3γ data.

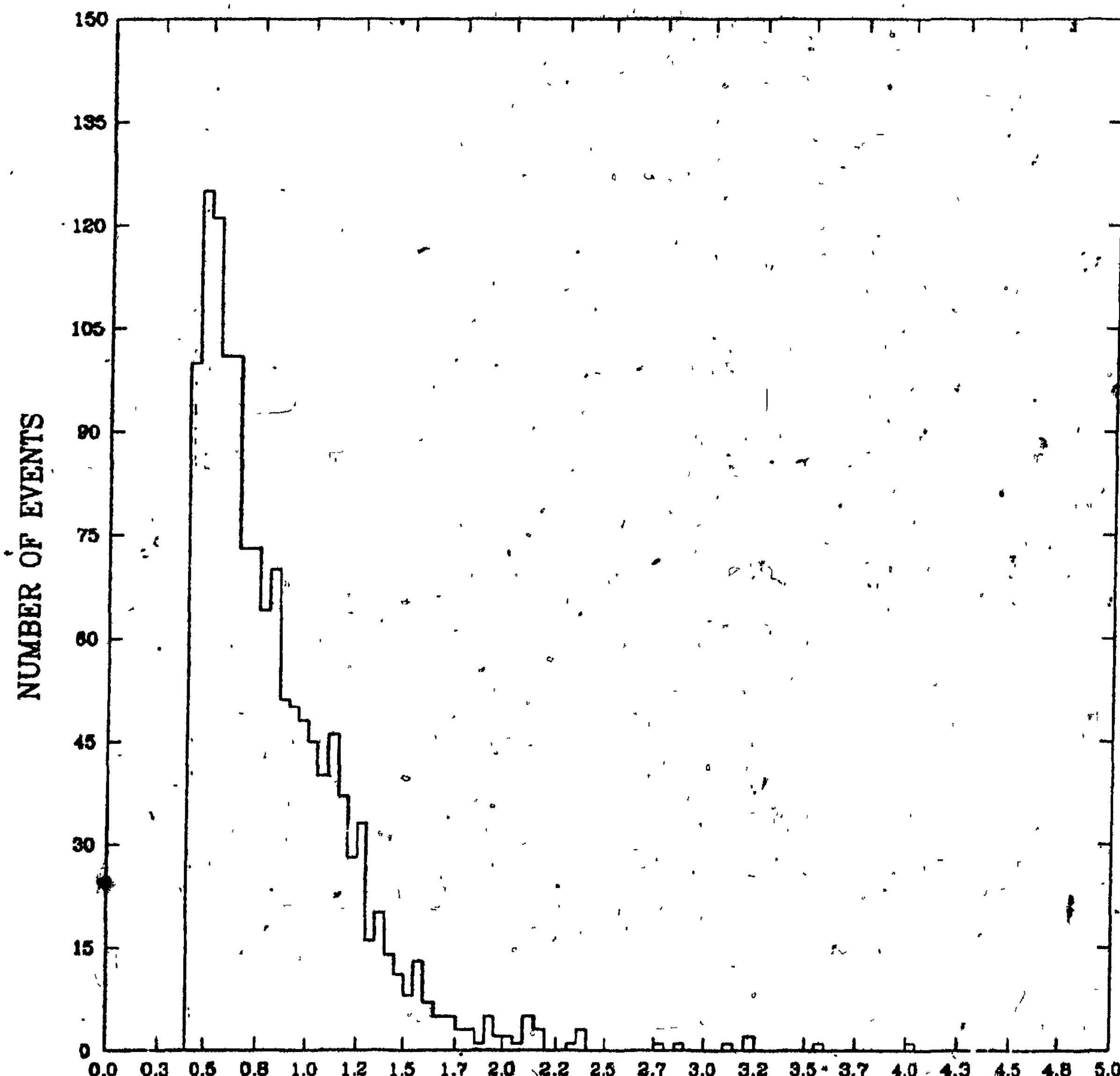

FIG.7–9. E_{γ_2} for the 3γ data.

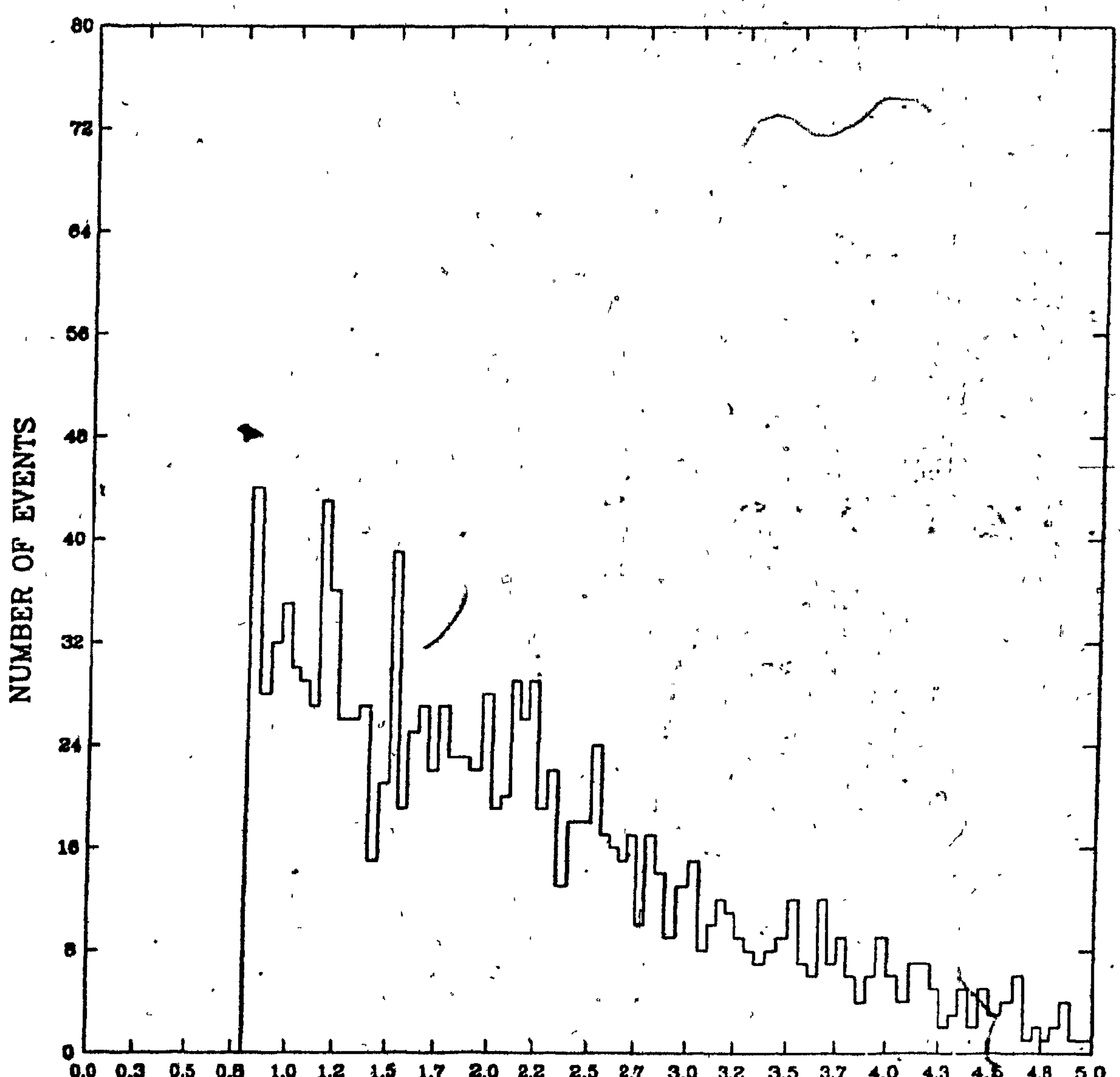

FIG.7–10. E_{γ_3} for the 3γ data.

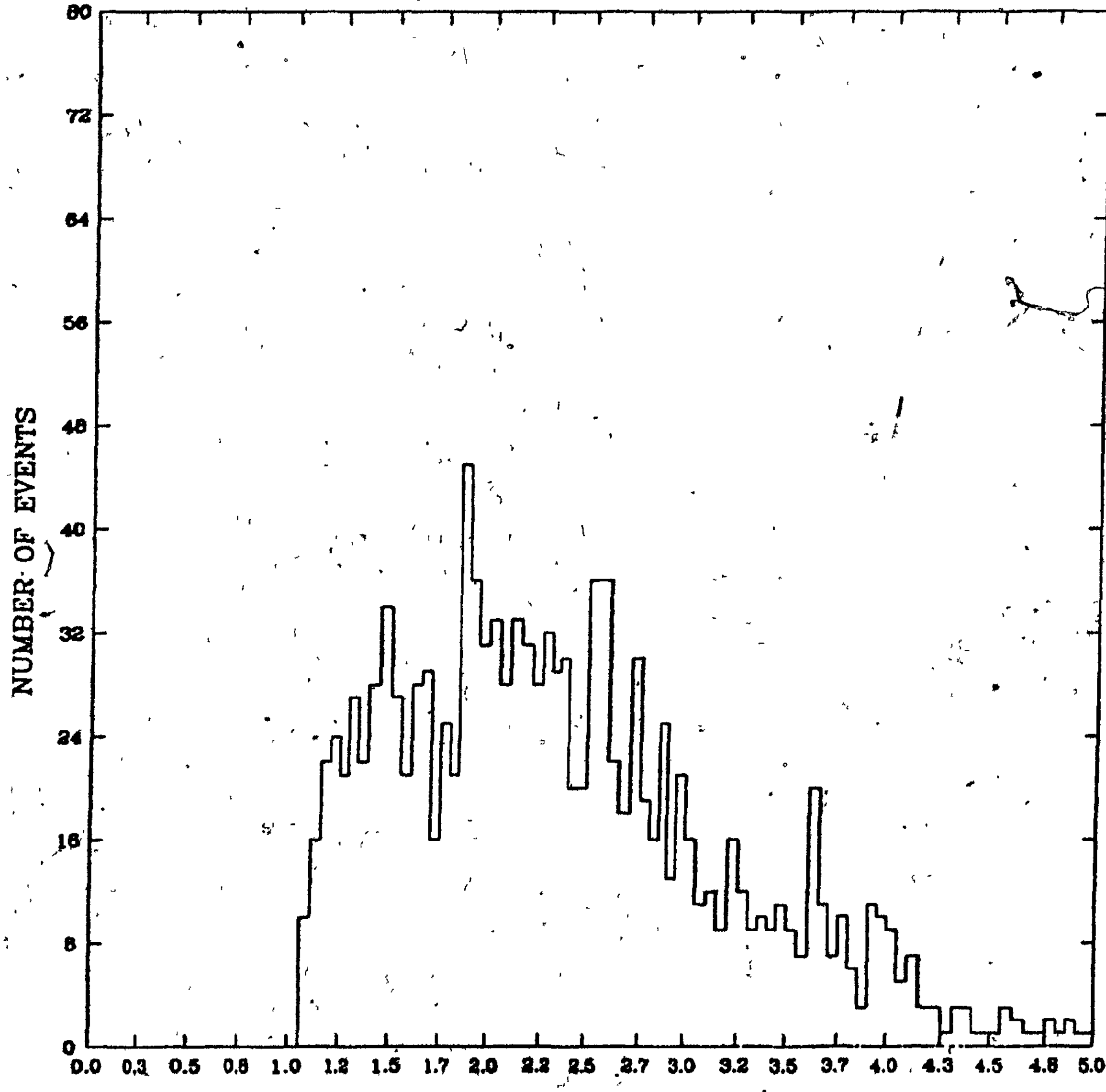

FIG.7−11. $E_{\gamma_1\gamma_2}$ for the 3_γ data.

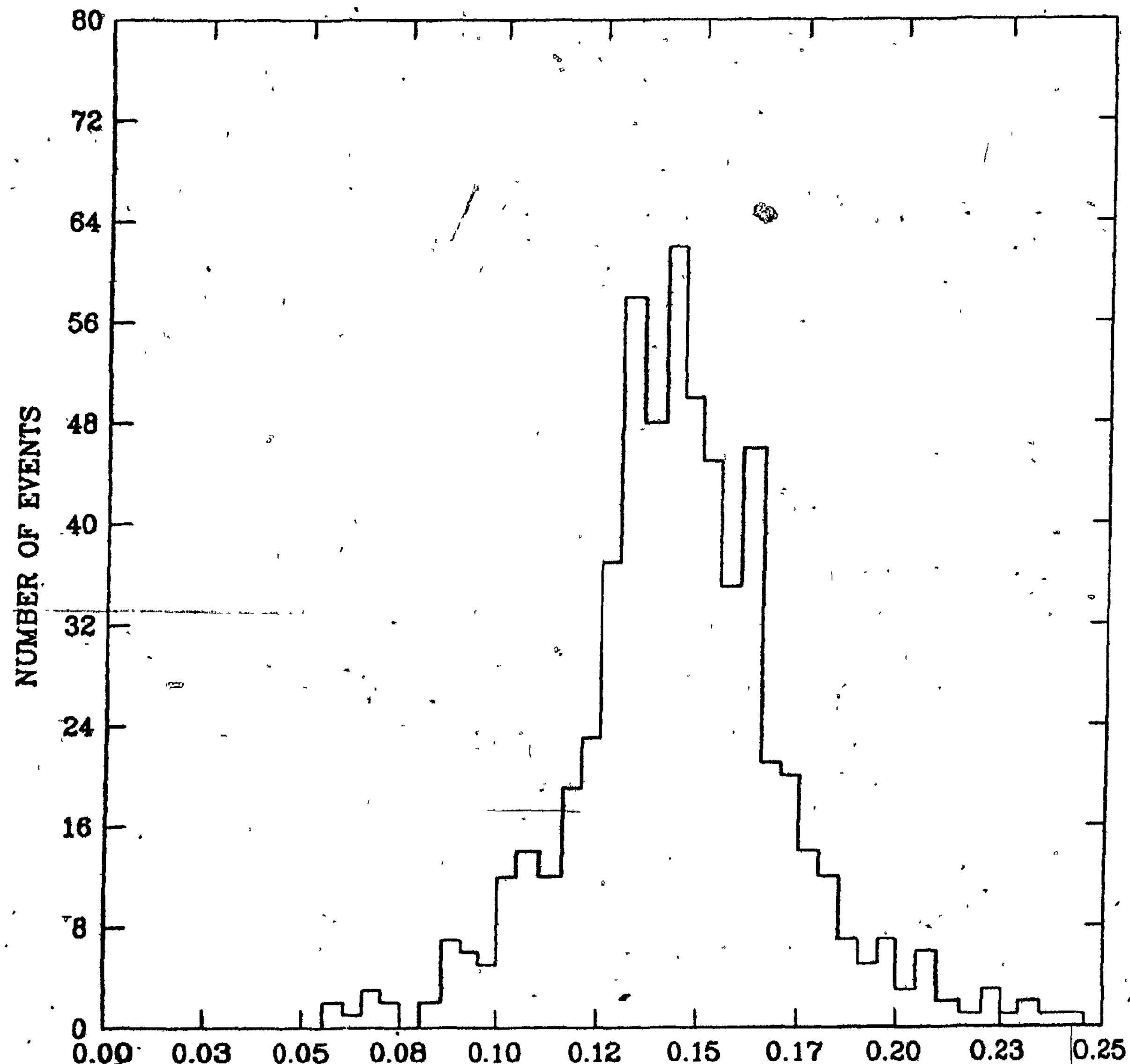

FIG.7-12: $M_{\gamma_1\gamma_2}$ for the 3γ data. $M_{\pi^+\pi^-\pi^0} < .6$ Gev.

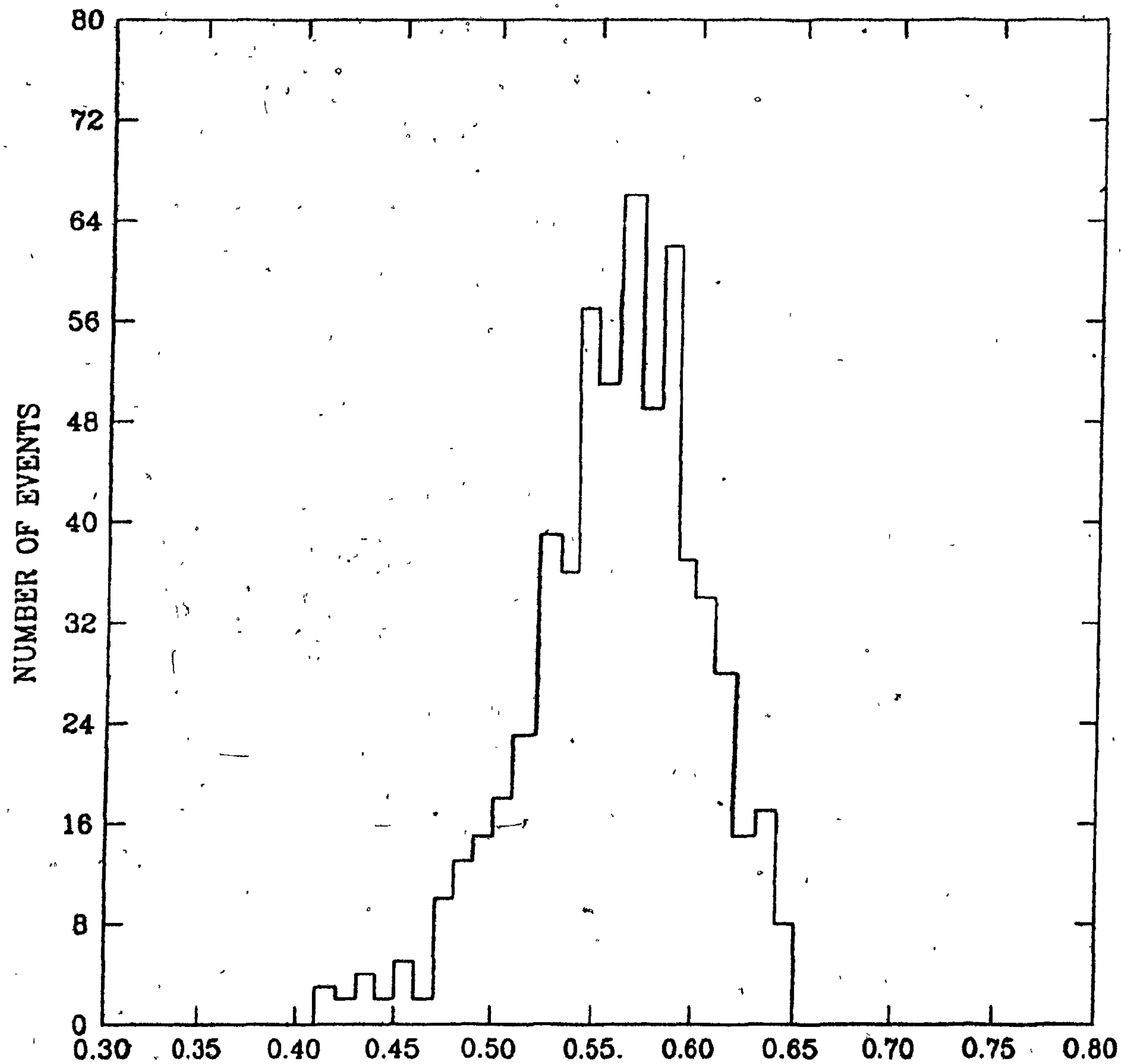

FIG.7–13. $M_{\pi^+\pi^-\pi^0}$ with E_γ cuts.

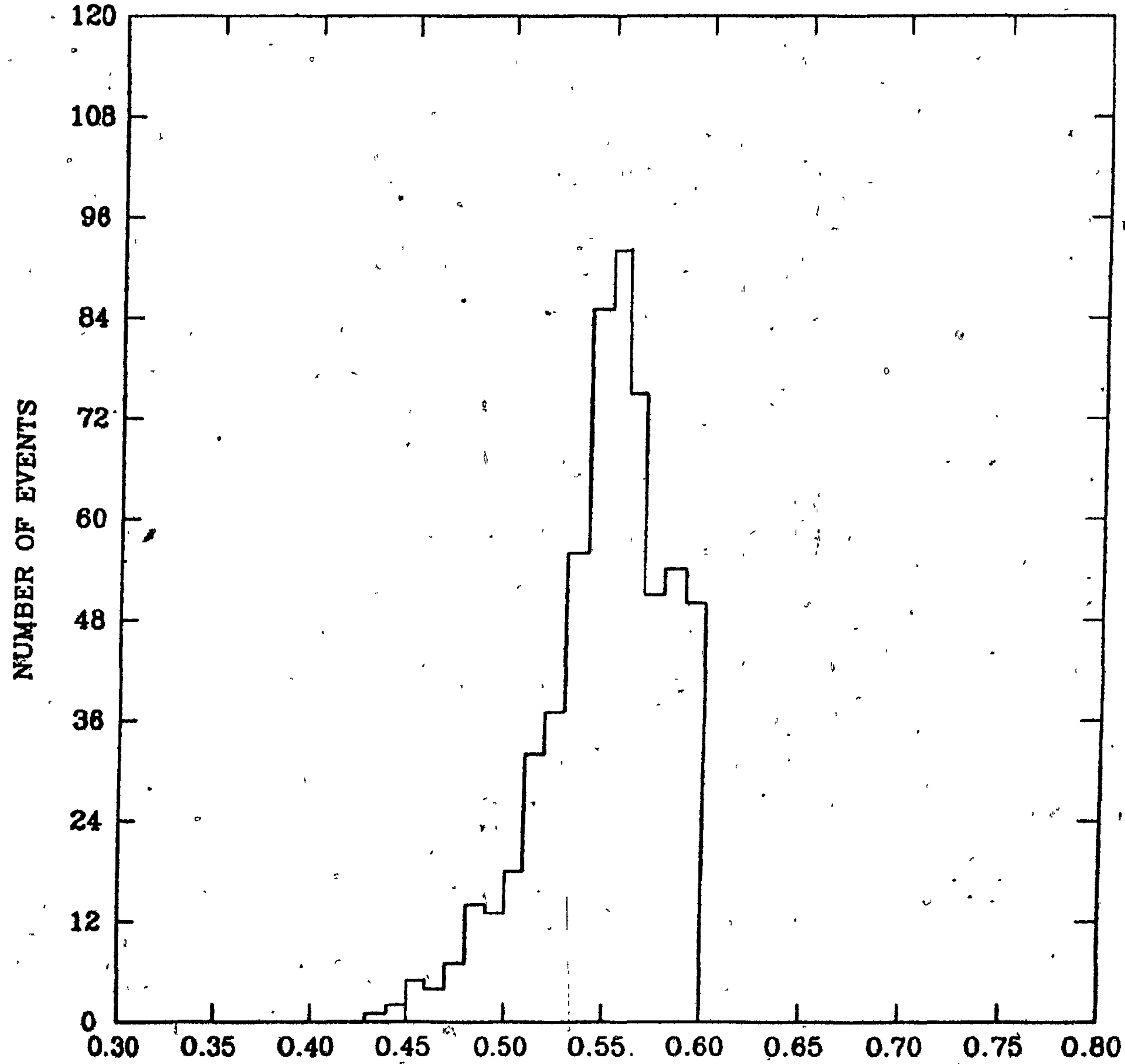

FIG.7−14. $M_{\pi^+\pi^-\pi^0}$ 1C fit with E_γ cuts.

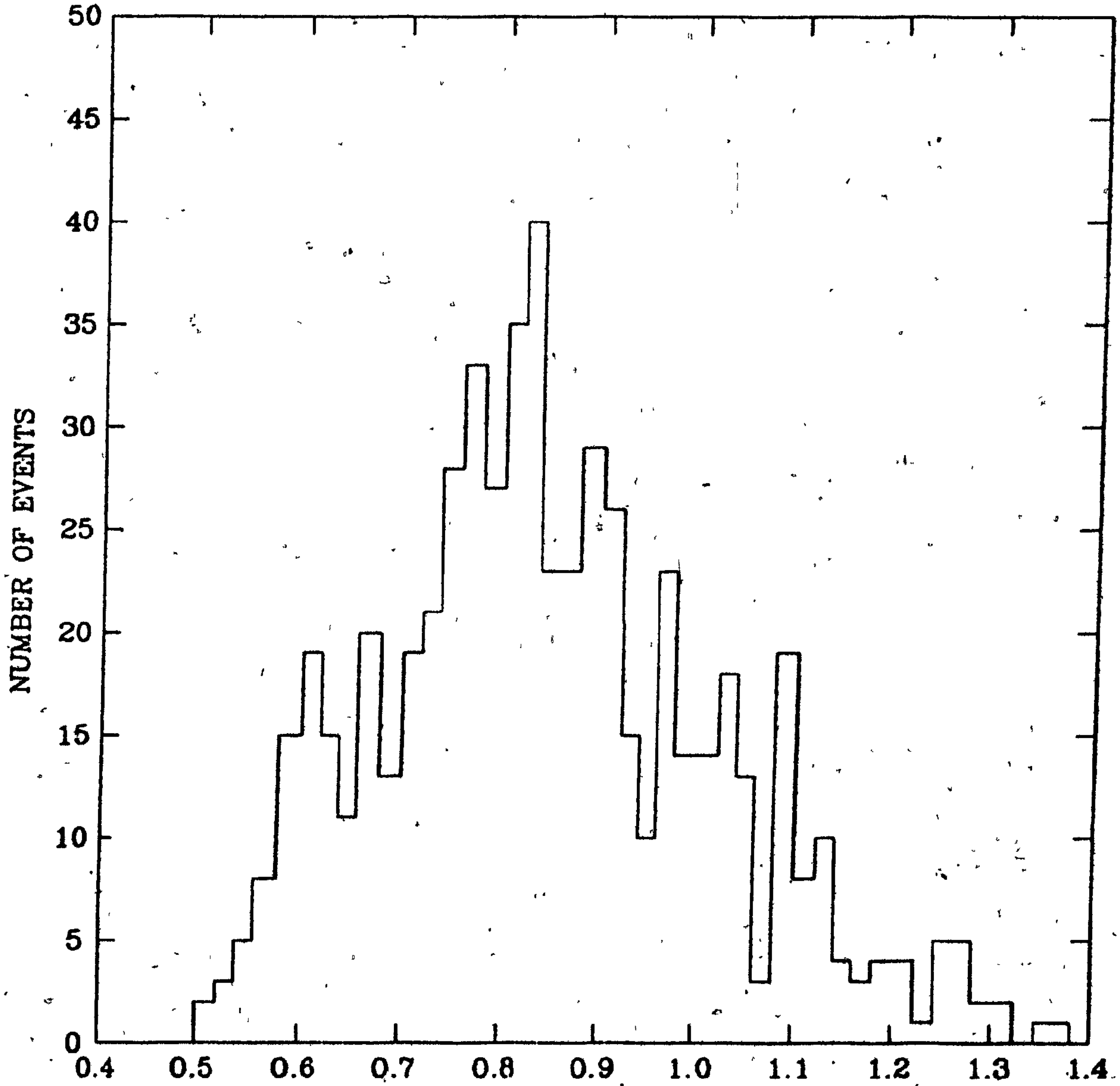

FIG.7−15. $M_{\eta\gamma}$ with E_{γ} cuts. $M_{\pi^+\pi^-\pi^0} < .60$ Gev.

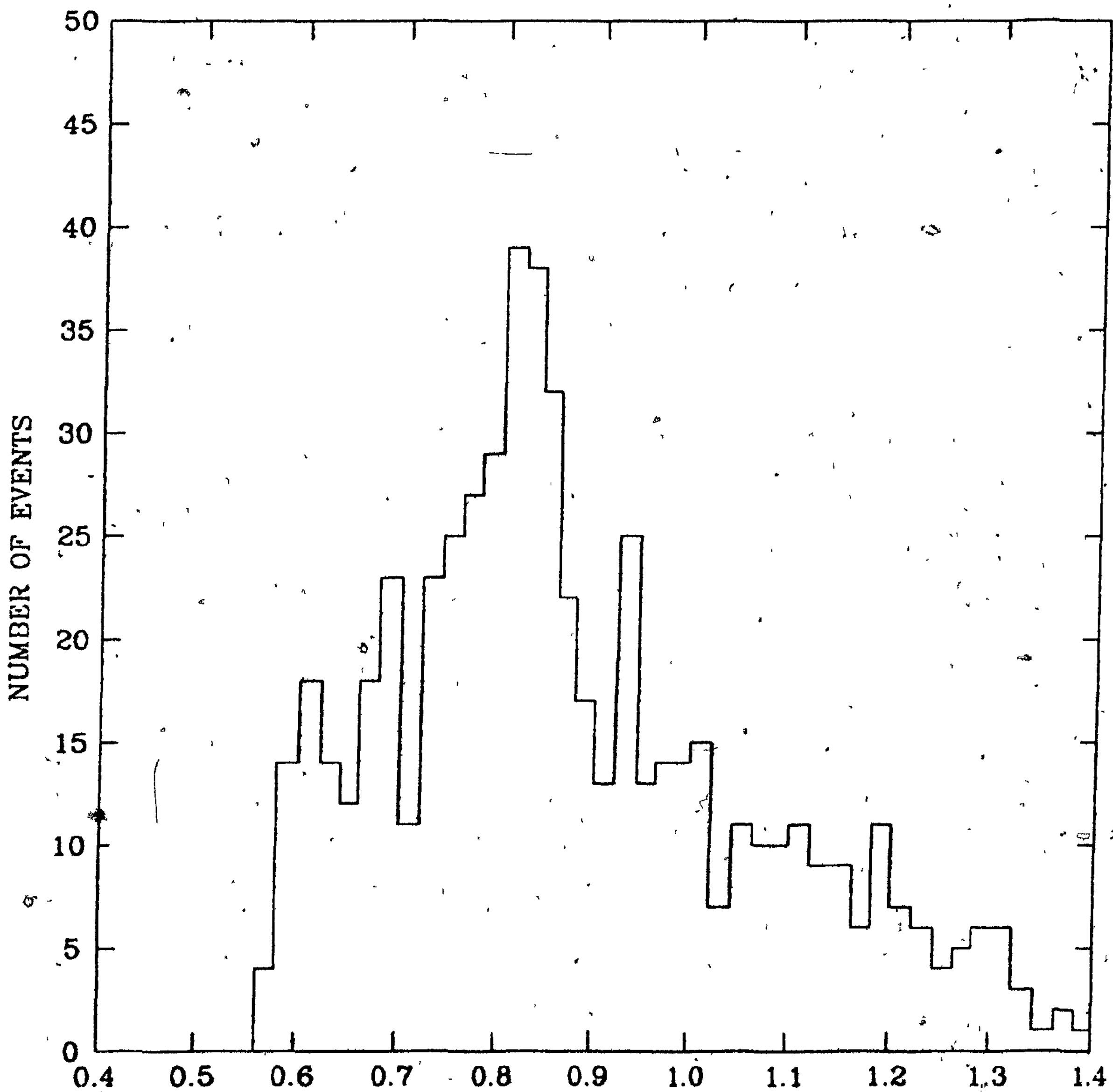

FIG.7-16. $M_{\eta\gamma}$ 3C fit with E_{γ} cuts. $M_{\pi^{+}\pi^{-}\pi^{0}} < .60$ Gev.

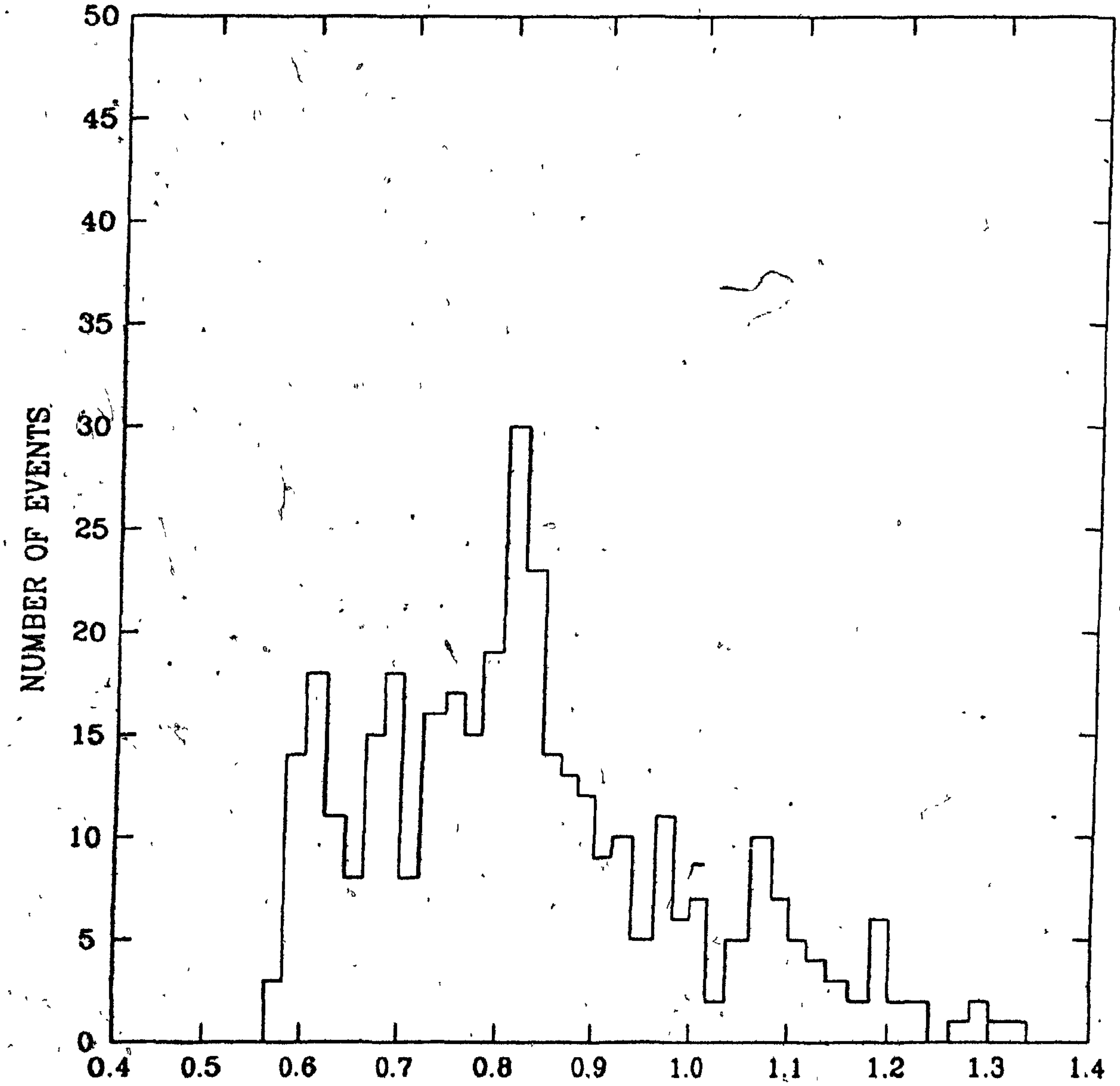

FIG.7-17. $M_{\eta\gamma}$ with E_{γ} cuts. $M_{\pi^+\pi^-\pi^o}$ < .58 Gev.

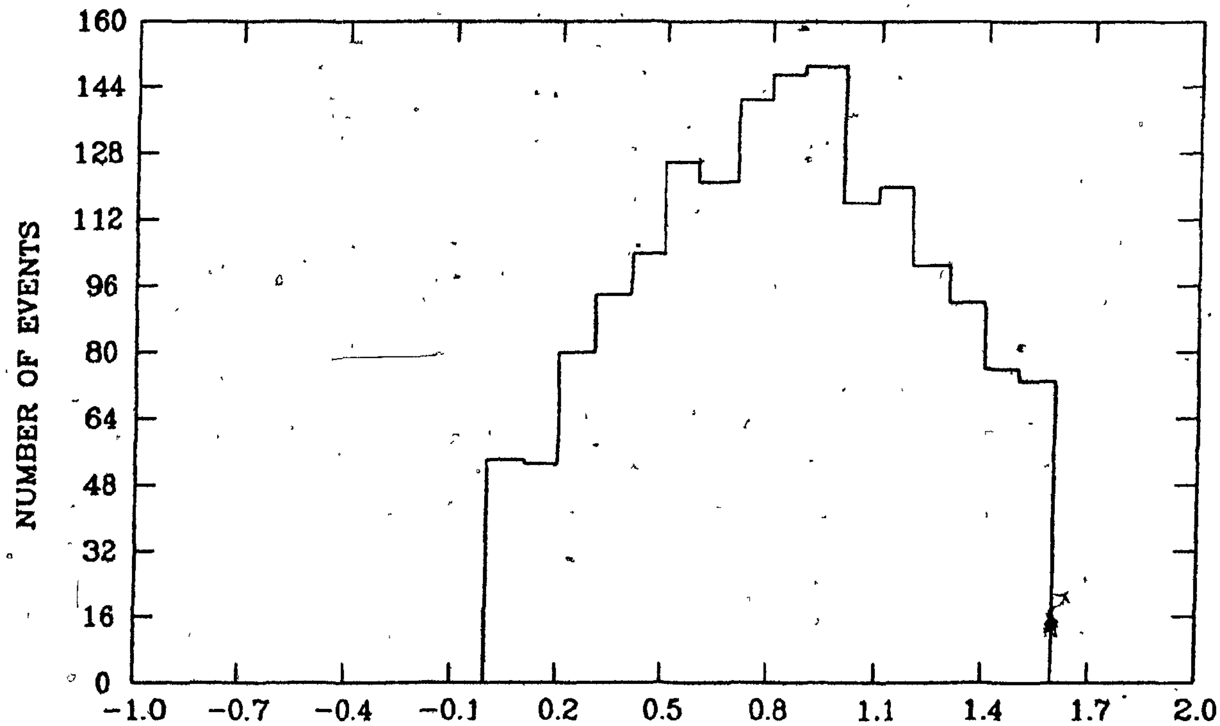

FIG.7−18a. M_{rec}. Monte-Carlo with E_{γ} cuts. $M_{\pi^+\pi^-\pi^o}$ < .58 Gev.

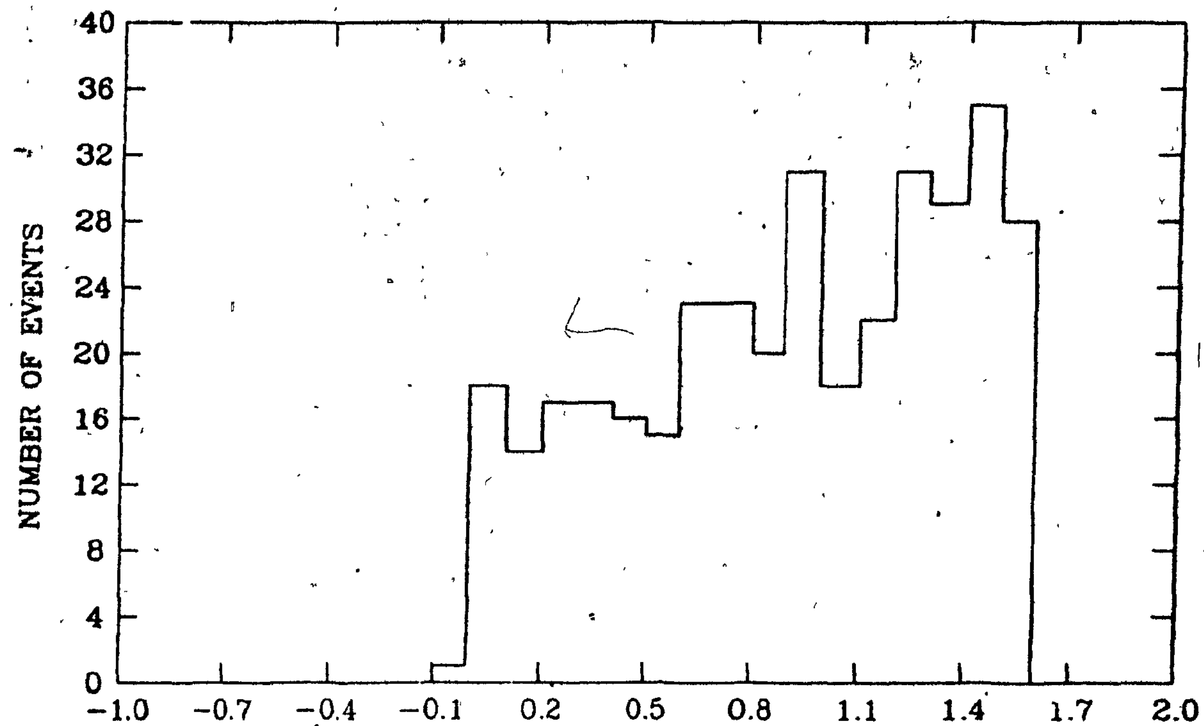

FIG.7−18b. M_{rec}, with E'_{γ} cuts. $M_{\pi^+\pi^-\pi^o}$ < .58 Gev.

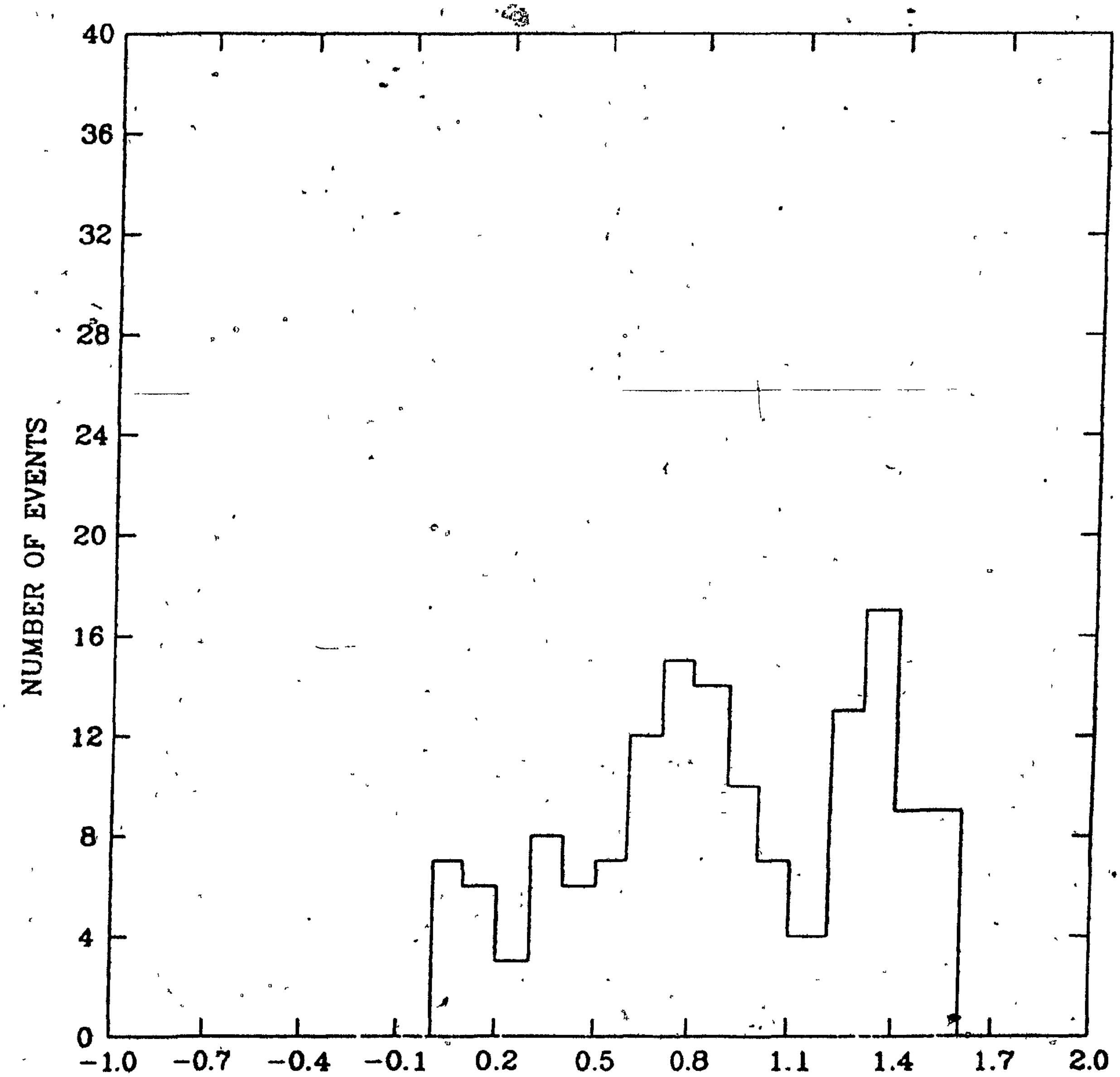

FIG. 7−19. M_{rec}, with E_{γ} cuts, $M_{\pi^+\pi^-\pi^0} < .58$, $.72 < M_{\eta\gamma} < 1.2$ Gev.

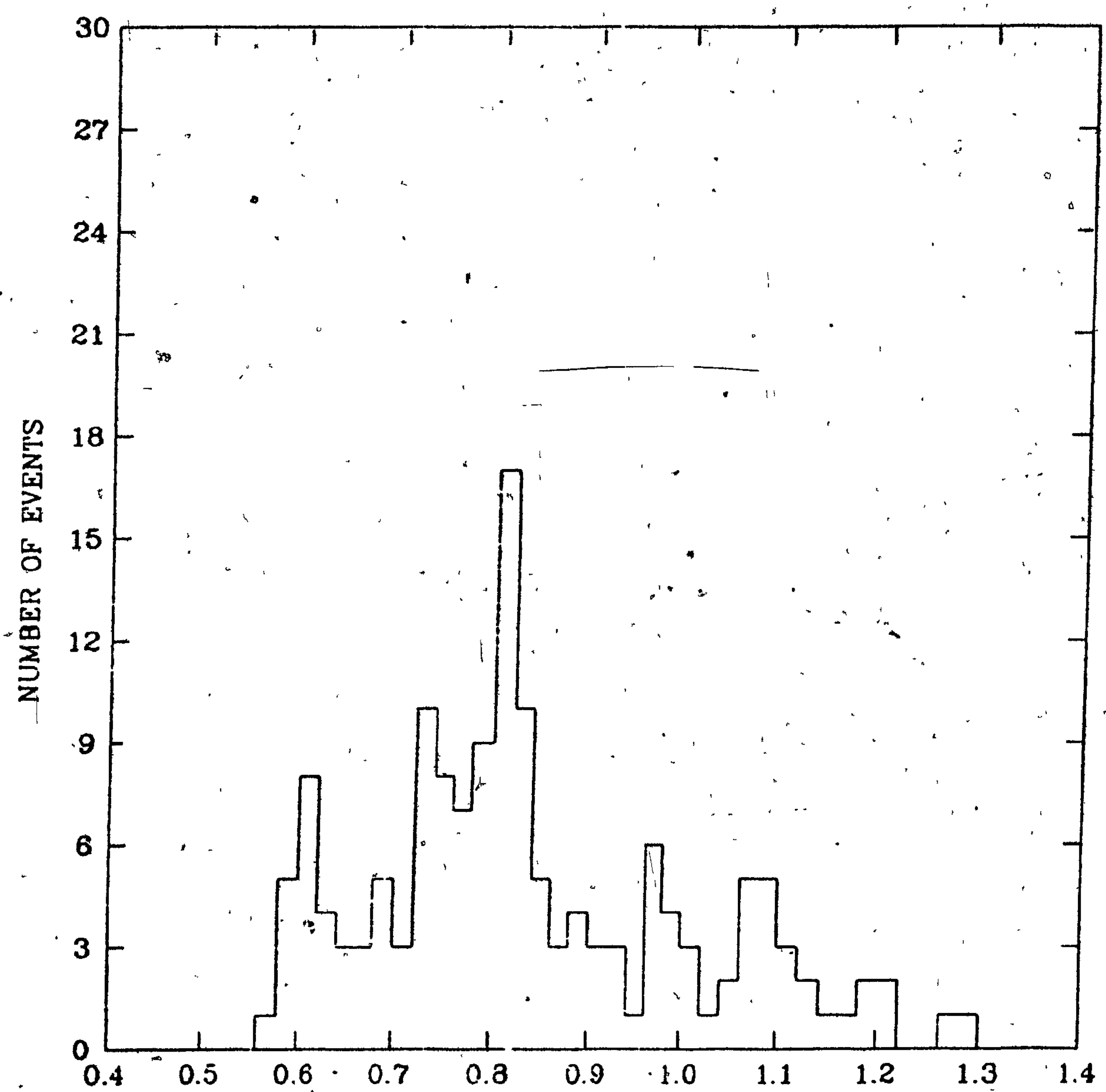

FIG.7–20. $M_{\eta\gamma}$ with E_γ cuts, $M_{\pi^+\pi^-\pi^0} < 58$, $.5 < M_{rec} < 1.2$ Gev.